DEVELOPMENT AND EVALUATION OF THE (GEF) MODEL AT MEDIUM AND SEASONAL RANGES

Dragan Latinovic

Doctorate Thesis of the Graduate Course in Meteorology, guided by Dr. Chou Sin Chan, approved in February 28, 2018.

URL of the original document:
<http://urlib.net/8JMKD3MGP3W34R/3QNATU8>

INPE

São José dos Campos

2018

DEVELOPMENT AND EVALUATION OF THE (GEF) MODEL AT MEDIUM AND SEASONAL RANGES

Dragan Latinovic

Doctorate Thesis of the Graduate Course in Meteorology, guided by Dr. Chou Sin Chan, approved in February 28, 2018.

URL of the original document:
<http://urlib.net/8JMKD3MGP3W34R/3QNATU8>

INPE

São José dos Campos

2018

Aluno (a): *Dragan Latinovic*

Título: **"DEVELOPMENT AND EVALUATION OF THE GEF MODEL AT MEDIUM AND SEASONAL RANGES".**
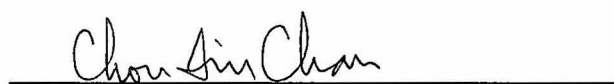
Aprovado (a) pela Banca Examinadora em cumprimento ao requisito exigido para obtenção do Título de *Doutor(a)* em

Meteorologia

Dr. **Nelson Jesuz Ferreira**

Presidente / INPE / Cachoeira Paulista - SP

( ) Participação por Video - Conferência

Dra. **Chou Sin Chan**
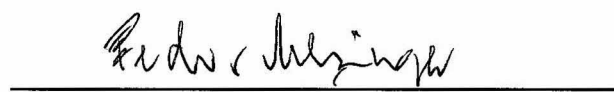
Orientador(a) / INPE / Cachoeira Paulista - SP

( ) Participação por Video - Conferência

Dr. **Silvio Nilo Figueroa Rivero**

Membro da Banca / INPE / Cachoeira Paulista - SP

( ) Participação por Video - Conferência

Dr. **Fedor Mesinger**

Convidado(a) / CAHY/SANU / Serbia - BEG

( ) Participação por Video - Conferência

Dr. **Miodrag Rancic**

Convidado(a) / NOAA / Estados Unidos - USA

(X) Participação por Video - Conferência

Este trabalho foi aprovado por:

(X) *maioria simples*

( ) *unanimidade*

São José dos Campos, 28 de fevereiro de 2018.

ACKNOWLEDGEMENTS

This thesis is dedicated to my parents, for their love, endless support and encouragement throughout my life and to my wife for the same, for being ever-present and for sharing all the good times and bad, especially in this important time of my life.

ABSTRACT

The objective of this research is to implement the Global Eta Framework (GEF) model and evaluate its performance in medium and seasonal range integrations. GEF is a global atmospheric model on cubed-sphere grid, constructed as a combination of the technique of quasi-uniform gridding of the sphere and the numerical structure of the regional Eta model. Six regional models, interconnected through the cubed-sphere framework are integrated simultaneously, one on each side of the cube, to provide a global coverage and to create unique "globalized" version of the regional Eta model. Two model setups of the model are developed and configured, one at 25-km horizontal resolution for seasonal range runs and another at 8-km horizontal resolution for medium-range runs. Total of 10 seasonal integrations of approximately 4 months are performed creating 5 member ensembles for the period September-November (SON) of 2011 and 2013 with the objective to evaluate the model skill to simulate the onset of the rainy season in Western-Central Brazil (WCB). Comparative assessment of daily means of global model output fields against appropriate reanalysis and observations for the austral spring indicates high level of agreement, both in spatial distribution and intensity for most of the variables. The lowest skill is shown for precipitation which is overestimated over some tropical oceanic regions and underestimated over tropical continental regions, including South America. Other fields, evaluated at different levels include 200-hPa wind from upper-troposphere, 500-hPa geopotential height from mid-troposphere, 850-hPa temperature and wind representing lower-troposphere and mean sea level pressure (MSLP) at the surface. The onset of the rainy season is determined by using methods based on precipitation and outgoing long-wave radiation (OLR). Comparison of 5-day averaged values (pentads) of precipitation and OLR of the ensemble members and the ensemble mean against observed data shows the ability of GEF to reproduce the typical pattern of transition from dry to wet season in WCB almost in the same pentad determined by both methods. However, most of ensemble members tend to underestimate precipitation and overestimate OLR. The other set of integrations

is performed at 8-km horizontal resolution, for the length of 10 days. The total of 22 integrations is performed with the lead times of 24 h, 48 h and 72 h to analyze 8 selected cases of extreme rainfall over the city of Manaus, Amazonas. The model demonstrates the ability to simulate well the large-scale patterns for the period of up to 7 days. The Equitable Threat Score (ETS) for the time ranges of 36 h and 60 h shows that the model simulates well the areas with precipitation, while for the higher thresholds, the results are on the lower limit of referential values. The BIAS score (BIAS) shows almost "perfect" score for the lowest "rain-no rain" threshold, and decreases rapidly for the other thresholds. The areas with precipitation over South America are well simulated by the model, with comparable intensity in extratropical regions and mostly underestimated values in the tropical regions. The model simulated rain for Manaus in almost every simulation, with underestimated values in most of the cases, in addition to showing the low skill in the simulation of the positions of the precipitation maxima in Central Amazon. The computational efficiency of GEF and the results presented in this study show that continuous efforts in the development of the GEF model can give significant contribution to the improvement of medium-range and seasonal forecasts at CPTEC. Improvements mostly related to the parameterization of convection and radiation, and the ongoing development of nonhydrostatic version should position GEF as a good candidate for future unified model of the centre, capable of running across a range of scales.

Key words: Global Eta Framework. eta coordinate. cubed-sphere. monsoon onset. diurnal cycle. global model

DESENVOLVIMENTO E AVALIAÇÃO DO MODELO "GLOBAL ETA FRAMEWORK" (GEF) NO PRAZO MÉDIO E SAZONAL

RESUMO

O objetivo desta pesquisa é implementar o modelo "Global Eta Framework" (GEF) e avaliar seu desempenho em simulações sazonais e de prazo médio. O GEF é um modelo atmosférico global em grade cúbica, desenvolvido a partir de uma combinação da técnica de grades quasi-uniformes e a estrutura numérica do modelo Eta regional. Seis modelos regionais, interconectados através da estrutura da grade cúbica, são integrados simultaneamente, um em cada face do cubo, para fornecer uma cobertura global e criar uma versão única "globalizada" do modelo Eta regional. Duas versões do modelo são desenvolvidas e configuradas, uma com resolução horizontal de 25 km para simulações sazonais e outra com a resolução horizontal de 8 km para testes de médio prazo. Um total de 10 integrações sazonais de aproximadamente 4 meses são realizadas para o período setembro-novembro (SON) de 2011 e 2013 com o objetivo de avaliar a capacidade do modelo para simular o início da estação chuvosa na região Centro-Oeste do Brasil (COB). Integração para cada ano consiste de um conjunto de 5 membros. A comparação entre as medias diárias dos campos globais simulados e a reanálise ou as observações para o período SON indica boa concordância, tanto na distribuição espacial quanto na intensidade para a maioria das variáveis. A simulação de precipitação mostra desempenho mais baixo devido à superestimativa em algumas regiões oceânicas tropicais e à subestimativa em regiões continentais tropicais, incluindo a América do Sul. Outras variáveis avaliadas em diferentes níveis, incluem o vento de 200 hPa, altura geopotencial de 500 hPa, temperatura e vento de 850 hPa e pressão do nível médio do mar. O início da estação chuvosa é determinado utilizando os métodos baseados em precipitação e radiação da onda longa (ROL). A comparação de valores médios de 5 dias ("pentadas") de precipitação e ROL dos membros de conjunto e a média do conjunto com os dados observados mostra a capacidade do modelo GEF em reproduzir o padrão de transição da

estação seca para estação chuvosa na região COB. No entanto, a maioria dos membros do conjunto tende a subestimar a precipitação e a superestimar a ROL. Um outro conjunto de integrações é produzido na resolução horizontal de 8 km, para o prazo de 10 dias. Um total de 22 integrações são realizadas com o "lead time" de 24 hs, 48 hs e 72 hs para analisar 8 casos selecionados de precipitação extrema sobre a cidade de Manaus, AM. O modelo demonstrou a capacidade de simular bem os padrões de grande escala no período de até 7 dias. O "Equitable Threat Score" (ETS) para os intervalos de tempo de 36 hs e 60 hs mostra que o modelo simula bem as áreas com precipitação, enquanto que para os limiares mais altos, os resultados estão no limite inferior dos valores referenciais. O índice BIAS (BIAS) mostra o valor próximo a 1 para o menor limiar "chuva-sem chuva" e diminui rapidamente para os outros limiares. As áreas com precipitação sobre a América do Sul são bem simuladas pelo modelo, com intensidade comparável em regiões extratropicais e valores principalmente subestimados nas regiões tropicais. O modelo simulou chuva para Manaus em quase todas as integrações, com valores subestimados na maioria dos casos, mostrando dificuldades na simulação das posições dos máximos de precipitação na Amazônia Central. A eficiência computacional do GEF e os resultados apresentados neste estudo confirmam que esforços contínuos no desenvolvimento do modelo podem dar uma contribuição significativa na melhoria da previsão sazonal e de médio prazo no CPTEC. As melhorias relacionadas principalmente com a parametrização de convecção e radiação, juntamente com o desenvolvimento contínuo da versão não hidrostática podem posicionar o GEF como um bom candidato para o futuro modelo unificado do centro, capaz de atuar em varias escalas.

Palavras-chave: Global Eta Framework. coordenada eta. esfera cúbica. início da estação chuvosa. ciclo diurno. modelo global

LIST OF FIGURES

xiv

LIST OF TABLES

LIST OF ACRONYMS

ABLE2B   Amazon Boundary-Layer Experiment

ABRACOS   Anglo-Brazilian Amazonian Climate Observation Study

AGCM   Atmospheric Global Circulation Model

AM   Amazonas, state in Brazil

BOS   Basin Occurring Systems

CAPE   Convective Available Potential Energy

CCSR   Center for Climate System Research

CGCM   Coupled Global Circulation Model

CHUVA   Cloud processes of tHe main precipitation systems in Brazil: A contribUtion to cloud resolVing modeling and to the GPM (GlobAl Precipitation Measurement)

CIN   Convective Inhibition Energy

CMIP3   Coupled Model Intercomparison Project Phase 3

CMIP5   Coupled Model Intercomparison Project Phase 5

CMORPH   CPC MORPHing technique

COLA   Center for Ocean–Land–Atmosphere Studies

COS   Coastal Occurring Systems

CPTEC   Centro de Previsão de Tempo e Estudos Climáticos (Center for Weather Forecasting and Climate Studies)

DJF   December-January-February

DWD   Deutscher Wetterdienst

ECHAM   European Centre Hamburg Model

ECMWF   European Centre for Medium-Range Weather Forecasts

ENSO   El Niño Southern Oscillation

EOF   Empirical orthogonal function

ERA INTERIM   A global atmospheric reanalysis from 1979, continuously updated in real time

FMA   February-March-April

GEF   Global Eta Framework

GEM   Global Environmental Multiscale model

GFDL   Geophysical Fluid Dynamics Laboratory

GOAMAZON   Green Ocean Amazon

GPCP   Global Precipitation Climatology Project

HOMME   High-Order Method Modeling Environment

ICON   Icosahedral Non-hydrostatic

IFS   Integrated Forecast System model

INPE   Instituto Nacional de Pesquisas Espaciais (National Institute
for Space Research)

ITCZ   Inter-Tropical Convergence Zone

JJA   June-July-August

KF   Kain-Fritsch

LFC   Level of free convection

LCL   Lifted condensation level

LOS   Locally Occurring Systems

MCC   Mesoscale convective complex

MPAS   Model for Prediction Across Scales

MSLP   Mean sea level pressure

NCEP   National Centers for Environmental Prediction

NICAM   Non-hydrostatic ICosahedral Atmospheric Model

NIM   Non-hydrostatic Icosahedral Model

NOAH: N-National Centers for Environmental Prediction (NCEP), O:
Oregon State University (Dept. of Atmospheric Sciences), A: Air Force (both
AFWA and AFRL-formerly AFGL, PL), H: Hydrology Lab-NWS (formerly Office
of Hydrology-OH)

N-S   north-south

NW-SE   northwest-southeast

OLR   Outgoing Longwave Radiation

RRTMG   Rapid Radiative Transfer Model for GCM

SACZ   South Atlantic Convergence Zone

SALLJ   South American Low Level Jet

SAMS   South American Monsoon System

SE-NW   southeast-northwest

SON   September-October-November

TRMM/LBA   Tropical Rainfall Measuring Mission/LBA Large-Scale Biosphere-Atmosphere

WCB   Western-Central Brazil

WCRP-CMIP3   World Climate Research Project – Coupled Model Intercomparison Project

WETAMC/LBA   Wet season Atmospheric Mesoscale Campaign/Large-Scale Biosphere-Atmosphere

TABLE OF CONTENTS

1 INTRODUCTION

As global atmospheric models became more complex and started to include more physical processes, the spectral transform method, that was especially successful for large scale dynamical motions and had advantages at coarse resolution, dominated the global atmospheric modelling for some time. The emphasis in the numerical methods development today is placed on developing methods with more desirable physical properties, especially conservation and shape preservation, while maintaining the accuracy and efficiency gained in the past. Most of the development is based on quasi-uniform grids. Another aspect driving current development is the need to develop schemes which are capable of running efficiently on computers with thousands of processors and distributed memory.

Several high-resolution global atmospheric models are in use today in many institutions around the world, with applications ranging from experimental science to operational forecasting. With the advances achieved in computer technology, there is an increasing tendency to unify climate models with global weather prediction models. New technologies such as variable-resolution mean that parts of the globe can now be simulated at extremely high resolutions. The following list shows the nonhydrostatic global atmospheric models and actively developing nonhydrostatic dynamical cores in many major international modelling centres (Ullrich, 2015):

1) GFDL FV3 (FV-Cubed) model (Geophysical Fluid Dynamical Laboratory, Princeton, NJ) (PUTMAN; LIN, 2009; PUTMAN; SUAREZ, 2009),

2) High-Order Method Modeling Environment (HOMME) models (Sandia National Laboratory, Albuquerque, NM) (FOURNIER et al., 2004; TAYLOR et al., 2008),

3) Icosahedral Non-hydrostatic (ICON) GCM (Max Planck Institute for Meteorology, Hamburg, Germany and DWD) (WAN, 2009; GASSMANN, 2010),

4) ECMWF Integrated Forecast System (IFS) model (WEDI et al., 2010),

5) Global Environmental Multiscale (GEM) model (YEH et al., 2002),

6) Model for Prediction Across Scales (MPAS) (NCAR, LANL/DOE) (SKAMAROCK et al., 2010),

7) Non-hydrostatic ICosahedral Atmospheric Model (NICAM), developed in cooperation with the Center for Climate System Research (CCSR, Japan) (TOMITA; SATOH, 2004),

8) Non-hydrostatic Icosahedral Model (NIM) (Earth System Research Laboratory, NOAA) (GOVETT et al., 2010),

9) UK Met Office Unified Model (DAVIES et al., 2005; STANIFORTH; WOOD, 2008).

Even if multiple simultaneous modelling efforts in the centres around the world might seem as a waste of time and resources, there are numerous benefits to the diversity of that approach. There is no "correct" model design, because all models represent an approximation to reality. Since the Coupled Model Intercomparison Project phase 3 (CMIP3), it has been clear that the mean model behaviour actually outperforms any individual model in representing the Earth system.

In agreement with the simultaneous modelling efforts around the world and as a contribution to the modelling approach diversity, the Global Eta Framework model (GEF), developed by Zhang and Rančić (2007) seems to be a good candidate to be implemented and improved in the Center for Weather Forecasting and Climate Studies (CPTEC). It is based on quasi-uniform cubed-sphere grid, it is computationally efficient and, in addition, it uses the numerical infrastructure of the regional Eta model, an operational model in CPTEC. The concept of a unified or seamless framework for weather and climate prediction, that attracted a lot of attention in the last few years (HURRELL et al., 2009; BRUNET et al., 2010; SHAPIRO et al., 2010; NOBRE et al., 2010; HAZELEGER et al., 2010; SENIOR et al., 2011) was the motivation to explore the potential of GEF to run at high resolution in weather and climate simulations.

As an early stage of going in that direction, GEF is configured and evaluated at 25-km horizontal resolution for the seasonal integrations and 8-km horizontal resolution for the medium-range integrations with the results presented in this thesis.

1.1 Objectives

The main objective of this research is to evaluate the skill of GEF in seasonal and in medium-range simulations.

1.2 Specific objectives

1) Evaluate the model skill in simulating the onset of the rainy season in seasonal runs

2) Evaluate the model skill in simulating the diurnal cycle of precipitation

3) Evaluate the model skill at high-resolution version of the model in the medium-range simulations of extreme precipitation events

To this end, the onset of the rainy season in Western-Central Brazil for the years 2011 and 2013, and diurnal cycle of precipitation will be analyzed through the ensemble of seasonal simulations, and 8 selected cases of extreme precipitation events occurred in the city of Manaus, Amazonas (AM), in last 5 years will be simulated at high-resolution.

In Chapter 2, the introduction about convective processes and their parameterizations is presented, together with the introduction about global atmospheric models and GEF. Chapter 3 starts with the introduction about South American monsoon characteristics and monsoon onset and with some initial results obtained using configuration of the model at 25-km horizontal resolution for seasonal integrations. It continues with the evaluation of

simulation of the large-scale features and of the onset of the rainy season and ends with the analysis of the diurnal cycle of precipitation and Chapter discussion and conclusions. In Chapter 4, simulations of the large-scale features and 8 events of extreme precipitation in Manaus are evaluated, and some statistical analysis performed with the configuration of the model at 8-km horizontal resolution for medium-range integrations. The chapter ends with chapter discussions and conclusions. Chapter 5 summarizes the obtained results and presents the general conclusions of the thesis.

2 LITERATURE REVIEW

2.1 Convective processes

The Amazon is home to the world's largest continuous rainforest, although it has lost the largest amount of forest among all tropical countries. It holds about 60 percent of the world's remaining rainforests and stores billions of metric tons of carbon. Tropical deforestation represents the most important land cover change and the carbon cycle change. The Amazon has been labeled as one of the global heat engines because it drives large-scale patterns of atmospheric circulation and precipitation (GEIST, 2006). Convection in the Amazon region is an important mechanism for heating the tropical atmosphere. The release of heat during the rainy season is typically 2.5 K day^{-1} (FIGUEROA; NOBRE, 1990), the equivalent of a precipitation of 10 mm day^{-1}. Land use changes in the Amazon have complex effects in distant regions of the world, although most of their impacts are local (GEIST, 2005).

Meteorological conditions in the Amazon are affected by a wide spectrum of phenomena that range from the cumulus convection scale to the global scale. According to Molion (1987, 1993), the mechanisms that cause the precipitation in the Amazon can be grouped into 3 types:

a) daytime convection resulting from surface warming and favorable large-scale conditions,
b) squall lines originating along the north-northeast coast of the Atlantic coast,
c) meso- and large-scale convective clusters, associated with the passage of frontal systems in the south-southeast region of Brazil and interaction with the Amazon convection.

The spatial and temporal distribution of rainfall in the Amazon was studied in detail by Figueroa and Nobre (1990), who used 226 rainfall stations, and by Marengo (1995), who used long-wave radiation data. The maximum rainfall in central Amazon (close to latitude 5°S) may be associated with the

passage of frontal systems in the southern region, which interact and organize the local convection. The period of rainfall or strong convective activity in the Amazon region occurs between November and March, and the dry season (without large convective activity) is between May and September. The months of April and October are months of transition from one regime to another. Rainfall distribution in the December-January-February trimester (DJF) shows a region of heavy rainfall (over 900 mm year^{-1}) located in the western and central part of Amazon. On the other hand, in the June-July-August trimester (JJA), the centre of maximum precipitation moves to the north and positions over Central America. Therefore, the atmospheric convection dominates the weather and climate conditions of the Amazon region. The convective environment in the Amazon is quite complex and heterogeneous, and is not categorized as representative of any classical convective regime (e.g. tropical continental) (WILLIAMS et al., 2002). The temporal evolution, frequency and morphology of deep convection can vary greatly, depending on the regime, e.g. organized convective systems (squall lines and mesoscale convective systems). The seasonal variability of convection can be very large depending on whether the season is rainy, dry or transitional. The intraseasonal variability may also change the thermodynamic characteristics of the convective environment and changes in precipitation occurrence and frequency, as well as cloud morphology (PETERSEN; RUTLEDGE, 2001; PETERSEN et al., 2006).

Shallow (non-precipitating) convection and deep (precipitating) convection are among the major components of the local energy balance. In addition, precipitating convection is essential for the hydrological cycle, as it influences the large-scale tropical dynamics and it is critical in the energy balance of the planet's general circulation. One of the major challenges of tropical meteorology for decades is to relate the local nature of convection and its interaction with the large-scale atmosphere circulation. The climate of the Amazon region is a combination of several factors, and the most important is the availability of solar energy in the energy balance. Measurements taken in Manaus, AM, indicate that solar radiation arriving at the surface peaks in the

months of September and October, and the minima occur from December to February. This distribution is controlled by the cloudiness of southeast-northwest (SE-NW) migration of Amazon convection (HOREL et al., 1989). Part of the energy that reaches the Earth's surface returns to the atmosphere in the form of sensible (heating) and latent (evapotranspiration) heat. In this way, the balance of radiation, being partitioned in terms of sensible and/or latent heat, depends on the environmental conditions and water in the soil.

In the Amazon basin, there are regional differences in the convective regimes (e.g. coastal areas versus central Amazon), which are visible in the seasonal distribution of rainfall and in the character of convective events (GARSTANG et al., 1990; PETERS et al., 2002, 2006). The squall lines represent a notable convective aspect of the region and they are responsible for a considerable amount of annual precipitation. Greco et al. (1990) classify the Amazon convection into three categories: Coastal Occurring Systems (COS), Basin Occurring Systems (BOS) and Locally Occurring Systems (LOS). The main differences between these systems are: geographic location, propagation and life cycle. The squall lines classified as COS represent the systems with the largest geographical extension and duration. These lines are typically generated along the coastal region of north-eastern Amazon as a result of the convergence of the sea breeze upon reaching the continent due to the difference in roughness (GARSTANG et al., 1994). With north-south (N-S) and northwest-southeast (NW-SE) orientation, the lines propagate to the west, extending for more than 1000 km in horizontal length and lasting for more than 48 hours (GARSTANG et al., 1994). They occur mostly between April and August (transition months from rainy to dry season). These lines produce a significant amount of the total precipitation in the central part of the Amazon Basin (GARSTANG et al., 1994). The systems of the categories BOS and LOS tend to be numerous, of shorter duration and horizontal length, and are typically distributed throughout an immense region in the Amazon Basin and occur under varied synoptic conditions (GRECO et al., 1990). Systems in the BOS category, compared to LOSs, also tend to form lines while the LOSs organize more freely,

7

often within a diurnal cycle.

Further inland, southwest of the Amazon, different "eastern" and "western" convective regimes exhibit changes in atmospheric stability, convection organization, convective and stratiform precipitation segregation and lightning frequency, among other characteristics (HALVERSON et al., 2002, LAURENT et al., 2002, PETERSEN et al., 2002, CIFELLI et al., 2004). The evolution of the thermodynamic environment and its relation with convection has been investigated in the Amazon. Two important variables that define the local stability of the thermodynamic profile are CAPE and CIN (Convective Available Potential Energy-CAPE and Convective Inhibition Energy-CIN). They are important for triggering and modulating convection. Fu et al. (1999) concluded that CIN is important for the beginning of the convection in different regions of the Amazon Basin in the seasonal scale. They found that the increasing instability of the atmosphere, due to surface warming and to the increasing moisture advection from July to August in the southern Amazon basin, does not necessarily lead to more convective activity. The role of CIN in modulating the occurrence of convection in the tropics was also noted in the observational studies of Williams and Rennó (1993) and in the theoretical studies of Raymond (1995) and Mapes (2000). Examining the diurnal cycle in the local convective phase during the WETAMC/LBA experiment, Machado et al. (2002) found that CAPE increased very rapidly between morning and early afternoon. The lack of cloud cover implies higher solar radiative fluxes reaching the surface, which rapidly increases CAPE. At the same time, CIN values decrease because of lower level of free convection (LFC) as the surface warmed. With the development of deep convection and afternoon precipitation, the boundary layer cools through convective descending currents and evaporation of precipitation. The moisture flux of the boundary layer then decreases, the atmospheric profile follows approximately a wet adiabatic and, consequently, becomes neutral for convection. The convective instability is therefore removed, completing the cycle. From this discussion, it is evident that to understand the evolution of CIN/CAPE and the start time and convection

cycle, the role of surface heating, moisture flows, convective descending currents and large-scale subsidence must be carefully examined, particularly with respect to boundary layer forcing and large scale. More details about convective processes in the Amazon can be found in Adams et al. (2009).

If deep convection is very dependent on large-scale processes, the frequency and intensity of shallow convection are very sensitive to local factors such as vegetation cover, topography, etc. The shallow convection, in addition to the influence on the thermodynamic profile of the layer where it acts, is fundamental in the energy balance of the surface and the convective boundary layer. The presence of shallow cloud clusters implies several feedback mechanisms. The full effect of shallow convection is completed by shortwave radiation. The attenuation of solar radiation due to shallow convection, which can cover more than 60% of continental regions (WETZEL et al., 1996), is of great importance for obtaining more realistic simulations. The presence of shallow convective clouds definitely influences the surface energy balance. The absence of this interaction process between shallow convection and radiation causes the overestimate of surface energy balance in the models.

2.2 Parameterization of convective processes

Convective cloud systems are responsible for much of the vertical transport of mass, heat and moisture in the atmosphere, especially in the tropical region. The strong ascending currents observed in the convective clouds and the compensating subsidence correspond to circulations whose scale, of the order of 1 km or less, prevents from explicitly solving these clouds in low-resolution models. Thus, all physical processes that occur at scales smaller than those resolved by the models need to be parameterized. In the case of convection, the problem is to connect convective condensation and heat, moisture and momentum transport through cumulus clouds, which cannot be explicitly solved by the resolved model variables of low-resolution models (COTTON; ANTHES, 1989). This is known as convection parameterization or

9

cumulus parameterization. According to Cotton and Anthes (1989), the problem of convection parameterization is to connect the convection and the transport associated with it, which cannot be solved, with the larger scale variables provided by the model.

However, the convective parameterizations typically used in low-resolution models have experienced difficulties in simulating the effects of convective processes in all tropical regions and particularly in representing the diurnal cycle (LIN et al., 2000; YANG; SLINGO, 2001). The Amazon Basin has been shown to be a particularly challenging region for testing convective parameterization because of the presence of various convective regimes and complex interactions between the surface and the atmosphere. In order to better understand the complex links between convection, surface energy fluxes and large-scale forcing, several intensive observational studies in the Amazon, including field campaigns and remote sensing (e.g., ABLE2B, ABRACOS, WETAMC/LBA, TRMM/LBA, LBA dry-to-wet, CHUVA, GOAMAZON). Data from these campaigns were used to reduce the deficiencies in modelling convection.

The main deficiencies in the convection parameterizations are the simulations of the convection diurnal cycle. These difficulties are particularly evident when it is necessary to present with fidelity the growth of the convective boundary layer and the gradual transition from shallow to deep convection.

The convective environment in the Amazon is complex and heterogeneous, and is not categorized as representative of any classical convective regime (e.g., tropical continental) (WILLIAMS et al., 2002). The temporal evolution, frequency, and morphology of deep convection can vary significantly, depending on the convective regime. For example, some regimes often have organized convective systems, such as: linear instability lines and mesoscale convective complexes, while others have a strong diurnal cycle of non-organized convective cells. The nature of the convective regime can vary depending on the season, if it is rainy, dry or transitional

Examining the diurnal cycle in the TRMM/LBA WETAMC experimental region, Machado et al. (2002) demonstrated that CAPE is very sensitive to

moisture and temperature of the boundary layer, whereas the upper troposphere has less influence. This implies that the CAPE is substantially controlled by the evolution of the boundary layer, i.e. changes in heat and moisture fluxes (DONNER; PHILLIPS, 2003; ZHANG, 2003a, b). This has important implications for cumulus parameterizations based on the near-equilibrium principle or CAPE-based closure schemes (DONNER; PHILLIPS, 2003). Therefore, an appropriate simulation of the boundary layer is crucial for modelling convection in the Amazon. The nocturnal stable boundary layer is not as stable in the model simulations as it is in nature. In nature, strong stabilization often results from the mesoscale sub-saturated downstream currents associated with organized convection of the previous afternoon and evening (BETTS; JAKOB, 2002a, b; RICKENBACH, 2004). Similarly, nocturnal convection associated with propagating squall lines can also suppress precipitation the next day (RICKENBACH, 2004). It seems that none of these stabilizing processes is well represented in the models.

The way convective parameterization relates the thermodynamic stability and the convection activation and intensity determines the nature of simulated precipitation in deep convective regimes. In fact, thermodynamic instability is not the only factor that determines the onset of deep convection. Wind shear, small and large-scale dynamics, and instability lines may play key roles in the activation or suppression of convective elements. These factors, however, are typically neglected in parameterization of convective processes.

2.3 Global atmospheric models

The first global atmospheric models were developed in the early 1960s. Since that time, they have evolved and nowadays they find their application in weather and seasonal forecasts and in climate change simulations and projections. Development of the numerical methods for global models has been an active area of research since the appearance of the first global models, and continues with renewed interest today. The research is divided in two areas, the

first deals with numerical methods for calculating transport and for calculating hydrostatic, large scale fluid motion in the atmosphere, from the largest scales down to those below synoptic scales. The second area of research is in the adapting these numerical methods to the spherical geometry of the Earth, which usually faces the problem called the singularity of the poles. However, these two areas are not completely independent. Many of the earliest models used a finite-difference horizontal discretization of the equations of motion, in which the evolution of the state of the atmosphere is followed on a set of horizontal grid points. Spherical curvilinear coordinates (latitude and longitude) present the most obvious coordinate system for the surface of the sphere. A problem with finite-difference methods based on spherical coordinates is that the meridians converge at both poles, making the longitudinal grid interval approach zero. The existence of the singularities on the poles is defined as the "pole problem". It necessitates the use of very short time steps unless a filter of some kind is used to remove short zonal wavelengths at high latitudes. A technique of Fourier filtering (ARAKAWA; LAMB, 1977; TAKACS; BALGOVIND, 1983) is typically used to release the restriction on the time step.

In the mid to late 1970s, further development of grid-point schemes for spherical geometry slowed down in favour of the spectral transform method (ELIASEN et al., 1970; ORSZAG, 1970). Although grid-point models continued to be used, the level of research and development into explicit grid-point approximations dropped. The basic idea of spectral transform method is to represent the horizontal structure of the global atmosphere using truncated spherical harmonic expansions (SILBERMAN, 1954; PLATZMAN, 1960). The amplitudes of these harmonics represent the fundamental model variables and they can transform back to physical space when needed. By including a sufficient number of spherical harmonics, in theory, the resolution can be made as high as desired. Using spectral methods, spherical geometry is handled in a very natural way and the pole problem is eliminated. It was especially good for large scale, relative smooth dynamical motions and had advantages at coarse resolution that was common then. In 2005, the spectral transform method was

the basis of 11 out of 14 recent operational global NWP systems, the remaining 3 were grid point based (WGNE 2005, Appendix E), indicating the popularity of the spectral transform method. Even if the spectral models have dominated atmospheric modelling, for both climate research and numerical weather prediction, for the past several decades, they also have significant deficiencies. A problem with this approach is that the quadratically nonlinear processes of a model, notably advection, are represented by sums in which the numbers of terms increase quadratically with the number of spherical harmonics kept, making high-resolution models impractical. A further difficulty is that it would be virtually impossible to formulate the physical parameterizations of a model in wave-number space.

With the advent of powerful supercomputers and consequently the possibility to develop global atmospheric models at high horizontal resolutions, the need to develop schemes which are capable of running efficiently on computers with thousands of processors and distributed memory became a new driving force in global atmospheric modelling. Especially for these high-resolution models, there has been a move towards finite-difference and finite-volume methods based on spherical grids that are not derived from spherical coordinates and also towards spectral element methods. Much effort is recently being devoted to development of new methods that could be applied to the grids known as quasi-uniform grids. These grids were an elegant solution to the pole problem, but in many cases were not competitive with existing models until the advent of distributed supercomputing. As a consequence, quasi-uniform grids were not largely used in operational atmospheric models until the mid-1990s. This new choice of the grid has allowed for the design of models which can be run at very fine resolutions on parallel computing systems.

The initial development of quasi-uniform grids dates back to 1960's and 1970s. In the mid-1960s, Buckminster Fuller's geodetic domes (MCHALE, 1962) inspired the development of spherical grids that were constructed by covering the sphere with almost uniform triangles. This type of grid is referred to as

spherical geodesic or icosahedral grid. Sadourny (1972) developed a method to cover sphere with several non-conformal projections which required no interpolations between meshes. The method is based on a regular polyhedron circumscribed to the sphere. A coordinate system is derived for each side for a gnomonic or central projection. He tested this approach with a cube for the polyhedron in which case the sides of the polyhedral faces are coordinate lines and grid points are common to the two sides defining the edge. This type of grid is referred to as cubed sphere.

The geodesic grids for atmospheric models were revisited by Masuda and Ohnishi (1986). Subsequently, Thuburn (1997) developed a shallow water model based on an icosahedral grid. Swarztrauber et al. (1997) developed a local method to solve differential equations in the sphere through Cartesian coordinates. They applied it to the shallow water equations using a geodesic grid. Stuhne and Peltier (1999) also developed a shallow water model on an icosahedral grid. More recently, the spherical geodesic grids were again taken up by several groups, which led to the development of several baroclinic cores based on those grids. For example, the Deutscher Wetterdienst effort led to the first operational model based on an icosahedral grid (GME), which replaced their earlier global spectral transform model. This model is described by Majewski et al. (2002), who also included a brief summary of the recent development of the icosahedral grid. Ringler et al. (2000) also produced a dynamic core based on icosahedral grid. It was based on the vorticity and divergence equations rather than the momentum equation. Tomita and Satoh (2004) developed a global non-hydrostatic model extending the regional formulation of Satoh (2002, 2003) using the icosahedral grid. Giraldo and Rosmond (2004) ultimately extended the method introduced in Giraldo (2001) to develop a dynamic core of spectral element with the horizontal operators discretized in Cartesian 3D space. By developing the equations in Cartesian coordinates, any grid can be used. They applied the model on an icosahedral grid and on a hexahedral grid.

Cubed sphere grids for atmospheric models were revived for atmospheric application by Ronchi et al. (1996) and Rančić et al. (1996). Ronchi et al. (1996) developed a method for the shallow water model, but instead of applying the cubic-gnomonic projection of Sadourny (1972), they used non-conformal mappings for the projected sides of the cube. Rančić et al. (1996) applied the Arakawa-type finite differences scheme on a B-grid to the shallow water equations on the cubed sphere. They also developed an alternative approach involving numerically generated conformal coordinates that are smoothed and continuous at the edges. This eliminates the directional discontinuity of the gnomonic projections at the edges of the cube. Purser and Rančić (1997) also developed a shaped octagonal grid. They demonstrated their viability with the same shallow water model as used in Rančić et al. (1996). Purser and Rančić (1998) proposed a variational method to generate smoothed quasi-homogeneous grids in order to increase the minimum grid distance of the cubic or octagonal grid in order to increase the maximum time step allowed by explicit schemes. This generalized their conformal cubic and octagonal grids. McGregor (1997) applied the semi-Lagrangian advection to the cubed sphere with the gnomonic projection with good results. McGregor (1996) also reported improvements when he applied his scheme to the conformal-cubic grid invented by Rančić et al. (1996).

Taylor et al. (1997) implemented the spectral method for the shallow water equations using gnomonic projections to map the sphere onto the cube. Giraldo and Rosmond (2004) also applied their spectral element baroclinic model on a cubed sphere. Adcroft et al. (2004) developed a dynamic core for application in atmospheric and oceanic models. They formulated it in general orthogonal curvilinear coordinates and applied the finite-volume method to the cubed sphere using the conformal mapping of Rančić et al. (1996). More details about the evolution of dynamical cores for global atmospheric models can be found in Williamson (2007).

Although the uniformity of grid spacing is inferior to the icosahedral grid

near the corner of each panel, this type of model has an advantage in the applicability to the regional prediction. Some trials have been done to cover the globe by plural limited area model domains. Dudhia and Bresch (2002) developed a global version of MM5 by combining two polar-stereo graphic projection domains and conducted one month simulation. Takahashi et al. (2005) developed the nonhydrostatic model MSSG (Multi-Scale Simulator for Geoenvironment) on a "Yin-Yang" grid system, which covers whole global surface by two rotated latitude-longitude grid domains and performed a high resolution (5 km) global simulation on the Earth Simulator. Purser et al. (2005) has also tested Yin-Yang approach with WRF-NMM model. Zhang and Rančić (2007) used similar approach, by combining the numerical infrastructure of the regional Eta model and the technique of quasi-uniform gridding of the sphere to create a global version of the regional Eta model, the so called Global Eta Framework (GEF).

2.4 Global Eta Framework (GEF) model

The current version of GEF uses a further improvement that provides an "equal-area" cubed-sphere, without angular discontinuities across the edges of the cube (PURSER; RANČIĆ, 2011; PURSER et al., 2014; RANČIĆ et al., 2017). The prognostic variables of the model are the same as in the regional Eta model: air temperature, zonal and meridional components of the wind, specific humidity, surface pressure, turbulent kinetic energy and cloud hydrometeors. Obviously, it uses the same vertical coordinate, eta, as the regional model (MESINGER, 1984). Thanks to the definition of the eta coordinate, the eta surfaces remain almost horizontal, which reduces the errors to estimate the pressure gradient force over steep terrain (MESINGER and JANJIC, 1985). This is treated as a major advantage compared to Phillips' sigma (σ) coordinate (1957) in the region which has the Andes Mountains. This feature can contribute to more accurate precipitation forecasts (MESINGER, 1996).

The horizontal coordinates of the cubic grids are strictly conformal far from the singularities. Close to the singularities, the conformality constraint is broken, and the coordinates become curvilinear. Purser and Rančić (1998) introduced the smoothed version of the cubic grid, with the largest minimum grid spacing. Consequently, the area where orthogonality is not applicable is also wider. Therefore, in order to correctly describe the flow in quasi-uniform grids, governing equations needed to be expressed in a curvilinear coordinate system (SADOURNY, 1972; RANČIĆ et al, 1996).

With regard to the numerical structure of the GEF model, the parameterization schemes are the same as in the regional Eta model. However, some of the numerical techniques require modification, or an adequate substitution, due to the use of curvilinear coordinates.

In the implementation in parallel computers, each element of the topological base is allocated to its own processor, so that the amount of data load and computation, at least in the code portion that describes the atmospheric dynamics, is equally distributed among the processors.

Arakawa's semi-staggered B-grid, used in GEF, substantially simplifies the indexing compared to the E grid, which is used in the regional Eta model. Since the B grid is equal to the E grid, rotated by a 45 ° angle, it is possible to apply the same numerical schemes that are efficient in the E grid. This method of applying numerical schemes from grid E to grid B was described by Janjić (1984). The points where the scalars are defined in the B grid are placed along the boundaries between the sides of the cube. This choice reduces the errors in the calculation of pressure gradient force at the edges of the cube, as pointed out by Rančić et al (1996). As in the Eta regional model, the variables are vertically staggered using a Lorenz distribution, with the temperature and momentum components defined in the middle of the layers, and the geopotential height and vertical velocity at the interfaces between the layers. The non-linear advective terms in the momentum equation are discretized using the Arakawa-type scheme (JANJIC, 1977). For the other members, second-order finite difference scheme in space is applied for the mass. Energy

conservation is applied. A gravity-wave coupling scheme developed by Mesinger (1973), Mesinger (1974), and Janjic (1979) is used in the regional Eta model dynamics to eliminate two-grid-interval noise, as a consequence of separation of solutions on the elementary C subgrids. This technique is adjusted to be used in curvilinear coordinates in GEF. A scalar point located in a corner of the cube has only three velocity points around itself, and within the code it is treated equally like all other points by constructing an artificial "ghost" space in the missing area location and with the values set to zero. This technique is formally equivalent to a finite volume reformulation consisting of vector operators in the corners (RANČIĆ et al., 1996) and allows the conservation of mass, total energy and vorticity of the general flow (but not the non-divergent part of the flow).

The model uses the same explicit scheme for integration in time, as the regional Eta model, with the time step of geostrophic adjustment, being half the time step applied in the advection processes. The forward-backward scheme is applied to the gravity wave terms and the implicit trapezoidal scheme to the Coriolis term (MESINGER, 1977; JANJIC, 1979). Instead of updating the continuity equation with the forward scheme and the momentum equation with the backward scheme, as it is done in the regional Eta model, the order is reversed and the forward scheme is applied in the equation momentum and the backward scheme in the continuity equation. Rančić and Zhang (2002) found this to be more accurate. The multidimensional scheme of Smolarkiewicz and Grabowski (1990), which corrects the flow, is applied to the horizontal advection of water vapor and cloud water.

The physics package implemented in the GEF model is the same as the regional Eta model package, with minimal modifications. For parameterization of radiation, the model uses the Geophysical Fluid Dynamics Laboratory (GFDL) scheme (LACIS; HANSEN, 1974; FELS; SCHWARZKOPF, 1975). Soil surface temperature and humidity are predicted by the land surface NOAH scheme described in Chen et al. (1997) and Ek et al. (2003). Sea surface temperature is prescribed by NCEP analysis. Cloud and ice water are explicitly treated as

prognostic variables by the Ferrier et al. (2002) scheme. As in the regional Eta model, two cumulus convection schemes are optionally available: the Betts-Miller-Janjic scheme (BETTS, 1986; BETTS; MILLER, 1986; JANJIC 1990) and the Kain-Fritsch scheme (KAIN; FRITSCH, 1990). Turbulent processes in the free atmosphere are treated using the Mellor-Yamada level 2.5 scheme in which the turbulent kinetic energy is prognostic. The Mellor-Yamada 2.0 level scheme is used in the first layer of the model to represent the turbulence in the surface layer.

2.5 Ferrier cloud microphysics parameterization scheme

A cloud microphysics scheme developed by Ferrier et al (2002) is used in the Eta regional model. The same scheme is used in the GEF model. The scheme was formulated to predict the variation of six forms of the water substance. The scheme represents the cloud and rain of the grid scale of the model. It predicts cloud water variation in the form of: water vapor, cloud water, cloud ice, snow, hail and sleet. It predicts the changes in the specific humidity and total condensation, which is the sum of cloud water (small non-precipitating drops), rain (large drops) and cloud ice. All can coexist at temperatures higher than -10 °C. The ice category is formed of small ice crystals, which are dominant in cirrus clouds in the upper troposphere, and of larger particles in the form of snow (pellets), ice pellets, graupel, and hail, which are dominant in the lower levels. The changes between water vapor and cloud condensation are determined based on the algorithm proposed by Asai (1965). Precipitation is predicted by integrating precipitation fluxes from the top of the cloud to the surface. It is divided into local storage, proportional to the thickness of the layer and precipitation that falls through the base of the model grid. Precipitation can be in the form of rain, frozen rain, and ice. The density of the ice varies depending on the formation process. Ice can be of low density obtained by freezing cloud water or sleet over the low density snow ("fluffy" snow), or of high density obtained by freezing of melted snow or supercooled cloud water (ice

pellets/graupel). Mixed phase states are considered to occur at temperatures between 0°C and -10 °C. In lower temperatures, it is assumed that the supercooled rain freezes forming hail and the supercooled droplet freezes forming cloud ice. The latent heat associated with melting of the water ("riming") on ice, freezing supercooled rain, and the melting of all ice particles are considered. The cloud microphysical processes considered by the scheme are: condensation/evaporation of cloud water, deposition/sublimation of ice crystals, collection of cloud water by precipitation, growth of precipitation of ice by riming, aggregation of cloud water to form rain, freezing rain on large ice particles at super low temperatures, condensation on melting ice, melting ice, autoconversion of cloud water into rainfall, collection of cloud water for rainfall, and rain evaporation.

2.6 Kain-Fritsch (KF) parameterization scheme for convection

The KF parameterization scheme is based on mass flux. The scheme represents the mass exchange between the cloud and the environment, which causes heating and drying in the cloud layer. This process is performed through the one-dimensional cloud model by the amount of rising air. The KF scheme assumes the entrainment and detrainment of the air at several levels of the cloud layer that causes an exchange between the environment and the cloud.

An advantage of the KF scheme is that the detrainment effect simulation is more realistic. The parameterization also guarantees the conservation of mass, thermal energy and momentum. In order to trigger the convection in this scheme, it is necessary to have air of sufficiently high values of CAPE originating from low levels and thickness between the surface and the lifted condensation level (LCL) of not more than 50 hPa. Once the convection is triggered, available energy is reduced at a specific time, using an air-cloud mixing scheme to calculate the mixing rates.

The KF scheme has an appropriate assumption about the time scale to consume the CAPE. The scheme has more details about convective processes

and is able to perform better in severe convective cases, then Fritsch-Chappell scheme (FRITSCH; CHAPPELL, 1980), from where it is derived. It is not recommended for use in low resolution models due to the strong consumption of CAPE. Thus, it is more suitable for mesoscale models and to be coupled with systems that use cloud microphysics.

3 SEASONAL RANGE INTEGRATIONS

3.1 Literature review

3.1.1 Monsoonal characteristics

Based on characteristic atmospheric circulation features and their evolution, it is demonstrated by Zhou and Lau (1998) that the monsoon system does exist over South America. Some other studies related to precipitation and circulation regimes over the continent are documented in Nogués-Paegle et al. (2002) and Vera et al. (2006). Probably the most recognizable characteristic of every monsoon is the seasonal cycle of precipitation. Well defined wet season during austral summer (DJF) and dry season during austral winter (JJA) represent the typical precipitation pattern over tropical South America (RAO et al., 1996; GAN et al., 2004). The period of transition from dry to wet season occurs in austral spring (SON) and it is characterized by a rapid southward shift of the region of intense convection from the Caribbean and northwestern South America to the southern Amazon Basin and Brazilian highlands (Planalto) in October and further to southeast Brazil in November. At onset of the rainy season, the South Atlantic High moves eastward, reflecting the pressure reduction over the continent and change of the intensity and direction of the zonal flow over the nearby tropics and sub-tropics (MARENGO et al., 2010). Also, the moisture from the Atlantic Ocean brought by the easterlies together with the moisture from evapotranspiration from the Amazon rainforest is transported by low-level jet in the east of the Andes to the central and southeastern Brazil (RAO et al., 1996). The presence of more humidity in these regions leads to the development of deep convection. During the austral summer (DJF), the maximum of rainfall intensity occurs over much of tropical South America (FIGUEROA; NOBRE, 1990; RAO; HADA, 1990).

3.1.2 Monsoonal onset

Many studies were performed to define the onset and demise dates for the South American monsoon, where several criteria were applied. Some of the criteria are based on OLR (KOUSKY, 1988; GONZALES et al., 2007; GARCIA; KAYANO, 2009), some only on precipitation (LIEBMANN; MARENGO, 2001; MARENGO et al., 2001), while some others use a combination of wind and precipitation (GAN et al., 2004). The onset and demise of the rainy season are also evaluated by monsoon indices based on the dynamical aspects of the atmosphere in Gan et al. (2006), by Large-Scale Index for South American Monsoon (LISAM) that consists of combined EOFs (empirical orthogonal functions) using anomalies of precipitation, specific humidity, air temperature, and zonal and meridional winds at 850 hPa (SILVA; CARVALHO, 2007), or by atmospheric humidity flux over an area recognized as the monsoon core, because of zonal wind reversal and changes in humidity in transition seasons (RAIA; CAVALCANTI, 2008). Although these methods employ different atmospheric variables, they mostly agree in definition of the mean onset date for South American Monsoon System (SAMS), showing only small differences (MARENGO et al., 2010).

3.1.3 Monsoon simulations

There are various documented studies about model simulations of SAMS integrated on seasonal and climate scale. Coupled Global Circulation Models (CGCMs) of World Climate Research Project – Coupled Model Intercomparison Project (WCRP-CMIP3) for the 20th century make reasonable results, comparable with observations, nevertheless with difficulties in representing precipitation and duration of the rainy season in some regions (BOMBARDI; CARVALHO, 2009) or position and intensity of Intertropical Convergence Zone (ITCZ) and South America Convergence Zone (SACZ) in an ensemble integration (SETH et al., 2010). Vera and Silvestri (2009) examined interannual

seasonal variability and informed about problems in representing the variability associated with the South Atlantic convergence zone during summer, pointing out the necessity for model improvement. Jones and Carvalho (2013) used the CMIP5 models and confirmed improvement in comparison with CMIP3 models in simulation of SAMS. An Atmospheric Global Circulation Model (AGCM), ECHAM 4.5, evaluated in Liebmann et al. (2007) demonstrated skill in representing the onset of SAMS in some regions and for some years during the period of 1976 to 2001. CPTEC-COLA AGCM (CAVALCANTI et al., 2002) represented well the large scale characteristics of SAMS in the summer season, but had difficulties in simulating precipitation, with underestimate over Amazon region and overestimate in the Andes region. An upgraded version of CPTEC-COLA AGCM used in Cavalcanti and Raia (2017) was able to represent well the main observed features of the SAMS lifecycle, improve precipitation and capture the change of humidity flux direction. However, simulations also indicated later onset and produced delay in wind reversal. There are also documented simulations using regional models, which mostly represent well the large-scale features of the SAMS (CHOU et al., 2005; SETH et al., 2006; ROCHA et al., 2009*).*

The objective of this chapter is to evaluate the capability of the Global Eta Framework (GEF) at a 25 km horizontal resolution, to simulate the onset of the rainy season in Western-Central Brazil (WCB) in a 5-member ensemble seasonal integration. In the next section, initial results are discussed. In section 3.3 we describe the model, seasonal simulation setup and the dataset used in this study. Section 3.4 shows the large-scale circulation patterns and section 3.5 shows the analysis of pentad averages of rainfall and OLR. In section 3.6, the model skill to simulate diurnal cycle of precipitation over South America is evaluated. We finish with the section 3.7 with the summary and conclusions of the chapter.

3.2 Initial results and discussion

A preliminary evaluation reported in Latinović et al. (2013) showed model capability to simulate extreme climate events and stability in long-term, low resolution (approximately 230 km) climate type runs. With a new, "equal-area" grid and increased resolution (25 km), continuous seasonal (90-day) runs were performed (Figure 3.1). The initial condition was taken at 0000 UTC 9 February 1996. Figure 3.1 shows the globally averaged 850-hPa temperature, 850 hPa wind and 200-hPa wind from GEF simulation in comparison against ERA-Interim reanalyses (DEE et al., 2011). The time series of 850-hPa temperature show that the global mean values are slightly underestimated when compared with reanalyses, although they follow the trend of seasonal increase/decrease, as in the reanalyses. In addition, the simulated time series of 850 hPa temperature shows a phase lag of a few days at the beginning of integration before it reaches the state of equilibrium and later it continues to vary about 1–2 °C lower than the reanalyses. The significant difference between GEF and ERA-Interim temperatures at the beginning of the integration may be due to of different discretization and vertical interpolations of temperature in GEF. The model uses geopotential height to calculate temperature and vertically interpolates it to the mid-layers of the model. In the post-processing phase, another vertical interpolation is applied to the temperature from model levels to the standard pressure levels. GEF wind magnitude agrees reasonably with the reanalysis both in the lower and upper troposphere. The 850-hPa mean wind simulation follows approximately the reanalysis, but mostly underestimates and occasionally overestimates, especially at the beginning of integration, when the differences reach at most 1.5 m s^{-1}. In contrast, the simulated 200-hPa mean wind shows underestimate by up to 4 m s^{-1}. Figure 3.2 shows that the global pattern of the seasonal mean precipitation agrees relatively well with the observed precipitation from GPCP (Global Precipitation Climatology Project). However, model produces a significant overestimate, mostly in the tropical oceanic regions, and produces some underestimate in the tropical continental

regions, especially in parts of Africa and South America, where it fails to represent typical pattern of precipitation over each continent. These results show the model ability to perform simulations at an increased horizontal resolution using an upgrade of the cubed-sphere, and demonstrate the model robustness in the long-term, seasonal run. Zhang and Rančić (2007) showed robustness for medium range at low resolution and these results show the model also has skill in longer, seasonal runs. It is important to mention that this is the first seasonal run made with the GEF. Further adjustments in convective parameterization schemes are planned in order to improve precipitation simulation and the further increase of horizontal resolution.

Figure 3.1: February to April (FMA) 1996 time series of global mean variables from ERA-Interim reanalyses and simulated by GEF: (a) 850-hPa temperature (°C) (the green curve is GEF and the red curve is the reanalysis) and (b) 850-hPa wind (ms^{-1}), and (c) 200-hPa wind (ms^{-1}) (the blue curves are GEF and the orange curves are the reanalyses).
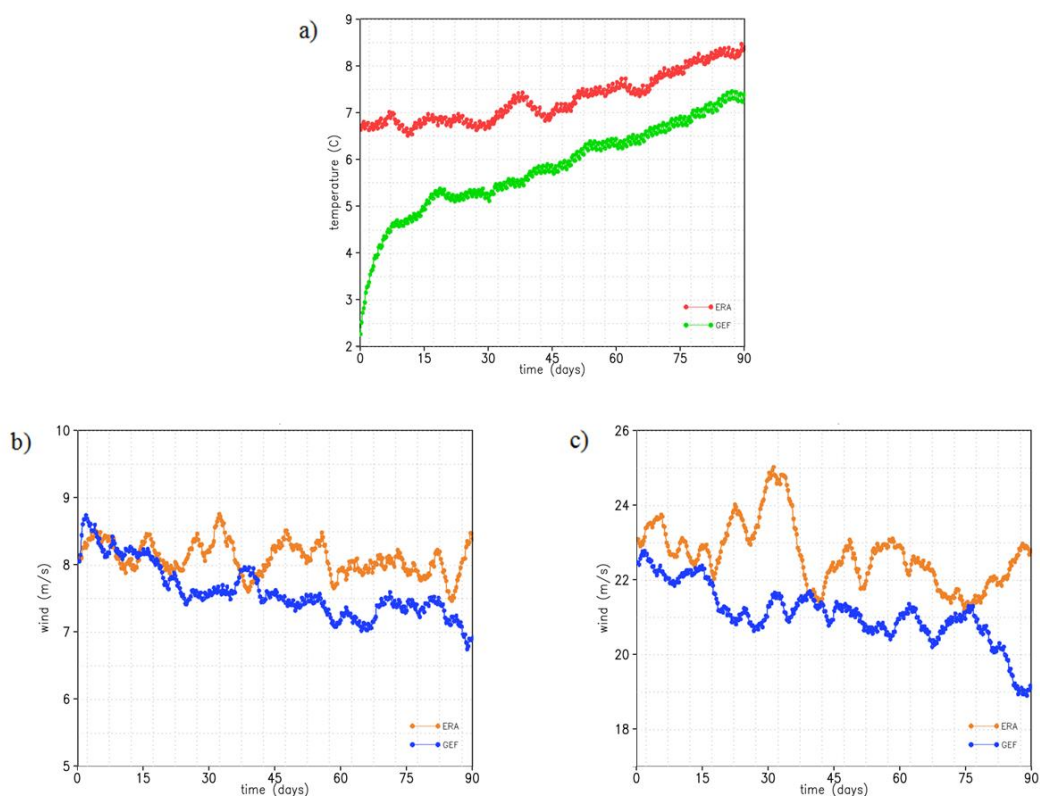
Source: Latinović et al. (2017)

The initial results show that GEF is capable of reproducing seasonal mean characteristics of the atmosphere. It is important to point out that all simulations were performed with relatively modest use of computational resources, 600 processor cores.

Figure 3.2: February to April (FMA) 1996 mean precipitation (mm day^{-1}) from GEF (a) and GPCP (b).
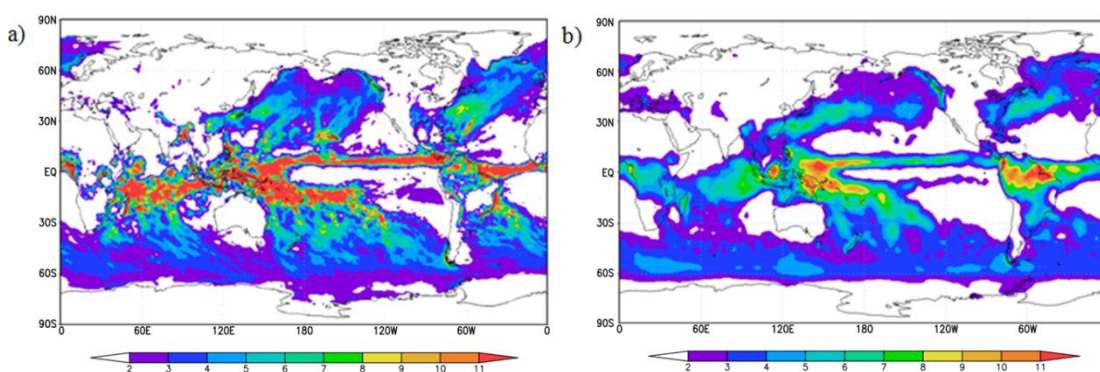
Source: Latinović et al. (2017)

3.3 Model specification, methods and data

Model description is provided again in this section for completeness of the description of the seasonal runs. Global Eta Framework (GEF) is a global atmospheric model, based on general curvilinear coordinates, capable of running on various rectangular spherical grids. It is developed by Zhang and Rančić (2007). The version of the model used in this study is based on cubed-sphere grid topology, originated by Sadourny (1972). The standard longitude-latitude grids require Fourier filtering around the poles, which degrades computational efficiency. With the development of massively parallel computers, emerged again the interest in application of quasi-uniform grids in AGCMs. Due to its uniformity and the geometrical symmetry, cubed-sphere, as a representative of quasi-uniform grids, came into focus again during 1990s. There are many documented improvements of the original gnomonic cubed-

sphere from that period, starting from conformal cubed-sphere, described in Rančić et al. (1996), Ronchi et al., (1996) and McGregor (1996), over the smoothed version developed by Purser and Rančić (1998) and used in the first version of GEF in 2007, until current version that provides an "equal-area" cubed-sphere, without angular discontinuities across the edges of the cube (PURSER; RANČIĆ, 2011; PURSER et al., 2014; RANČIĆ et al., 2017). GEF is created as a combination of the technique of quasi-uniform gridding of the sphere and the numerical structure of the regional Eta model (MESINGER et al., 1988; JANJIC, 1990; JANJIC, 1994; BLACK, 1994; CHOU et al 2002, 2012; MESINGER et al., 2002; PESQUERO et al., 2010; MESINGER et al., 2012; LYRA et al., 2017; MESINGER; VELJOVIC, 2017) therefore it represents a unique global version of the regional Eta model. Six regional models, interconnected through the cubed-sphere framework are integrated simultaneously, one on each side of the cube, to provide a global coverage and to create the global model – GEF.

The Eta is a regional atmospheric model used for weather and climate forecasts for South America at CPTEC/INPE. One of the main features of its dynamical core is the eta vertical coordinate (MESINGER, 1984), with quasi-horizontal coordinate surfaces that reduce pressure-gradient force errors due to steep topography, which is a typical error which appears in terrain-following coordinates. The physics package of the code includes a choice of two convection schemes, Betts-Miller-Janjic (BETTS; MILLER, 1986; JANJIC, 1994), and Kain-Fritsch (KAIN, 2004) and two cloud microphysics schemes, Zhao (ZHAO et al., 1997) and Ferrier (FERRIER et al., 2002). The radiation package is developed by GFDL (Geophysical Fluid Dynamics Laboratory), with short-wave radiation scheme of Lacis and Hansen (1974) and long-wave radiation scheme of Schwarzkopf and Fels (1991), with radiation tendencies calculated every hour and applied at every time step. The land–surface transfer processes are parameterized by the Noah scheme (EK et al., 2003). Monin–Obukhov similarity theory is combined with Paulson stability functions (PAULSON, 1970) and applied at the surface layer to describe the logarithmic wind profile and

coupled to molecular sublayer over land and ice according to Zilitinkevich (1995), and over water according to Janjic (1994). Turbulence transports above the surface layer use the Mellor-Yamada 2.5 closure (MELLOR; YAMADA, 1982; JANJIC, 1990). More details about the Eta model and its recent improvements, that include refined vertical coordinate system using "sloping steps" and the implementation of the fully finite-volume dynamics, are documented in Mesinger et al. (2012).

The step-terrain approach is especially important for the areas where weather conditions are strongly affected by high mountains, such as the Andes in South America. Therefore, the use of GEF in this study seems very appropriate since it uses the eta vertical coordinate, although the current version of GEF still does not employ "sloping steps" (MESINGER et al., 2012). Since the beginning of the CPTEC operational activities, a spectral global model (BONATTI, 1996) has been used to provide weather and seasonal climate forecasts, with new versions being developed and released along the years. Current version of global atmospheric model used by the centre (FIGUEROA et al., 2016) serves for weather forecasts. The global seasonal forecasts at CPTEC are produced by an ensemble of the global atmospheric model (AGCM), with the latest results being discussed in Cavalcanti and Raia (2017), an ensemble of coupled ocean-atmosphere model (SIQUEIRA; NOBRE, 2006), and an ensemble of the regional Eta model (CHOU et al., 2005; PILOTTO et al., 2012). The high computational demand of the spectral model for long-term simulations limits the CPTEC global models to the coarse resolution of about 200 km. The GEF development at CPTEC for seasonal forecasts is a less computationally demanding alternative for the operational seasonal forecasts at the centre (LATINOVIĆ et al., 2017).

The model was set up at 25-km horizontal resolution and 38 vertical levels, with model top at 25 hPa, time step 40 s, and it uses Ferrier cloud microphysics scheme, Kain-Fritsch convection scheme and GFDL radiation package.

This study performs a comparative assessment of simulated and

observed seasonal conditions for the trimester September-October-November (SON) of the years 2011 and 2013 with emphasis on the evaluation of the model skill to simulate the onset of the rainy season in the region of WCB (20°S-10°S, 60°W-50°W). For that purpose, the methods based on pentads of precipitation and OLR were applied. The rainy seasons of both selected years ended with extreme floods in the Amazon region, which is the motivation to use them in this study. A total of 10 seasonal integrations were performed, for the range of approximately 4 months, creating ensembles of 5 members for each season. Members of ensemble are constructed using initial conditions from NCEP reanalyses (KALNAY et al., 1996; KANAMITSU et al., 2002) at 0000 UTC from the days 13, 14, 15, 16 and 17 August of each year. Sea surface temperature (SST) is updated daily by interpolating from the observed monthly mean global SST (REYNOLDS et al., 2002) for each year, similarly as vegetation fraction, which is also updated daily but from monthly mean climatological values. Depending on the member of ensemble, approximately 2-3 weeks model spin-up period was considered for both years. The period analyzed in section 3.4 spans from 1st of September until 30th of November (SON). For the evaluation of the onset of the rainy season in the section 3.5, it spans from the pentad 49 until pentad 66 (29th of August-26th of November). Pentads represent mean values of 5 consecutive days, starting from 1st of January, where pentad 1 represents the mean value for the days 1st-5th of January, pentad 2 represents the mean value for the days 6th-10th of January, therefore one year consists of 73 pentads, as presented in Kousky (1988). The corresponding dates of the pentads used in this study are listed in Table 3.1. Evaluation of precipitation simulation is made by comparing against NCEP reanalysis data and CMORPH (CPC MORPHing technique) precipitation data (JOYCE et al., 2004).

Table 3.1: Pentad numbers and corresponding dates for the pentads 49-66.

Pentad	Dates	Pentad	Dates
49	29 Aug. - 2 Sep.	58	13-17 October
50	3-7 September	59	18-22 October
51	8-12 September	60	23-27 October
52	13-17 September	61	28 Oct. - 1 Nov.
53	18-22 September	62	2-6 November
54	23-27 September	63	7-11 November
55	28 Sep. - 2 Oct.	64	12-16 November
56	3-7 October	65	17-21 November
57	8-12 October	66	22-26 November

Source: Adapted from Kousky (1988)

3.4 Large-scale circulation patterns

In this section, the large-scale circulation patterns simulated by GEF are discussed, with focus on South America. Global ensemble mean values of 200-hPa and 850-hPa wind, 500-hPa geopotential height, 850-hPa temperature, mean sea level pressure (MSLP) and precipitation are compared against corresponding reanalyses and observations of the SON trimester of 2011 and 2013. In most of the cases, model has similar performance for both years. Some local discrepancies between the two years appear occasionally and they will be highlighted.

Figure 3.3: September to November (SON) 2011 and 2013 global ensemble mean 200-hPa and 850-hPa winds (m s^{-1}), GEF simulations (on the left) and NCEP reanalyses (on the right). Wind speed is shaded and direction is shown by streamlines. Top panel refers to 200-hPa wind (m s^{-1}) in 2011, the second panel shows 200-hPa wind (m s^{-1}) in 2013, the third panel shows 850-hPa wind (m s^{-1}) in 2011 and the bottom panel shows the 850-hPa winds (m s^{-1}) in 2013.
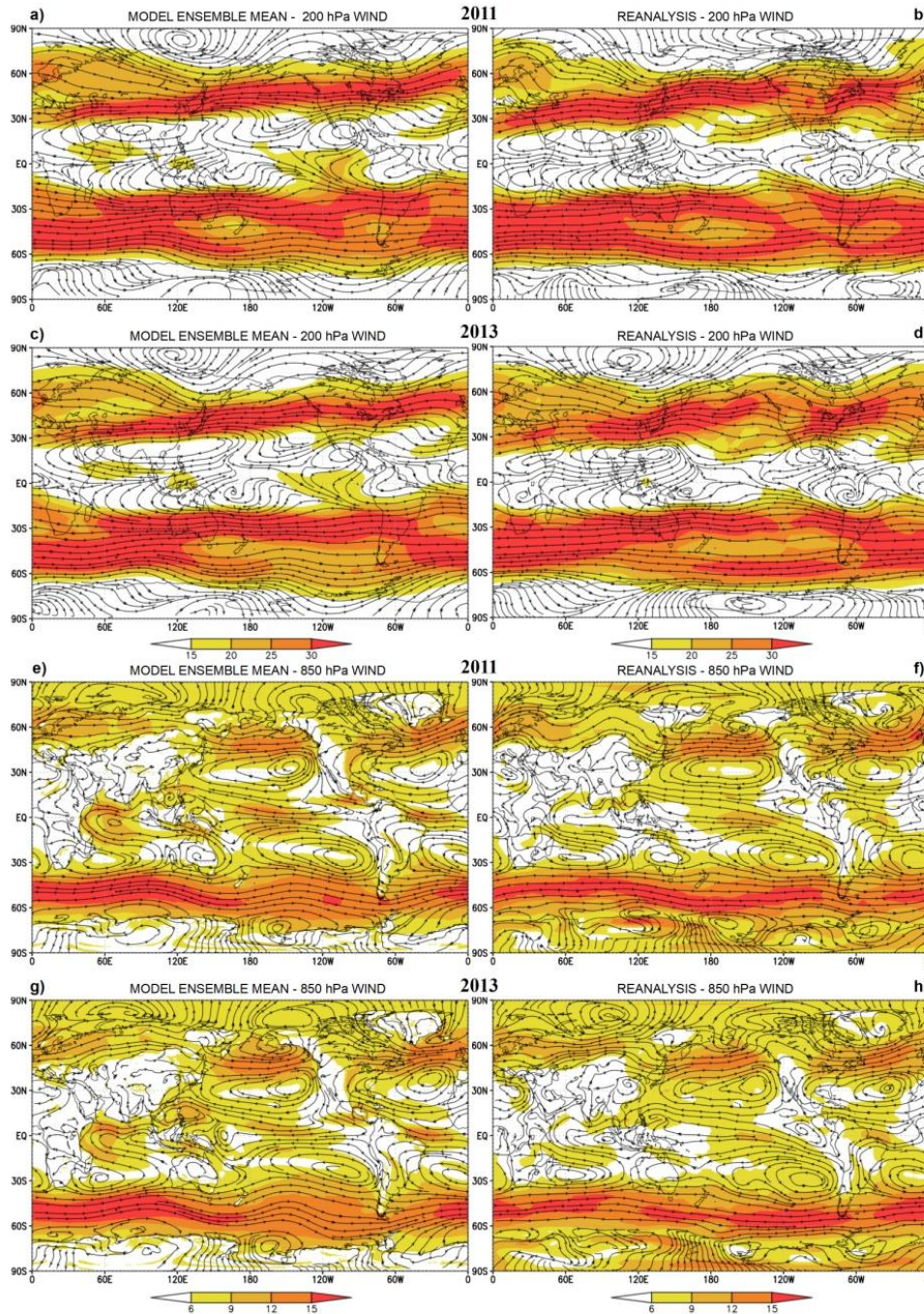
Figure 3.3 shows circulation in the upper (200 hPa) and lower (850 hPa) troposphere where model shows good performance in terms of wind intensity (shaded) and direction (streamlines). There are some disagreements in the reproduction of intensity of the jet streams over North America and over South Pacific, where model tends to simulate weaker winds. On the other hand, the model simulates stronger winds western equatorial Indian Ocean and in eastern equatorial Pacific (Figure 3.3 a-d). The monsoonal changes in the upper levels, typical of austral spring over South America, are also present in the form of developed anticyclonic circulation, although, a bit displaced in 2013 case. Lower-level circulation characteristics that include easterlies over the tropics, the subtropical anticyclonic circulation, the mid-latitude westerlies and the subpolar lows are reproduced by the model (Figure 3.3 e-h), although the centres of the subtropical highs and the subpolar lows are slightly displaced toward east. Wind intensity is mostly comparable with reanalysis, except in the western Indian Ocean, where wind speed is overestimated. More pronounced wave-like pattern is simulated in the mid-latitude westerlies in the southern hemisphere for both years and the absence of waves over part of Europe and Asia in 2011. Easterlies over the Atlantic Ocean, close to the coast of South America are more intense in the simulation. The low-level jet east of Andes, which is one of the characteristic features of the South American monsoon, is clearly simulated by the model. However, the model simulates a northwest-southeast orientation of the wind jet whereas the reanalysis has north-south orientation.

Figure 3.4: September to November (SON) 2011 and 2013 global ensemble mean 500-hPa geopotential height (gpm) (contour) and 850 hPa temperature (°C) (shaded) simulated by GEF (on the left) and global means of the same variables from NCEP reanalyses (on the right). Top row refers to 500hPa geopotential height (gpm) in 2011, the second row shows 500-hPa geopotential height (gpm) in 2013, the third row shows 850-hPa temperature (°C) in 2011 and the bottom row shows 850-hPa temperature (°C) in 2013.
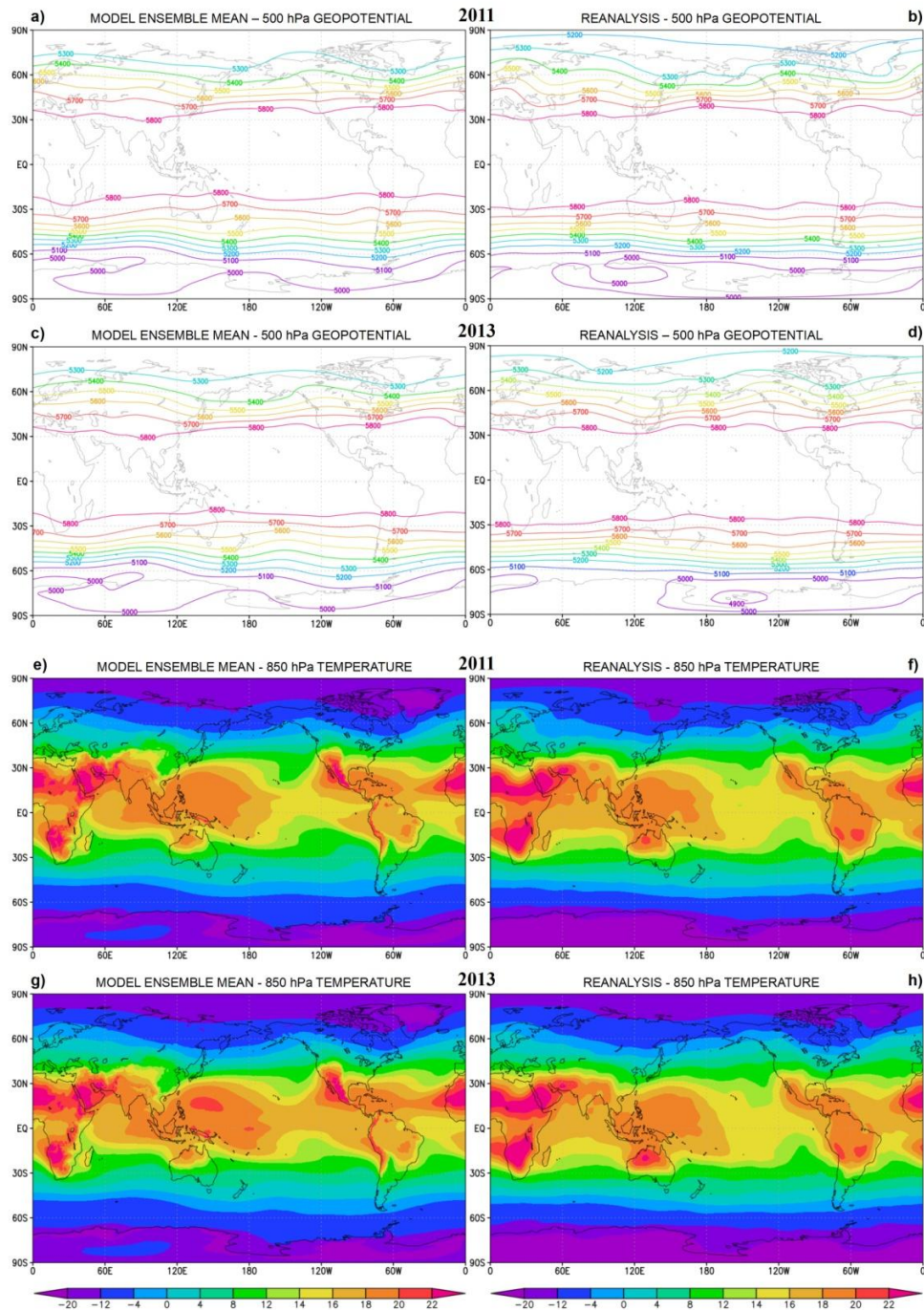
The simulated 500-hPa geopotential height and 850-hPa temperature show the best agreement between the model and reanalysis. Table 3.2 shows the high values of spatial correlation, 0.99 for 500-hPa geopotential height and 0.98 for 850-hPa temperature for both years. Major 500-hPa geopotential height differences are shown in polar regions and at 5700 and 5800 gpm in the southern hemisphere, which are shifted northwards when compared against reanalysis (Figure 3.4 a-d). At 850 hPa, temperature error is largest over the Pacific coast of Mexico (Figure 3.4 e-h), where model overestimates the temperature by about 4°C. Overestimate of 2°C is shown mostly over the equatorial oceanic regions in the eastern Indian Ocean and central Pacific, Atlantic Ocean and over Caribbean Sea. Simulations also overestimate the 850-hPa temperature by about 2°C over western Pacific Ocean in 2013. In contrast, the temperature over tropical continental regions is mostly underestimated by about 2°C over equatorial Africa, northern Australia and tropical regions of South America.

Table 3.2: Spatial correlations of daily mean global simulations and CMORPH observations for precipitation (mm day^{-1}) and the NCEP reanalyses for other variables, for the SON of 2011 and 2013.

variables / trimester	200-hPa wind (m s^{-1})	500-hPa geopotential height (hPa)	850-hPa temperature (°C)	850-hPa wind (m s^{-1})	MSLP (hPa)	precipitation (mm day^{-1})
SON 2011	0.89	0.99	0.98	0.86	0.89	0.64
SON 2013	0.88	0.99	0.98	0.85	0.88	0.64

A belt of high pressure system is shown in the mid-latitudes by the simulations. The pressure magnitude is reasonably simulated, but underestimated over south-eastern Pacific Ocean in 2013 (Figure 3.5 a-d). The surface high pressure centres of the subtropical anticyclones are displaced eastward especially over the Pacific Ocean in 2011. Subpolar lows, especially

in the southern hemisphere are not so deep as in reanalysis, and the position of the centres are also mainly displaced. In the Amazon region, the simulated 1010 hPa isobar spans over a larger area when compared with reanalysis. Despite mentioned differences, the MSLP field holds the third position in spatial correlation coefficients, when compared with all other analyzed fields (Tab. 3.2). The spatial correlations for both MSLP and 200-hPa wind are 0.89 and 0.88 for the years 2011 and 2013. The 850-hPa wind correlations are 0.86 and 0.85, for 2011 and 2013, respectively. Spatial correlations of precipitation of 0.64 for both years can be considered reasonably good. Despite the lowest correlation, model precipitation patterns show reasonable agreement with the high resolution CMORPH observations (Figure 3.3 e-h). The ITCZ is correctly positioned across the Pacific Ocean and over the Atlantic and Indian Oceans and the Maritime continent. However, precipitation rate is underestimated over central Pacific, over tropical South America and Africa and overestimated over Central America, Indian Ocean and over the western Pacific. The South Pacific Convergence Zone (SPCZ) that extends from the equatorial west Pacific southeastward across the south Pacific Ocean is correctly positioned. The simulated precipitation rate is also comparable to observations precipitation intensity. Similarly, the precipitation band over South Atlantic that extends from South America also has the quantities comparable to the observations. The weak precipitation areas in the southern hemisphere mid-latitudes are slightly overestimated by the model, while in the northern hemisphere mid-latitudes, the precipitation maxima along and off the eastern coasts of the continents are mostly well represented both in position and intensity. The simulations reproduce the precipitation minima in the mid-latitudes, which correspond to the positions of subtropical highs and the desert regions over the continents along the latitudes of 20°. Model precipitation pattern over South America reproduces the initial phase of onset of the rainy season which is indicated by the spatial distribution of precipitation, although the intensity of precipitation is clearly underestimated, especially over the Amazon region and the La Plata river basin. Global models generally show dry bias in these two regions (YIN et al., 2012).

Figure 3.5: 2011 and 2013 SON global ensemble mean MSLP (hPa) (contour) and precipitation (mm day^{-1}) (shaded); GEF simulations (on the left) and NCEP reanalyses and observed precipitation (mm day^{-1}) from CMORPH (on the right). Top row refers to MSLP (hPa) in 2011, the second row refers to MSLP (hPa) in 2013, the third row shows precipitation (mm day^{-1}) in 2011 and the bottom row shows precipitation (mm day^{-1}) in 2013.
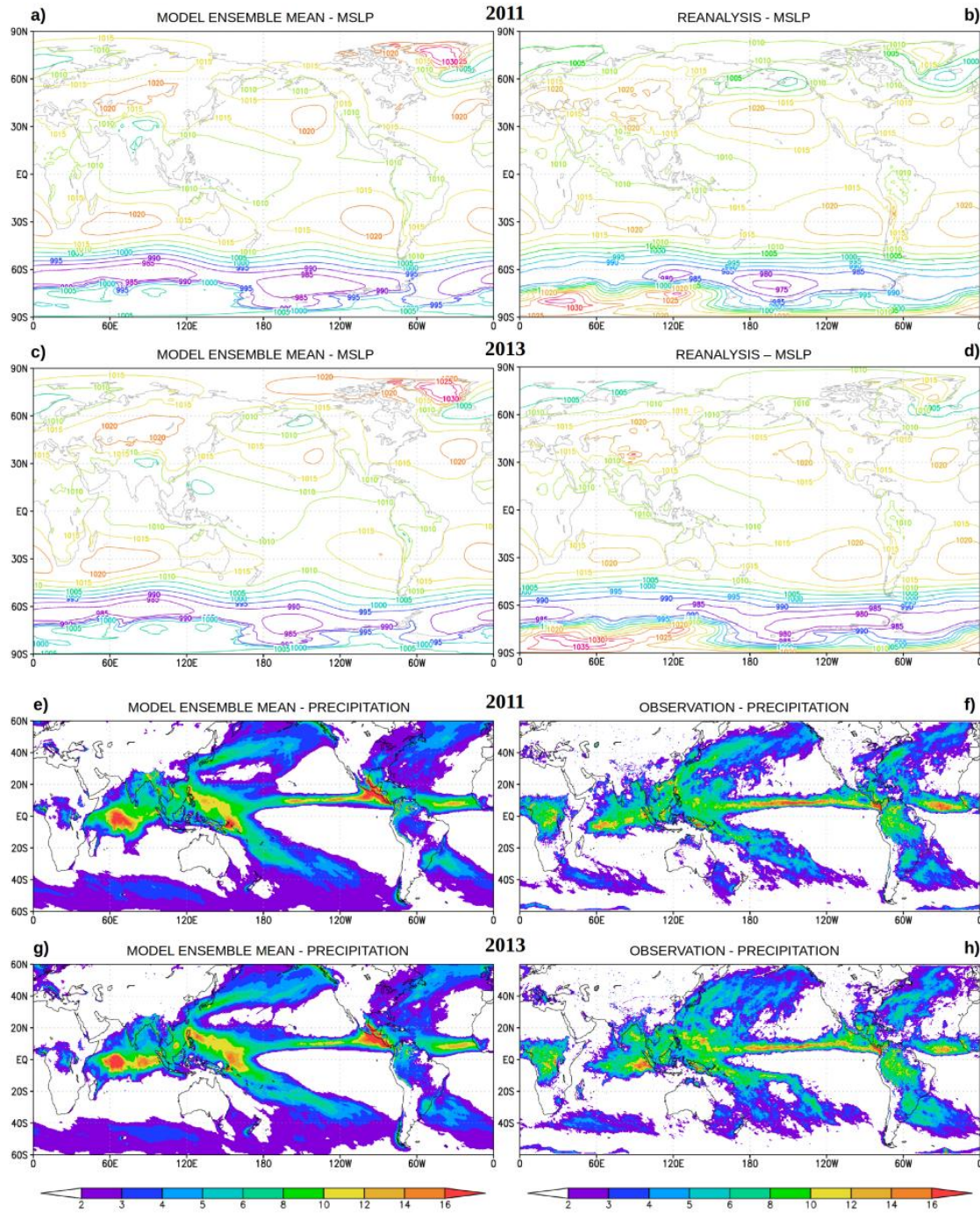
3.5 Analysis of the onset of the rainy season in Western Central Brazil

The definition of the onset of the rainy season in this study is based on precipitation and OLR. Marengo et al. (2001) defined the pentad that represents the onset of the rainy season as the one with daily precipitation greater than 4 mm day^{-1}, preceded with at least 6 out of 8 pentads with daily precipitation less than 3.5 mm day^{-1}, and followed by at least 6 out of 8 pentads with daily precipitation of more than 4.5 mm day^{-1}. The criteria of preceding and subsequent pentads are included due to the fairly noisy character of precipitation and the objective to capture correctly the transition from dry to rainy season. For example, a pentad with an episode of heavy rain, followed by a few pentads with precipitation below the defined threshold, cannot be qualified to define the onset.

A similar method is based on the OLR. Kousky (1988) defines onset as occurring when mean OLR falls below 240 W m^{-2} in a given pentad, provided that 10 out of the 12 previous pentads have OLR above 240 W m^{-2} and 10 out of the 12 subsequent pentads have OLR below 240 W m-2. The WCB region selected for this study (Figure 3.6) includes the area of maximum precipitation during the rainy season (DJF). The mean annual cycle of circulation is highly related to SAMS, as demonstrated in Gan et al. (2004). The authors pointed out remarkable seasonality in annual precipitation for the selected region (WCB) and the contrast between the summer and the winter precipitation patterns from more than 900 mm year^{-1} during summer (DJF) and less than 100 mm year^{-1} during winter (JJA) season. This region is also important because it contains the western portion of the Brazilian High Plains together with some rivers that flow into the Amazon and La Plata basins. This area is frequently used in studies related to SAMS to define the onset or demise of the rainy season (GAN et al, 2006; GARCIA; KAYANO, 2009; GARCIA; KAYANO, 2011).

Figure 3.6: Study area to define the rainy season onset, Western-Central Brazil (WCB), 10°S–20°S/60°W–50°W.
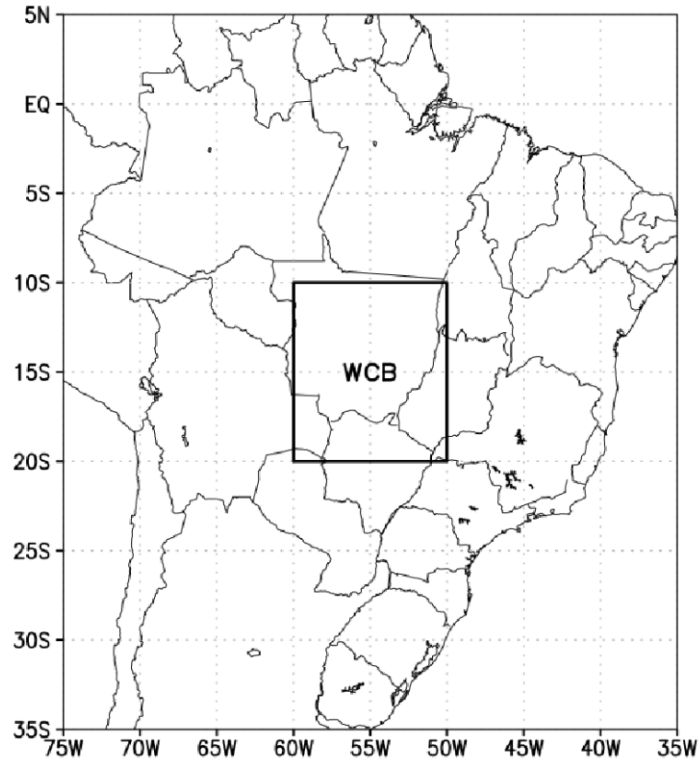
The onset dates for the years 2011 and 2013 are calculated (Figure 3.7). The two highly correlated curves refer to the NCEP reanalysis OLR data (red line) and the CMORPH precipitation (green line). The X-axis shows pentads from 1 to 73. The y-axis on the left corresponds to precipitation in mm day^{-1} and the inverted y-axis on the right corresponds to OLR in W m^{-2}. Black solid horizontal line represents the thresholds, both for precipitation (4 mm day^{-1}) and OLR (240 W m^{-2}). Both methods agree in the indication of the pentad that defines the onset, the pentad 55 (black vertical dashed line), that corresponds to the period between 28 September and 2 October, which coincides in both years. However, that is not the common situation. If the demise dates had to be defined, for example, the methods would give different pentads. For the precipitation method, they would be the pentad 21 in 2011 and the pentad 22 in 2013 whereas for the OLR method, they would be the pentad 22 in 2011 and

the pentad 25 in 2013. The first observed peak in precipitation and OLR above the defined threshold in 2011 (pentad 55) indicates the onset, while the first observed peak in 2013 (pentad 50) is followed by 4 consecutive pentads with the values below the threshold, thus does not qualify to be treated as the onset pentad. This emphasizes the importance of the criteria of preceding and subsequent pentads. Both methods are very sensitive on the definition of threshold, as discussed by Marengo et al. (2001). The OLR threshold value of 230 W m^{-2}, for example, would shift the onset for 2011 probably to some pentad in January of 2012.

Figure 3.7: The onset of the rainy season in WCB for the years (a) 2011 and (b) 2013. 5-day averaged time series of OLR (W m^{-2}) are presented by the red curve and precipitation (mm day^{-1}) by the green curve. The solid horizontal line refers to the thresholds defined for both methods and the vertical dashed line defines the onset pentads.
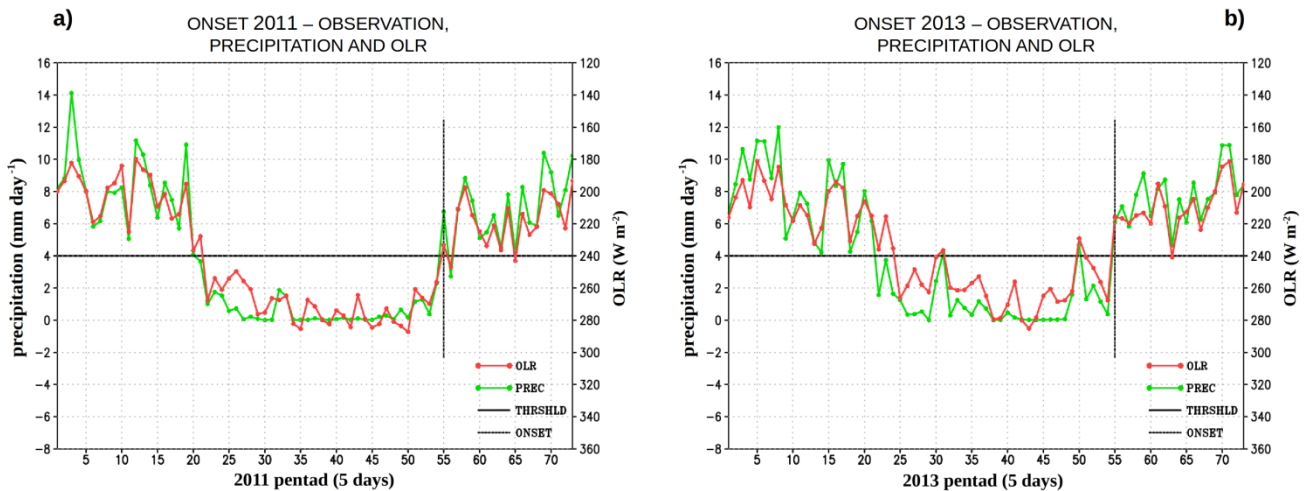
Figure 3.8 shows temporal evolution of 5-day averaged precipitation and OLR for each member of the ensemble referred to as GEF13 to GEF17, from now on, the ensemble mean and observation from pentad 49 until pentad 66, which covers the period 29 August-26 November, that is approximately the trimester SON. Coefficients r13-r17 are the Pearson correlation coefficients (temporal correlations) for each member of the ensemble and they are a measure of the linear correlation between 2 variables, in this case, between

simulated and observed precipitation and between simulated and reanalysis OLR. The coefficients vary between +1 and −1, where 1 is total positive linear correlation, 0 is no linear correlation, and −1 is total negative linear correlation. The numbers 13-17 as suffixes in the names of the members correspond to dates of initial conditions (13th-17th of August) of each member of the ensemble, while suffix "ens" corresponds to ensemble mean. The same methods as in Figure 3.5 cannot be applied. The first reason is because the period analyzed here (SON) is shorter than the 24 pentads necessary to apply the OLR method. The second reason is because of the missing information about precipitation before the pentad 49 and after the pentad 66, which could considerably change the onset date. Something similar would happen if the threshold of 230 W m^{-2} were applied to OLR in defining the 2011 onset, as mentioned in the analysis of Figure 3.7. The third reason is the definition of threshold for model simulations. For example, the threshold of 4 mm day^{-1} cannot be applied to the model because it underestimates precipitation in South America, as shown in Figure 3.5. However, it is possible to discuss and assess how the model reproduces the transition from dry to wet season analyzing each member and ensemble mean and comparing it against observed data.

Figure 3.8: 5-day averaged time series of precipitation (mm day^{-1}) of all members of the ensemble, ensemble mean and observation in WCB and temporal correlation coefficients for the period 29 August-26 November (pentads 49-66) of the years (a) 2011 and (b) 2013.
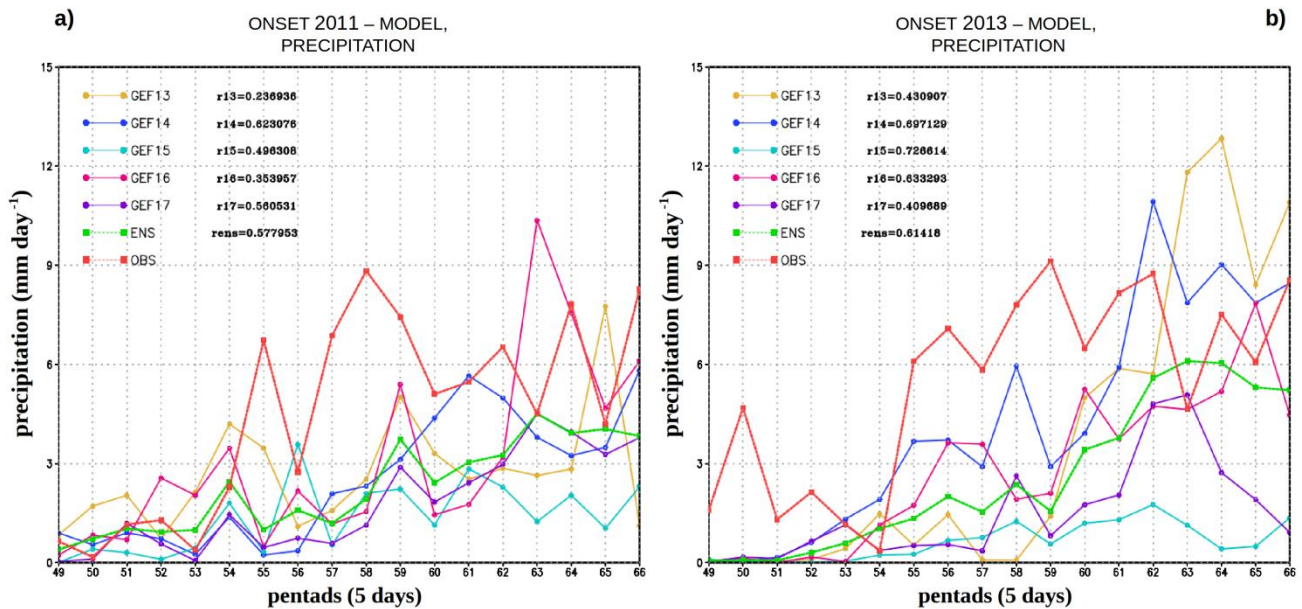
The observed precipitation data show 6 peaks in precipitation in pentads 52, 55, 58, 62, 64 and 66. The ensemble mean, on the other hand, shows clear peaks in pentads 51, 54, 56, 59, 63 and 65. Most of the members of ensemble simulate these peaks, but with different magnitude. Simple comparison of pentads with peak in precipitation indicates that model tends to lead the observed rain episodes, by about 1 pentad in most of the cases. However, the intensity of precipitation is not well simulated. In the first month of the analyzed period (September), before the observed onset in pentad 55, the intensity of precipitation seems reasonably reproduced. An abrupt change in precipitation pattern that represents the onset occurs between September and October. During the same period, the model shows slow increase, but with lower intensity of precipitation. That difference between simulation and observation decreases only in the last 4 pentads of the analyzed period, in November. The correlation coefficients varied between 0.24 and 0.62 among the ensemble members.

The first peak in observed precipitation in 2013 (Figure 3.8 b) in pentad 50 is almost nonexistent in the model, with barely visible sign of increase, while the second peak, in pentad 52, is more comparable in intensity but it is not clearly defined as a peak by the ensemble precipitation mean. In the period from pentad 51 until pentad 56, the ensemble mean shows constant, almost linear increase, while there are clearly present minima and maxima in the observed data. Simulated peaks in the pentads 56 and 58 correspond to the observed peaks in the pentads 56 and 59. The simulated precipitation, in pentads 59-61, shows the same pattern as the observed precipitation in pentads 60-62, which indicates that the model leads the onset, similarly as in 2011. However, in the last 5 pentads, although the model improves the simulation of the intensity of precipitation, it seems that the model loses the skill to represent the peaks in precipitation. Comparison of the correlation coefficients reveals that almost all members of the ensemble, including the ensemble mean, are better for 2011. The correlation coefficients varied between 0.41 and 0.73 among the ensemble members. Significant differences are present during the first month of analyzed period, where model has good skill in 2011, while it mostly fails to simulate some pre-onset maxima in precipitation in 2013. In addition, the members of ensemble in 2011 are more mutually comparable in intensity, especially during the first two months of integration, while the members in 2013 have more divergent nature, with bigger amplitude in intensity, that is particularly pronounced in the last month of integration.

Figure 3.9 shows daily mean precipitation over South America, simulated by each ensemble member and ensemble mean, compared against corresponding CMORPH observed precipitation. Numbers from 13 to 17 over the figures mark each member of ensemble depending on the date of initial conditions (13th-17th of August) for each year and black rectangle in the middle of the figure represents WCB region. All members show deficit in rain over the Amazon region in 2011. The members 13 and 15 have the lowest amount of precipitation in WCB region, while member 16 has the highest amount of

precipitation in WCB and generally in South America. Nevertheless, ensemble mean precipitation, even with clearly present deficit in rain, performs well in spatial distribution of precipitation and it is comparable with CMORPH observations. The first two members of ensemble for 2013, 13 and 14, have the best reproduction of intensity of precipitation when compared with all the integrations made for both years. At the same time, the members 15 and 17 are probably the worst, especially in WCB region. However, similar as in 2011, the ensemble mean precipitation has good spatial distribution, but with visible deficit in amount of precipitation.

Figure 3.9: SON daily mean precipitation (mm day^{-1}) over South America. The members of the ensemble for the year 2011 are in the top row (a) and for the year 2013 in the middle row (b). Comparison of the ensemble mean simulated and CMORPH observed precipitation (mm day^{-1}) for 2011 is in the bottom left row (c) and for 2103 in the bottom right row (d). The WCB region is identified by the black rectangle. The numbers 13-17 above figures are the dates of the initial conditions in August 2011 and 2013 for each ensemble member.
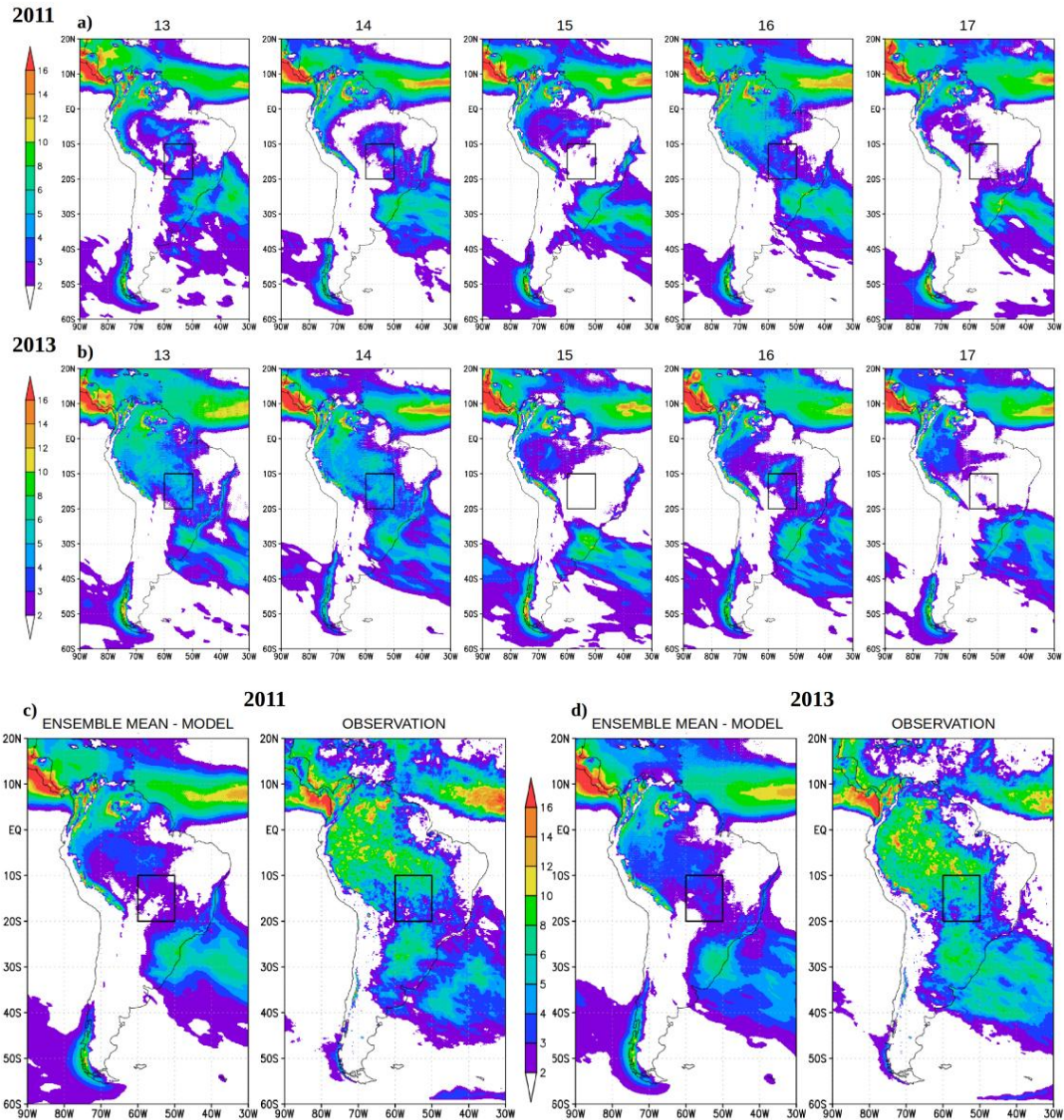
Figure 3.10 is the same as the Figure 3.8, only with inverted y-axis and showing OLR field. Maxima of the red dashed line represent the minima of OLR data from reanalysis, due to inverted y-axis and they correspond to maxima in precipitation. The model mean OLR follows well the tendency of decrease of observed OLR values, but without clear signs of minima of OLR during most of the analyzed period, only with weak minima and maxima in last 6 pentads, that are out of phase (Figure 3.10 a). Some other members of ensemble, GEF13, GEF14 and to some extent GEF15 show the same pattern in last 6 pentads, while GEF17, for example, reproduces very well the pattern of ORL before onset in pentad 55. The values of OLR are mostly overestimated by the model, especially at the beginning of integration, when the difference reaches almost 80 W m^{-2}. The error reduces with time, reaching the values around 40 W m^{-2} in the middle of integration. Similar values as in observation are shown in the last month of integration. As soon as the model starts to produce rain, that error in OLR decreases and starting from onset until the end of integration it shows good skill even with a good performance in simulating the minimum at the pentad 61. But it still overestimates the values of observed OLR maintaining relatively constant difference of about 40-50 W m^{-2}. If the model was able to reproduce the first two peaks in precipitation, the results of temporal correlation in OLR would be better. Correlations vary between 0.74 and 0.85.

Figure 3.10: 5-day averaged time series of OLR (W m^{-2}) of all members of ensemble, ensemble mean and observation in WCB and temporal correlation coefficients for the period 29 August-26 November (pentads 49-66) of the years (a) 2011 and (b) 2013.
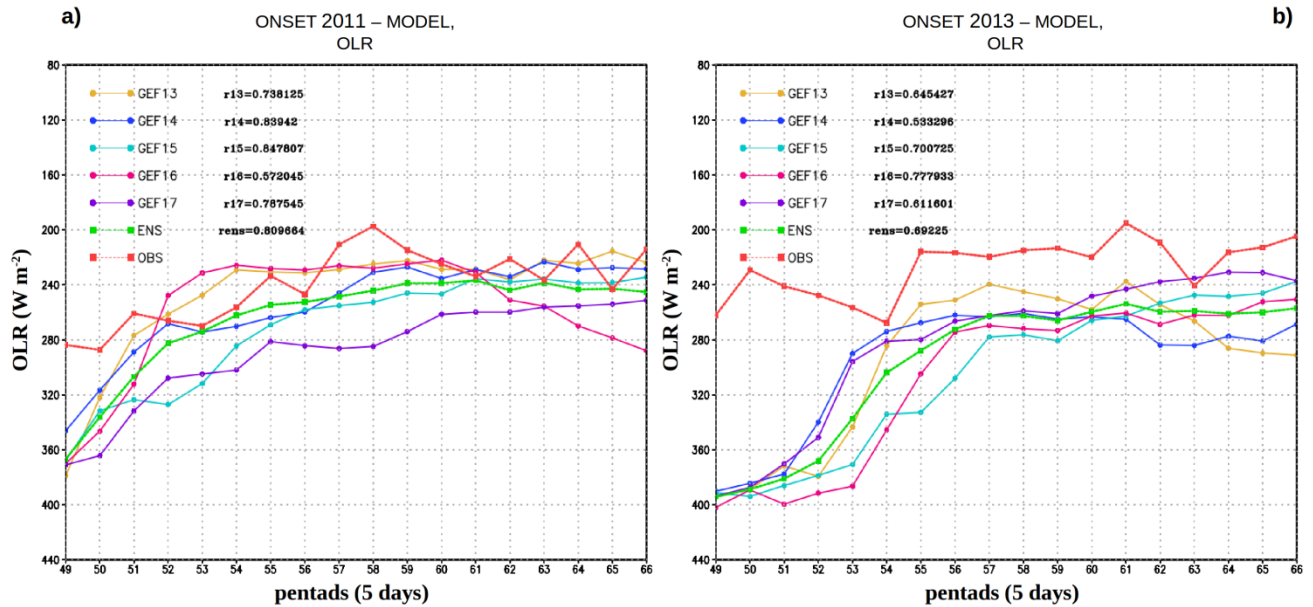
Observed precipitation and OLR are highly inversely correlated variables (Figure 3.11). Each maximum in precipitation (green line) corresponds to minimum in OLR (red line) and vice versa. Therefore, the temporal correlation between the two variables is highly negative such as -0.97 for 2011 (Figure 3.11 b) and -0.94 for 2013 (Figure 3. 11 d), for the same period as in Figure 3.8 and Figure 3.10. When ensemble mean precipitation and OLR simulated by the model are correlated, the values of coefficients are lower, but still relatively high: -0.69 for 2011 (Figure 3.11 a) and -0.76 for 2013 (Figure 3.11 c).

Figure 3.11: Comparison between simulated and observed 5-day averaged time series of precipitation (mm day^{-1}) (green curve) and OLR (W m^{-2}) (red curve) in WCB for the years 2011 (top row) and 2013 (bottom row). The temporal correlation between precipitation and OLR for the period 9 August-26 November (pentads 49-66) is plotted. The negative values show the inverse correlation between precipitation and OLR.
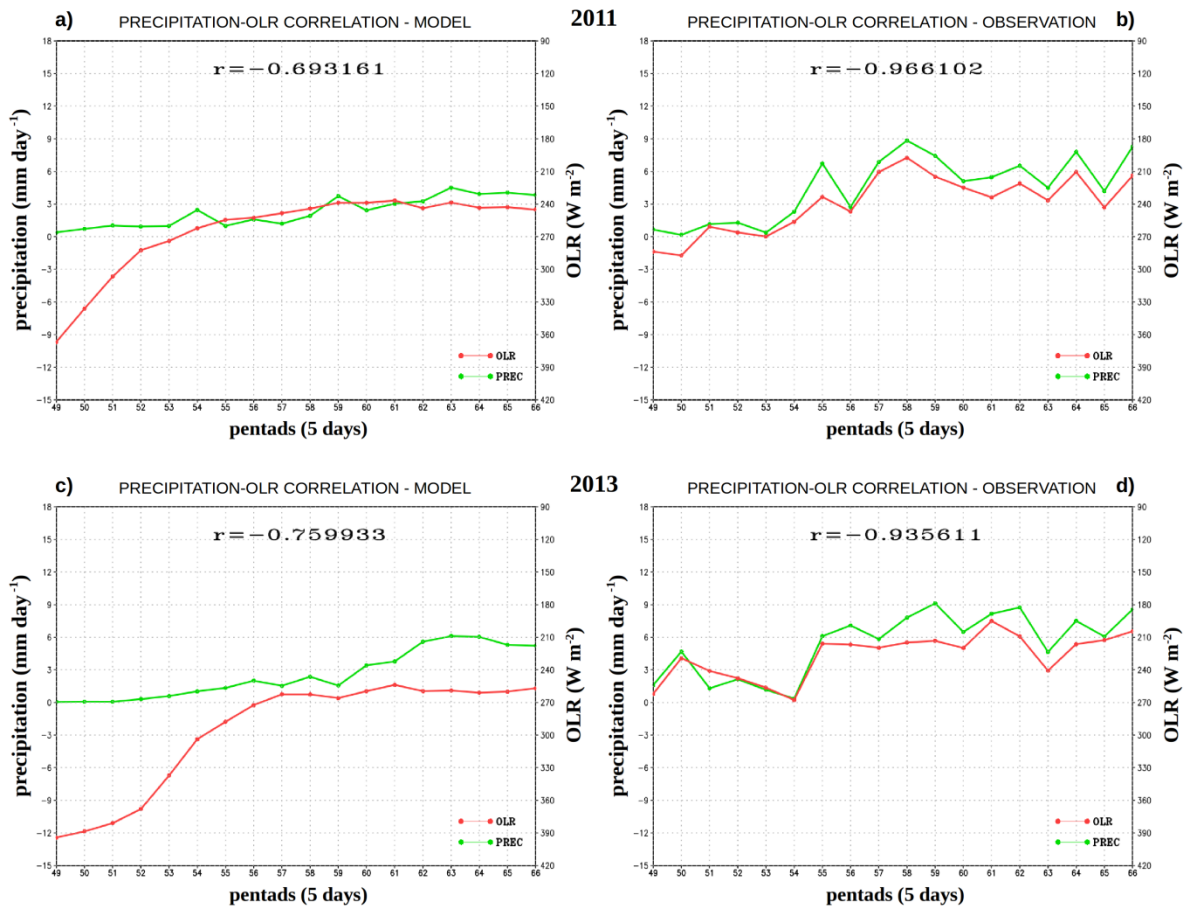
Time-longitude daily mean precipitation, averaged over 20°S-10°S for the period SON 2011 and 2013, is presented in Figure 3.12. The model simulates some pre-onset episodes of rain in WCB region in September, with the first intense continuous precipitation occurring in the period 23-28 September (approximately pentad 54), while in the observations the onset is identified in the period 26 September-2 October (approximately pentad 55). Lower charts show the ensemble mean simulated by the model for 2013 on the left and observed data on the right, and show relatively similar pattern as in 2011. The

difference is that model produces little rain in the first 20 days of September, simulating some weak rain only at the beginning of the last 10 days of September. More intense rain is simulated only in the eastern part of WCB region in the period 1-6 October (approximately pentad 56). Observed data show some rainy episodes in September with more intense continuous rain occurring in the period 28 September-2 October (approximately pentad 55). Precipitation is notably more intense in observations for both years.

Figure 3.12: Time-longitude daily precipitation (mm day^{-1}) averaged over 20°S–10°S for the period between 9 August-26 November (pentads 49-66) of 2011 (top row) and 2013 (bottom row). Simulated precipitation (mm day^{-1}) is on the left ((a) and (c)) and observed precipitation is on the right ((b) and (d)).
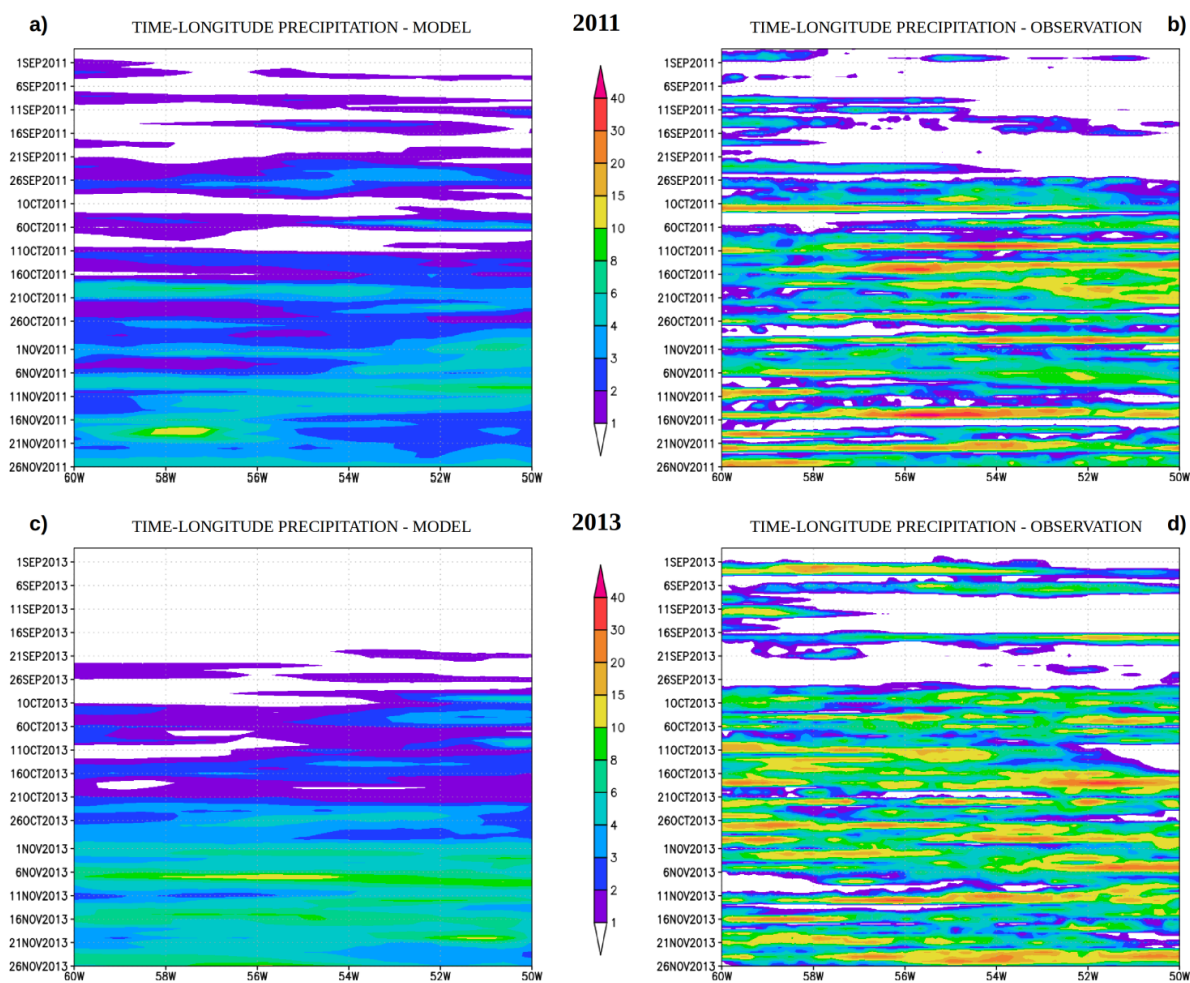
3.6 Diurnal cycle of precipitation

The ability of GEF to accurately simulate diurnal cycle of precipitation over South America is assessed using the approach similar as in da Rocha et al. (2009), where the values are averaged over the 10°×10° latitude by longitude squares, with the difference that the analysis presented here is extended more towards north, up to the latitude 5°N. Figure 3.13 shows the area of South America (35°S - 5°N, 75°W - 35°W) divided in 10°×10° squares where 5-member ensemble seasonal mean diurnal cycle simulated by GEF (blue bars) for the period SON 2011 is shown together with the corresponding CMORPH observed data (black solid lines).

Figure 3.13: 5-member ensemble mean of the total precipitation diurnal cycle for the period September to November (SON) 2011. The values are averaged over the 10° × 10° latitude by longitude square indicated in the background map. The blue bars represent 6-h accumulated precipitation simulated by the model and the solid black lines represent 30-min accumulated observed precipitation from CMORPH, both presented in the unit mm day^{-1}. The same scale (0-16 mm day^{-1}) is used for the y-axis in all plots.
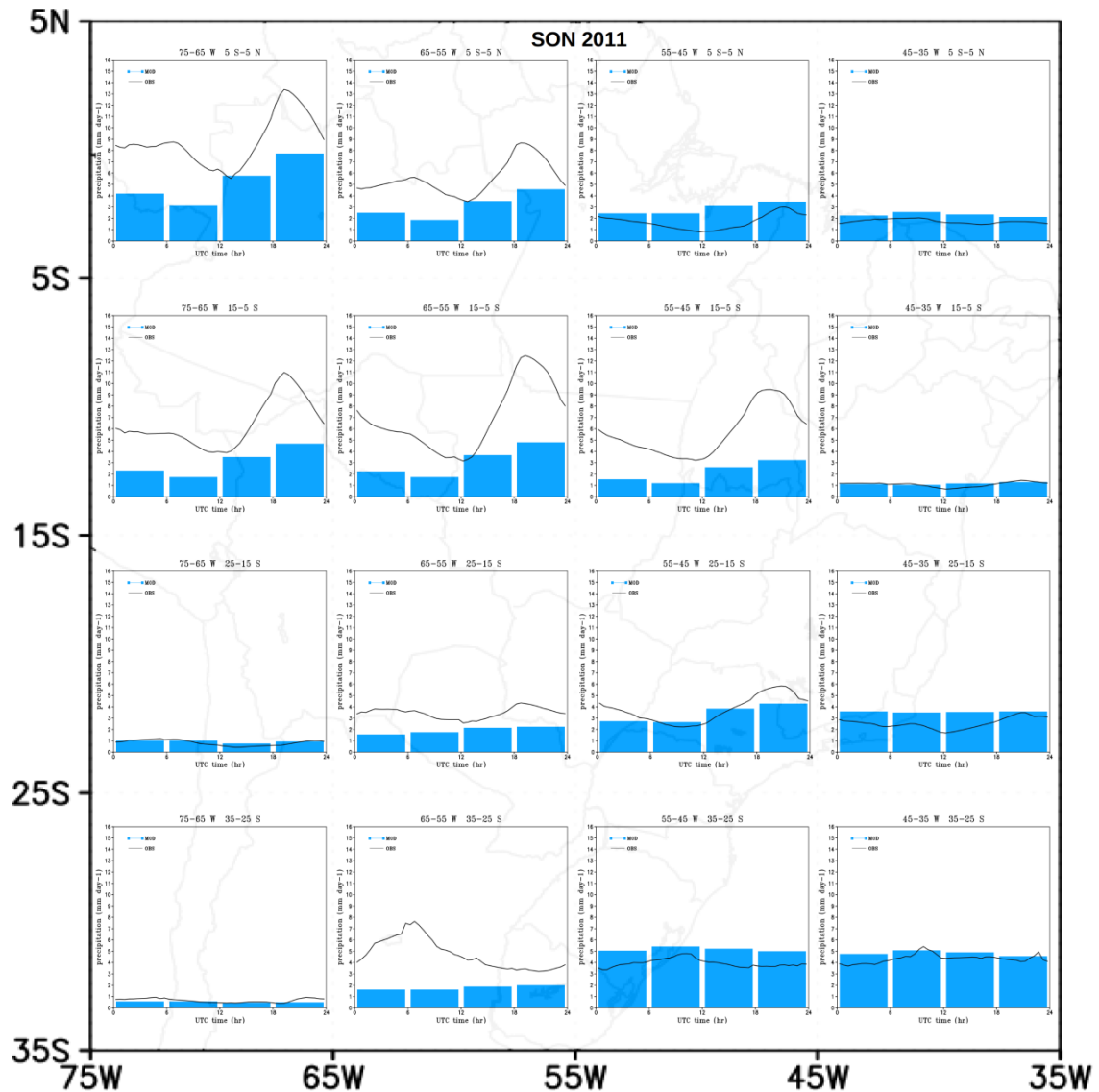
For the easier analysis, the subdomains are divided in 4 categories according to their latitude. The upper panel (5°S - 5°N) is called equatorial (EQ), and the panels below: tropical (TR, 15° - 5°S), subtropical (ST, 25° - 15°S) and

extratropical (ET, 35° - 25°S). The numbers from 1 to 4 are attributed to the each subdomain going from left to right, according to their longitude: 75° - 65°W is subdomain 1, 65° - 55°W is subdomain 2, 55° - 45°W is subdomain 3 and finally 45° - 35°W is subdomain 4. The subdomains EQ1, EQ2, TR1, TR2 and TR3 show the similar pattern in diurnal cycle of precipitation, with well defined daily peaks at 1900 UTC (1500–1600 local standard time (LST)) and less intense nocturnal peaks at 0700 UTC (0300-0400 LST). The daytime precipitation that dominates over the mentioned subdomains is probably associated with the boundary layer forcing, while the nocturnal peaks in subdomains EQ1 and TR1, closer to the Andes, are probably related with the convergence between the descendent mountain streamflow during the night (valley circulation) and the predominant north-easterly wind in the western Amazon basin (GARREAUD; WALLACE, 1997). The nocturnal peaks in the subdomains EQ2 and TR2 are likely associated with the synoptic systems that form at the mouth of the Amazon River during the afternoon hours and propagate inland with a velocity of approximately 15 m s^{-1} (KOUSKY, 1980; COHEN et al., 1995). With this propagation velocity, the precipitation maxima occur during the night hours, around 500–700 km inland, which is the distance covered by these subdomains. The subdomain TR3 is probably influenced by these systems, but without clear nocturnal peak in the observed data. In all analyzed cases, the model simulated well the presence of the daily and nocturnal precipitation maxima, despite having the underestimated intensity. The same systems are responsible for the daily peak observed in subdomain EQ3, when with the daytime heating, precipitation rapidly develops along and just inland from the coast, probably related to the sea breeze. In this situation, the model simulates well the daily peak in precipitation, but not the minimum in the morning hours and generally, overestimates the rainfall. Weak nocturnal peak observed in EQ4 is probably due to the area covered mostly by the ocean and it is also present in the model simulation, with slightly overestimated values. TR4 shows weak maximum in daily precipitation, that is captured by the model, while the precipitation during the night hours with approximately the same

52

intensity might be attributed to the partial presence of the ocean covered by this subdomain. The subdomains ST1 and ET1 are the areas with weak precipitation whose distribution is almost uniform, both in the observation and in the model simulation. However, weak maxima and minima exist, and they might be attributed to the highly heterogeneous terrain that these subdomains cover. The cloudiness that increases rapidly between 1500 and 2000 UTC in the Andean Altiplano, reaching a maximum after 1800 UTC (GARREAUD; WALLACE, 1997), probably causes the weak daily peak in precipitation, while the night-time peak (0600–1200 UTC) is normally associated with the mesoscale convective complexes (MCCs) activity over the central and northern part of Argentina, on the eastern border of these subdomains (VELASCO; FRITSCH, 1987; NICOLINI; SAULO, 2006; SALIO et al., 2007). The area where MCCs predominantly define the nocturnal peak is mostly covered by subdomain ET2 and partially by ST2. Particularly pronounced nocturnal peak (0600 UTC) is seen in ET2, however, it is not captured by the model, together with the lower nocturnal peak in ST2. The afternoon maximum (1900 UTC) in ST2 area is mainly of moist convection origin and it is present in the model simulation, with underestimated values. In the ST3, both the model and observation show one precipitation maximum at 2100 UTC. The daytime peak is probably the result of the strong solar heating at the surface that produces large sensible and latent heat fluxes from the surface to lower troposphere, making the atmosphere more favorable for convection. The sea-breeze circulation associated with the steep coastline in the region contributes to the rainfall intensification during the day (DA ROCHA et al., 2009). ST4 subdomain that covers subtropical east coast of Brazil shows two peaks, where the nocturnal rain is probably produced in its oceanic part. The precipitation in the model is mostly uniformly distributed and overestimated, with very weak signals of these peaks. ET3 subdomain receives more rain in SON season, due to the initial phase of SAMS. Increased precipitation is captured and even slightly overestimated by the model and it is distributed relatively uniformly during the day, with one peak observed at 1100 UTC which might be associated partially to the MCCs and partially to the

thermodynamic heating, topographical influence and presence of the ocean in the covered area. ET4 is the subdomain completely over the ocean, with the peak in precipitation observed at the same time as in ET3, which is captured by the model, and one more at 2300 UTC, which is not. Similar analysis is valid for the case of SON 2013 (Figure 3.14), where the precipitation peaks, both observed and simulated, in most of the cases only slightly differ in intensity.

Figure 3.14: 5-member ensemble mean of the total precipitation diurnal cycle for the period September to November (SON) 2013. The values are averaged over the 10° × 10° latitude by longitude square indicated in the background map. The blue bars represent 6-h accumulated precipitation simulated by the model and the solid black lines represent 30-min accumulated observed precipitation from CMORPH, both presented in the unit mm day^{-1}. The same scale (0-16 mm day^{-1}) is used for the y-axis in all plots.
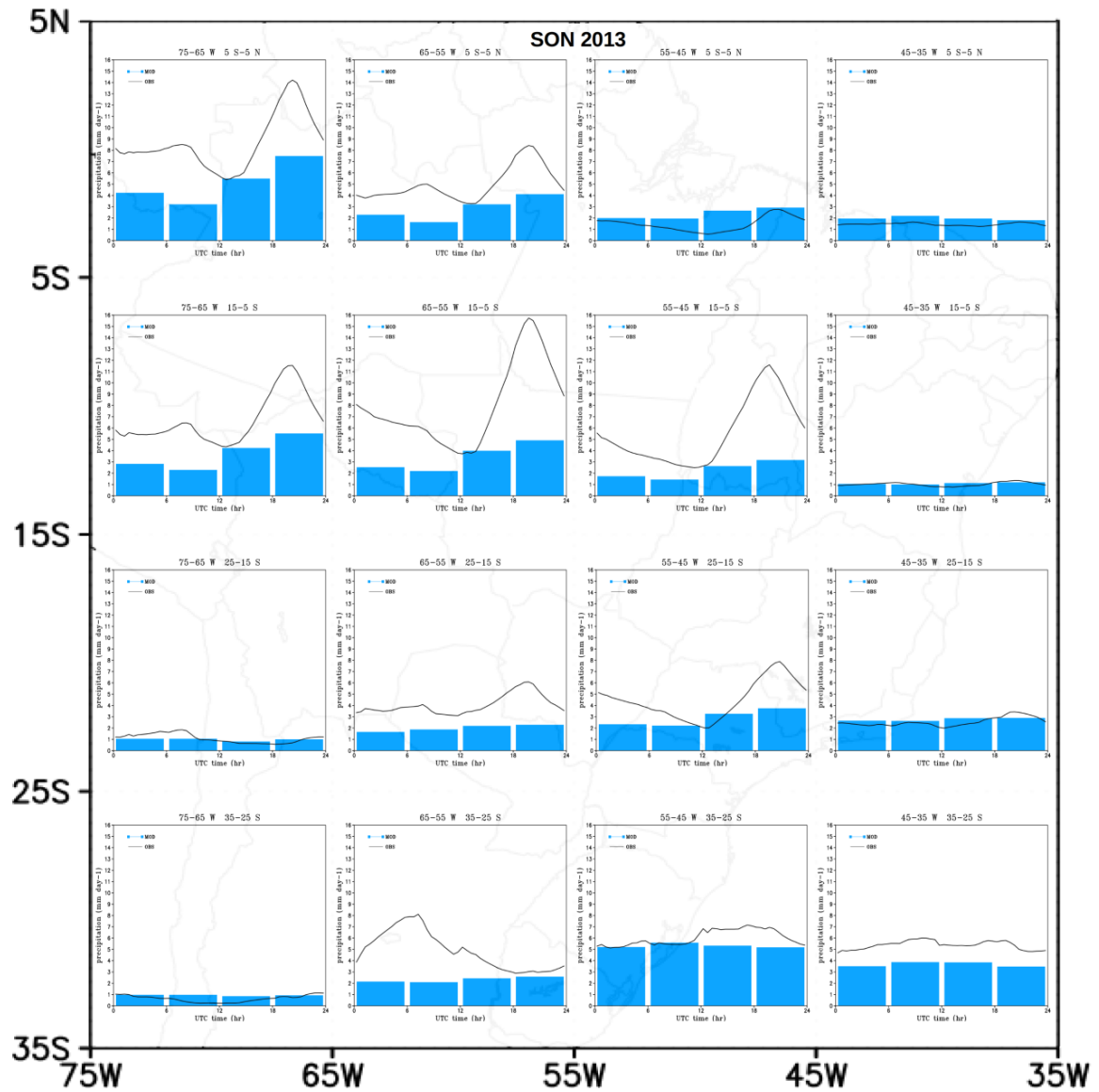
3.7 Chapter conclusions

The main objective of this study was to assess prediction skill of GEF and to evaluate capability of the model to simulate the onset of the rainy season in the WCB region in an ensemble seasonal forecast for the years 2011 and 2013. To this end, it was performed a comparative analysis of predicted and observed (or from reanalysis) global mean fields for the period SON of both years, in the first part of this work. Some preliminary results with this version of the model are shown in Latinović et al. (2017), where it is confirmed the ability of GEF to perform simulations with increased horizontal resolution and upgraded version of cubed-sphere and its stability in long-term seasonal integrations. The results presented in the section 3.4 of this study demonstrate the high level of spatial correlation between the model and reanalysis for almost all analyzed variables, with coefficients of 5 out of 6 variables varying from 0.85 to 0.99. Intensity of almost all variables is also well represented by the model, mostly with some local differences. Variables from different levels are evaluated, starting from upper-troposphere with 200-hPa wind, over mid-troposphere, represented by 500-hPa geopotential height and lower-troposphere represented by 850-hPa temperature and wind, down to MSLP at the surface. They represent the dynamical part of the model and demonstrate good skill for both years in seasonal integration for the period SON. The lowest skill comes from precipitation, as a variable that represents the "physics" of the model. On the other hand, it reproduces reasonably well the spatial distribution of precipitation, with the value of 0.64 for coefficient of spatial correlation, in both years. Simulated intensity shows the pattern where precipitation over some tropical oceanic regions is mostly overestimated and over tropical continental regions is mostly underestimated. The other part of this chapter contains analysis of onset of the rainy season in WCB region based on the methods that employ precipitation and OLR. The onset defined from observations using both methods occurs in the pentad 55 in both years. The model shows underestimate in precipitation and overestimate in OLR field, therefore, the

same thresholds could not be applied in the model outputs of these variables. Limitation is also present in the length of analyzed period where criteria of preceding and subsequent pentads, present in both methods could not be applied correctly. Still, comparative assessment of temporal evolution of 5-day averaged predicted and observed precipitation through the period SON demonstrates that the model ensemble mean possesses good skill in predicting maxima of precipitation even close to the end of observed period, with errors of around 1 pentad when compared with observed data. With regard to intensity, simulated precipitation rather shows continuous increase along the observed period than an abrupt change in regime during transition period from dry to wet season, with almost comparable intensity of precipitation in the first and in the last month of SON. Some members, however, show some signs of sudden change in precipitation intensity close to the pentad of observed onset, but with underestimated values. Temporal evolution is quantified through the linear correlation coefficients with the reasonably high values of 0.58 and 0.61 for the years 2011 and 2013, respectively. In comparison with precipitation, all the members of ensemble in the analysis of temporal evolution of OLR generally show higher values of linear correlation coefficients, with ensemble mean value of 0.81 for 2011 and a slightly lower value of 0.69 for 2013. The extreme values in OLR are to some extent simulated by some members of ensemble, but they mostly disagree in the position of these minima or maxima in time, thus the ensemble mean line looks smooth, with no clear signals of extreme values. On the other hand, it represents well the tendency and, except of the first analyzed month of 2013, it shows similar pattern as the observed OLR. Overestimate that also characterizes the model in simulation of OLR, is more visible in 2013. Temporal correlation of ensemble mean precipitation and ensemble mean OLR shows fairly good level of agreement, although with moderately lower values of coefficients than in observation.

The ability of the model to simulate the onset of the rainy season in WCB is best demonstrated in the Figure 3.12, which shows the time-longitude daily averaged precipitation over the latitudes 20°S-10°S. It is clearly shown that with

the difference of couple of days (earlier in 2011, and later in 2013) when compared against observed data, the model shows transition of precipitation regime from dry to wet, approximately at the end of September, beginning of October. Precipitation pattern changes and more intense precipitation starts to occur after that date, although still significantly less intense than observed.

The diurnal cycle of precipitation is mostly well represented by the model in the ensemble simulations. The exception is the region of central and northern Argentina and Paraguay where the nocturnal peaks attributed to MCCs that are more frequent during the summer and spring (VELASCO; FRITSCH, 1987; SALIO et al., 2007) and form downstream of the South American Low Level Jet (SALLJ) are not simulated well by the model, probably due to the simulated shift of SALLJ toward southeast.

The underestimate of precipitation rate over tropical continental regions, particularly over South America, remains one of the main issues of the model and further improvements and adjustments are necessary in convection scheme for precipitation production. The recently implemented and tested radiation scheme, RRTMG (Rapid Radiative Transfer Model for GCM), produced downward surface shortwave radiation fluxes closer to observations and reduced the systematic positive bias found in the regional Eta model (DE ANDRADE CAMPOS et al., 2017). It demonstrated better performance in most of evaluated variables, especially in clear-sky conditions. Once implemented in GEF, it could potentially bring benefits in the representation of radiation and precipitation as well. Already proven computational efficiency of GEF (ZHANG; RANČIĆ, 2007) and the results presented in this study confirm that continuous efforts in development of the model can give significant contribution in improvement to the seasonal forecasts at CPTEC.

4 MEDIUM RANGE INTEGRATIONS

4.1 Literature review

Extremes of precipitation are not well represented by global models. The extreme events such as floods, droughts, or storms have societal and economical impacts, since they may cause significant damage to agriculture, infrastructure and threaten human lives. Extreme rainfall events can be defined as significant deviations from the rainfall average. Extreme events of short duration are considered some of the most impacting (MARENGO, 2009). These events in the form of large amounts of rainfall in a short period of time are very frequent in Manaus, AM. Over the past 10 years, the Amazon basin has experienced frequent floods (ESPINOZA et al., 2012; MARENGO et al., 2012; SATYAMURTY et al., 2012) that directly impact the lives of its people. It is known that SST anomalies over the adjacent tropical oceans are the primary forcing for extreme events in the Amazon (CHEN et al., 2011; DAVIDSON et al. 2012; DOI et al., 2012; LIEBMANN; MARENGO, 2001; MOURA; SHUKLA, 1981; BOMBARDI; CARVALHO, 2011), through their impacts on atmospheric circulation patterns and moisture transport (WANG; FU, 2002; FU et al., 1999). Surface soil moisture and vegetation feedbacks, as well as land, regulate rainfall variability (NEPSTAD et al., 1999; MALHI; WRIGHT, 2004; FU; LI, 2004; CHEN et al., 2011; LEE et al., 2011; TOOMEY et al., 2011). Current global climate models mostly have deficiencies in capturing the intensity of extreme precipitation events (KHARIN et al., 2007; STEPHENS et al., 2010; SILLMANN et al., 2013). It has been suggested that physical processes governing extreme precipitation in these models are not well represented, especially subgrid processes and convective parameterization (SHIU et al., 2012; WILCOX; DONNER, 2007). The horizontal grid resolution of the models is also considered as an important factor in simulating extreme precipitation (POPE; STRATTON, 2002; ROECKNER et al., 2006; SALATHÉ et al., 2008; SHAFFREY et al., 2009). Nowadays, high-resolution models can explicitly

resolve convection, and there have been efforts by nearly every modelling group to run their models at the highest possible resolution affordable with the available computing power. However, increasing grid resolution often requires an adjustment of parameterizations to show improvement in model performance. These adjustments of model parameters are usually made in order to reduce biases. It is necessary because model parameterizations are typically resolution dependent (DUFFY et al., 2003). Also, changes which bring improvements in some output fields cause deterioration in others (POPE; STRATTON, 2002).

In this study, newly developed and configured high-resolution, 8-km, hydrostatic version of the Global Eta Framework (GEF) is integrated for the period of 10 days with 22 different sets of initial conditions. The model skill to simulate various atmospheric fields is assessed in a comparative analysis of simulated fields against reanalyses and observations, and by using some continuous and categorical statistical scores. The objective of this chapter is to evaluate the model simulations of the events at higher spatial scales and at medium range. In the next section, we describe the model configuration, the medium-range simulation setup, the methods and the data sets used in this study. Section 4.3 presents the large-scale circulation features of the runs and section 4.4 focuses on South America and provides some statistical analysis. In section 4.5 we analyze the model skill in simulation of 8 events of extreme precipitation over the city of Manaus, AM. We summarize and draw some conclusions of this chapter in section 4.6.

4.2 Medium-range runs and data

Model description is again provided in this section for completeness of the description of the medium-range runs. The Global Eta Framework (GEF) is a global atmospheric model, based on general curvilinear coordinates, developed by Zhang and Rančić (2007) and uses cubed-sphere grid topology, originated by Sadourny (1972). The version of the model used in this study has the latest version of the grid that provides an "equal-area" cubed-sphere,

without angular discontinuities across the edges of the cube (PURSER; RANČIĆ, 2011; PURSER et al., 2014; RANČIĆ et al., 2017). GEF represents a combination of the technique of quasi-uniform gridding of the sphere and the numerical structure of the regional Eta model (MESINGER et al., 1988; JANJIC, 1990; JANJIC, 1994; BLACK, 1994; CHOU et al 2002, 2012; MESINGER et al., 2002; PESQUERO et al., 2010; MESINGER et al., 2012; LYRA et al., 2017; MESINGER; VELJOVIC, 2017). Six regional models, interconnected through the cubed-sphere framework are integrated simultaneously, one on each side of the cube, to provide a global coverage and to create GEF – a "globalized" version of the regional Eta model.

The regional Eta model is named by the eta vertical coordinate (MESINGER, 1984) which is convenient to be used for weather forecasts in South America where weather conditions are strongly affected by high and steep Andes mountain range. It has quasi-horizontal coordinate surfaces that reduce pressure-gradient force errors due to steep topography, a typical error that appears in terrain-following coordinates. Even if the current version of GEF still does not employ "sloping steps" (MESINGER et al., 2012), the latest update of the vertical eta coordinate, it seems suitable for the use in simulation of weather conditions in South America.

The physics package of the code includes a choice of two convection schemes, Betts-Miller-Janjic (BETTS; MILLER, 1986; JANJIC, 1994), and Kain-Fritsch (KAIN, 2004) and two cloud microphysics schemes, Zhao (ZHAO et al., 1997) and Ferrier (FERRIER et al., 2002), where the latter of both are used in the configuration of the model in this study. The radiation package is developed by GFDL (Geophysical Fluid Dynamics Laboratory), with short-wave radiation scheme of Lacis and Hansen (1974) and long-wave radiation scheme of Schwarzkopf and Fels (1991), with radiation tendencies calculated every hour and applied at every time step. The land–surface transfer processes are parameterized by the Noah scheme (EK et al., 2003). Monin–Obukhov similarity theory is combined with Paulson stability functions (PAULSON, 1970) and applied at the surface layer to describe the logarithmic wind profile and coupled

to molecular sublayer over land and ice according to Zilitinkevich (1995), and over water according to Janjic (1994). Turbulence transports above the surface layer use the Mellor-Yamada 2.5 closure (MELLOR; YAMADA, 1982; JANJIC, 1990).

The model was set up at 8-km horizontal resolution and 38 vertical levels, with the model top at 25 hPa. Initial conditions are taken from NCEP reanalyses at 0000 UTC for each of 22 cases. The model is forced by observed SST (REYNOLDS et al., 2002) and it is updated daily by interpolating from the observed monthly mean global SST, similarly as vegetation fraction, which is also updated daily but from monthly mean climatological values. The model integration is 10 days using 10-second time steps. Analysis of the output data is made by comparison against NCEP reanalyses data and CMORPH precipitation data (JOYCE et al., 2004). 10-days integrations are run with the objective to assess the model ability to simulate 8 cases of heavy precipitation observed in Manaus, AM, with the lead times of 24, 48 and 72 hours.

Table 4.1 lists the corresponding dates of these events, where two analyzed events occurred in two consecutive days, on 20 and 21 April 2013. Due to the partial overlapping, the total number of the integrations is 22 instead of 24 (8 cases, 3 integrations of the model for each, with different lead time). In the analysis of large-scale circulation patterns, globally and for South America, a case study approach was used, where one selected integration of the model is analyzed. For calculation of the statistical scores, an ensemble of the 22 integrations is used. In the last section, 8 selected cases of extreme precipitation are described and their precipitation fields are compared against the corresponding observations.

Table 4.1: The dates of 8 extreme precipitation events observed in Manaus, AM

1	31 October 2012	5	30 September 2013
2	8 November 2012	6	19 November 2013
3	20 April 2013	7	9 September 2016
4	21 April 2013	8	17 November 2016

The statistics scores used in this study to evaluate the accuracy of continuous variables are the Root Mean Square Error (RMSE) and the Pearson correlation coefficient (R). The RMSE is a frequently used measure of the differences between values predicted by a model and observed values. It is the square root of the average of squared errors and represents the sample standard deviation of the differences between predicted and observed values. It penalizes large errors. Pearson correlation coefficient is a measure of the linear correlation between two variables, in our case, predicted and observed, and represents a ratio of covariance to the product of the two standard deviations. It varies between +1 and −1, where 1 is total positive linear correlation, 0 is no linear correlation, and −1 is total negative linear correlation. Both scores are used in Section 4, RMSE for the wind intensity at 200 hPa and 850 hPa, geopotential height at 500 hPa, temperature at 850 hPa and MSLP for South America. Pearson correlation coefficient is calculated from the time series of predicted and observed 10-day daily mean precipitation for different regions of Brazil.

The categorical statistical scores used for model verification are based on the Equitable Threat Score (ETS) and the Bias Score (BIAS). The ETS is defined as (e.g., MESINGER; BLACK, 1992):

$$ETS = (H - CH) / (F + O - H - CH),$$

where,

CH = (F x O) / N.

CH is the number of points of random hits, and N is the number of points in the verification domain. The BIAS is defined as the ratio between the number of points of predicted precipitation above a threshold and the number of points of observed precipitation above the threshold:

BIAS = F / O.

When predicted precipitation rate is higher (lower) than the observed, this score is above (below) 1. A perfect forecast result is for ETS = 1 and BIAS = 1. The amounts of precipitation were divided into 8 categories: 0.25, 2.54, 6.35, 12.7, 19.05, 25.4, 38.1, and 50.8 mm where the threshold values correspond to rounded numbers and are easier to understand when presented in inches. In this work, the model performance was evaluated according to the ability of the model to forecast precipitation amounts above the certain thresholds. The precipitation amounts used are the total precipitation accumulated in 24 hours at 1200 UTC. The ETS and BIAS are calculated for the forecast time ranges of 36 and 60 hours in Section 4, for the region of South America. Observed data used are from CMORPH and calculations are made in every grid box.

4.3 Large-scale features

Comparative assessment of simulated global atmospheric fields against appropriate reanalyses is presented in this section. The analyzed variables are: wind at 200 hPa and 850 hPa, geopotential height at 500 hPa, temperature at 850 hPa and MSLP. For this purpose, case study approach is applied, using only one selected integration of the model, with initial conditions from 0000 UTC 18 April 2013. Each figure shows the simulated field, the corresponding reanalysis field and the errors for the integration days 1 (Figure 4.1 a), 3 (Figure

4.1 b), 5 (Figure 4.1 c), 7 (Figure 4.1 d) and 10 (Figure 4.1 e). Figure 4.1 shows wind at 200 mb, with shaded magnitude and wind direction shown with streamlines. Day 1 shows the highest level of agreement with reanalysis, both in terms of intensity and direction, as expected. The most notable difference is in the jet streams in the southern hemisphere that are more intense in the model simulation. Days 3 and 5, simulations differ more from reanalysis, but they are still with reasonable agreement. Positions of the wind maxima start to be more displaced in model simulation, which becomes more visible on day 5, especially over Southern Pacific, Australia, and Bering Sea. On day 7, wind direction and wind maxima over northern hemisphere are still relatively comparable with reanalysis, with exception over the area of the Bering Sea, while in the southern hemisphere the differences become more visible. On day 10, the errors of wind intensity of the jet streams simulated by the model on both hemispheres clearly grow.

Figure 4.1: 200-hPa wind speed (color shaded, m s^{-1}) and direction (streamlines). The plots from left to right represent the model simulation, the corresponding NCEP reanalysis and the difference between the model and the reanalysis, respectively, after: (a) 24 h, (b) 72 h, (c) 120 h, (d) 168 h and (e) 240 h of integration of the model. The initial condition used was from 0000 UTC 18 April 2013.
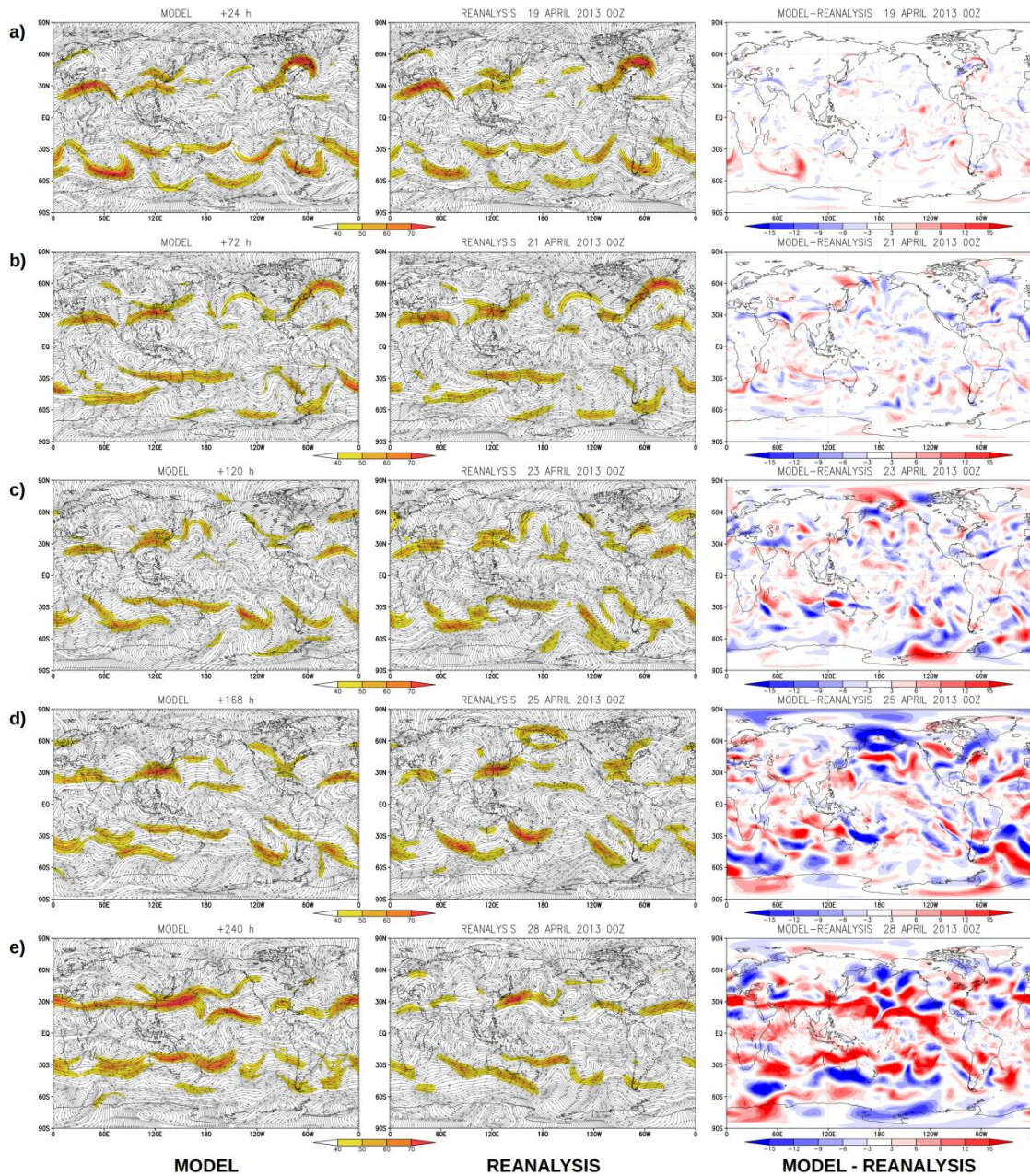
Wind field at 850 hPa simulated by the model shows high level of agreement with reanalysis on forecast day 1 and day 3 (Figure 4.2), with minor differences in position of the wind maxima and minima. Predominant easterlies are present in the equatorial region and westerlies with wave-like undulations upon the basic flow in the mid-latitudes, with mostly correctly simulated positions of the systems with cyclonic and anticyclonic flow. On day 5, most of these systems are captured by the model, with notable differences in position and intensity in southern Atlantic and Pacific, which is shown by patterns of shades of red next to the shades of blue, with the darkest shades representing the differences of more than 15 m s^{-1}. Similar to Figure 4.1, on day 7, the simulation errors become more visible and solutions provided by the model start to diverge when compared with reanalysis. Although some synoptic scale systems can be recognized in the model simulation, they differ from reanalysis more than on the day 5. The circulation pattern from the day 10 has more north and south meanders in the wave-like pattern in the southern hemisphere mid-latitudes, more intense easterlies over the equatorial region and generally low level of similarity with reanalysis.

Figure 4.2: 850-hPa wind speed (color shaded, m s^{-1}) and direction (streamlines). The plots from left to right represent the model simulation, the corresponding NCEP reanalysis and the difference between the model and the reanalysis, respectively, after: (a) 24 h, (b) 72 h, (c) 120 h, (d) 168 h and (e) 240 h of integration of the model. The initial condition used was from 0000 UTC 18 April 2013.
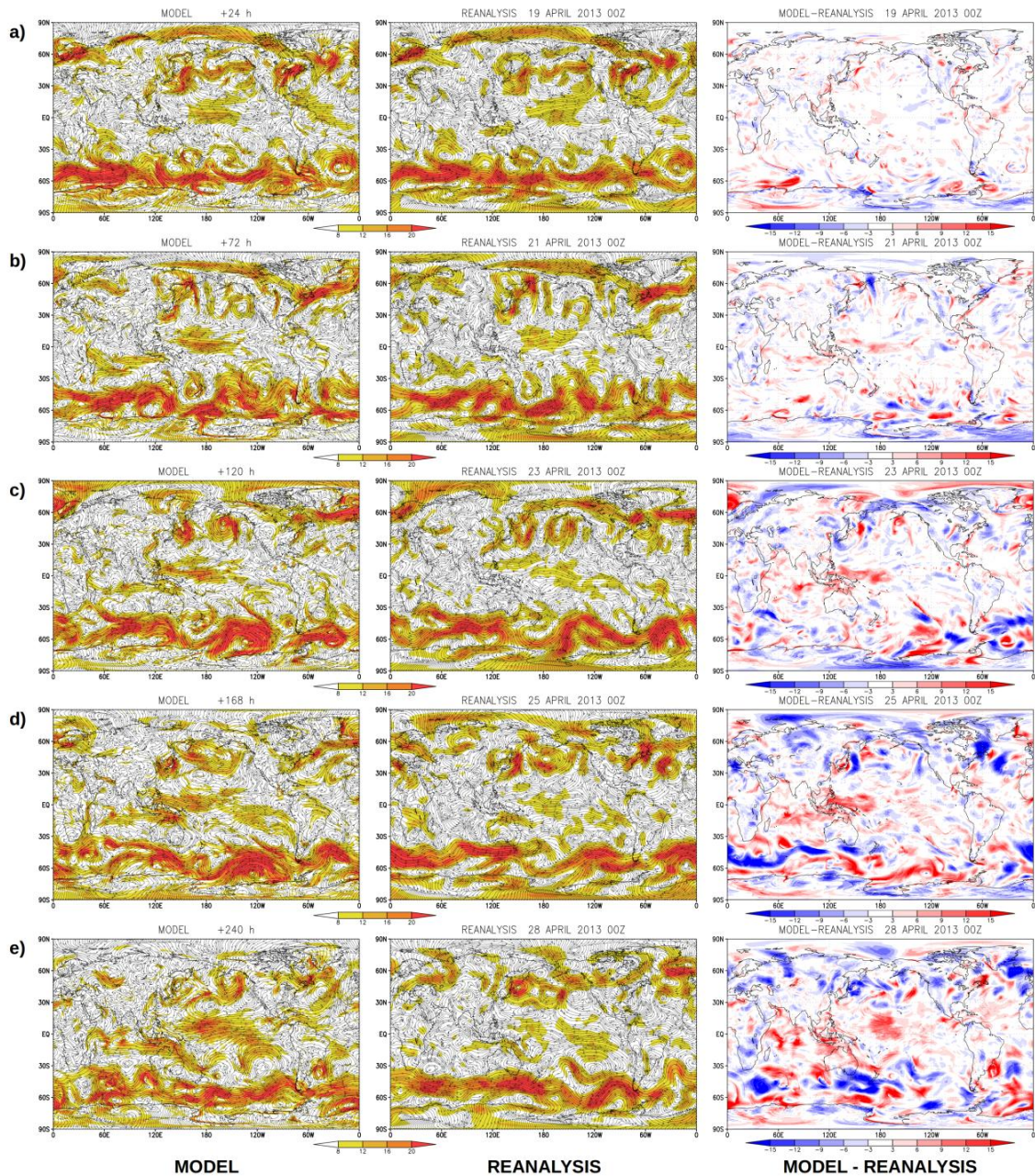
Pressure-latitude cross section of zonally averaged wind speed (Figure 4.3) shows the position and intensity. Positions of the upper level jet streams are well simulated by the model for the days 1 and 3, with slightly overestimated values of the wind maxima which exceed 25 m s^{-1}. On day 5 (120 h) of the simulation, the values of the wind maxima are comparable with reanalysis, mostly within the range between 60 and 70 m s^{-1}, but the model displaces the wind maxima slightly equatorward in both hemispheres. Except for the southern hemisphere subpolar jet, the simulated winds are stronger than in reanalysis on the day 7, while positions of the wind maxima are still comparable with reanalysis. On day 10, the northern hemisphere winds are overestimated by the model by more than 30 m s^{-1}, although still relatively well positioned; however, in the southern hemisphere zonal mean winds become differ significantly from reanalysis, both in position and intensity.

Figure 4.3: Pressure-latitude cross section of the zonally averaged wind speed (color shaded, m s^{-1}). The upper plots represent the model simulation and the lower plots the corresponding NCEP reanalysis after: (a) 24 h, (b) 72 h, (c) 120 h, (d) 168 h and (e) 240 h of integration of the model. The initial condition used was from 0000 UTC 18 April 2013.
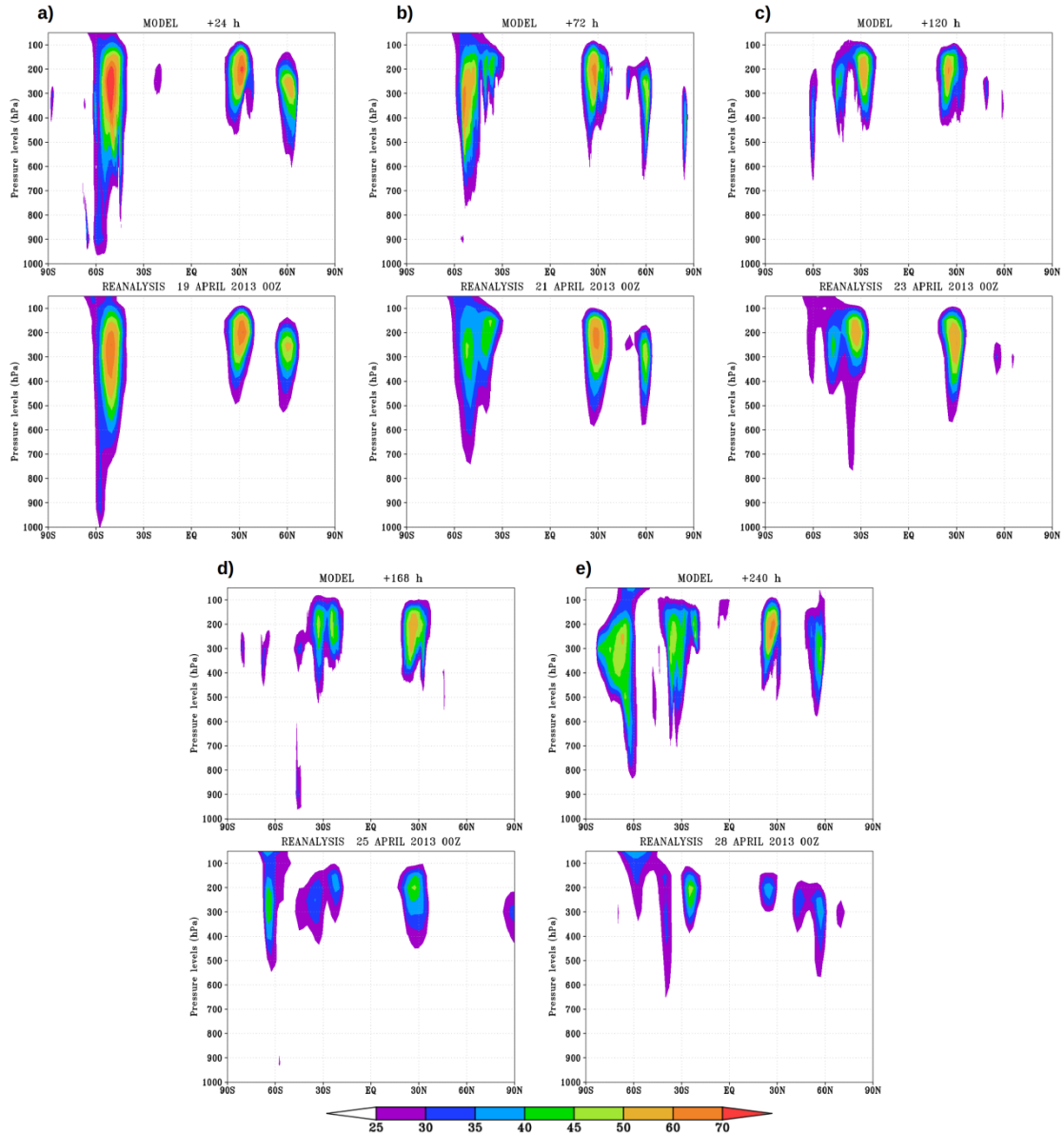
Geopotential height at 500 hPa shows clear disagreement with reanalysis on day 5 day (Figure 4.4). Model simulates most of the observed troughs and ridges but their positions start do differ more. This is clear on day 7 and on the day 10, the last day of integration. Some similarity between

reanalysis and simulations can be found on day 10 day; however, the model displaces the waves a few kilometres away from their observed position.

Figure 4.4: 500-hPa geopotential (colored contours, gpm). The plots from left to right represent the model simulation, the corresponding NCEP reanalysis and the difference between the model and the reanalysis, respectively, after: (a) 24 h, (b) 72 h, (c) 120 h, (d) 168 h and (e) 240 h of integration of the model. The initial condition used was from 0000 UTC 18 April 2013.
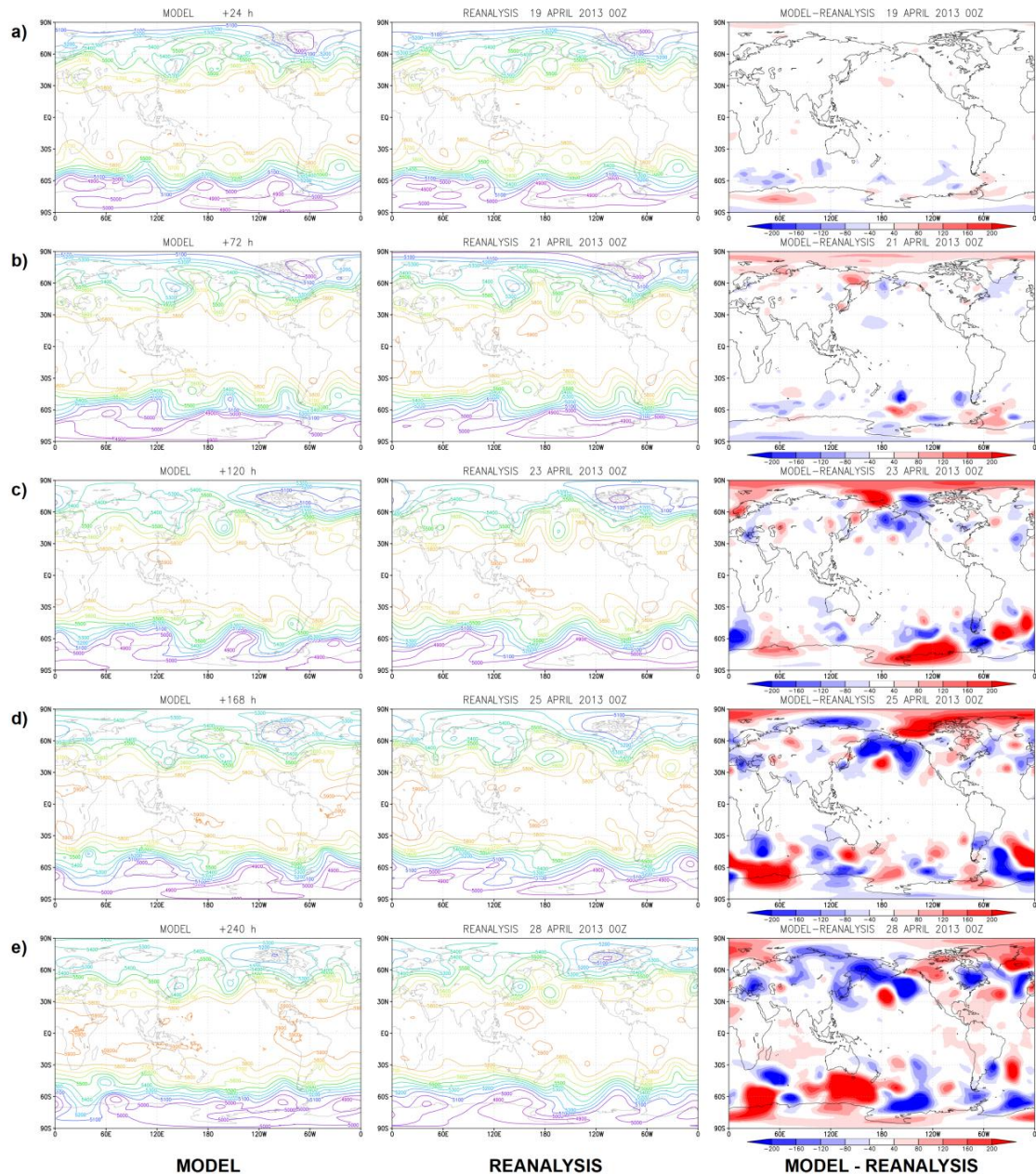
The warm bias in 850-hPa temperature over Antarctica and Greenland is present during all integration period (Figure 4.5). This error may be due to inappropriate initial conditions for snow depth data for these regions. The cold biases prevail in the mid-latitudes, while the warm biases are mostly present in the polar, subtropical and equatorial regions. These biases in temperature become more intense as the time of integration increases, exceeding 15 degrees Celsius, over the Antarctica after 10 days of integration. In the mid-latitudes, these larger errors that appear on the days 7 and 10 of integration are probably due to the increased difference in positions of the synoptic weather systems.

Figure 4.5: 850-hPa temperature (color shaded, °C). The plots from left to right represent the model simulation, the corresponding NCEP reanalysis and the difference between the model and the reanalysis, respectively, after: (a) 24 h, (b) 72 h, (c) 120 h, (d) 168 h and (e) 240 h of integration of the model. The initial condition used was from 0000 UTC 18 April 2013.
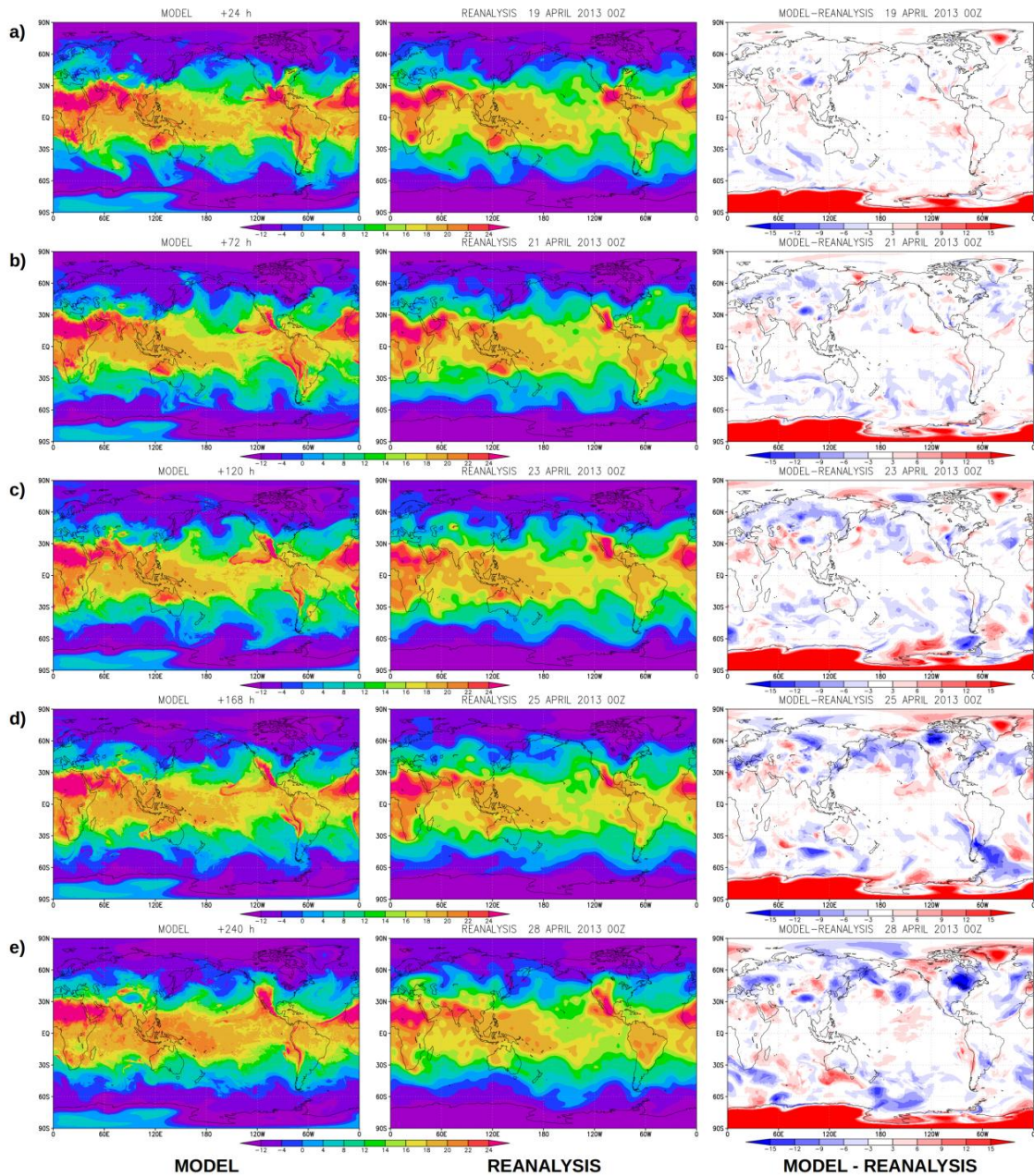

The simulated MSLP (Figure 4.6) correctly positions the highs and lows when compared with reanalysis up to day 5. The typical global pattern of MSLP

is maintained until the end of integration; however, the model starts to displace the positions of the synoptic scale systems and to simulate some lows and highs in the mid-latitudes that are not present in reanalysis particularly on day 10. Negative bias that appears in day 5 of simulation in equatorial regions of Africa and Indian Ocean spreads over Maritime continent and Pacific Ocean on day 10 of integration. Negative biases over Antarctica and positive over Arctic are probably due to inadequate initial conditions for snow depth and sea ice.

Figure 4.6: Mean sea level pressure (colored contours, hPa). The plots from left to right represent the model simulation, the corresponding NCEP reanalysis and the difference between the model and the reanalysis, respectively, after: (a) 24 h, (b) 72 h, (c) 120 h, (d) 168 h and (e) 240 h of integration of the model. The initial condition used was from 0000 UTC 18 April 2013.

MODEL **REANALYSIS** **MODEL - REANALYSIS**
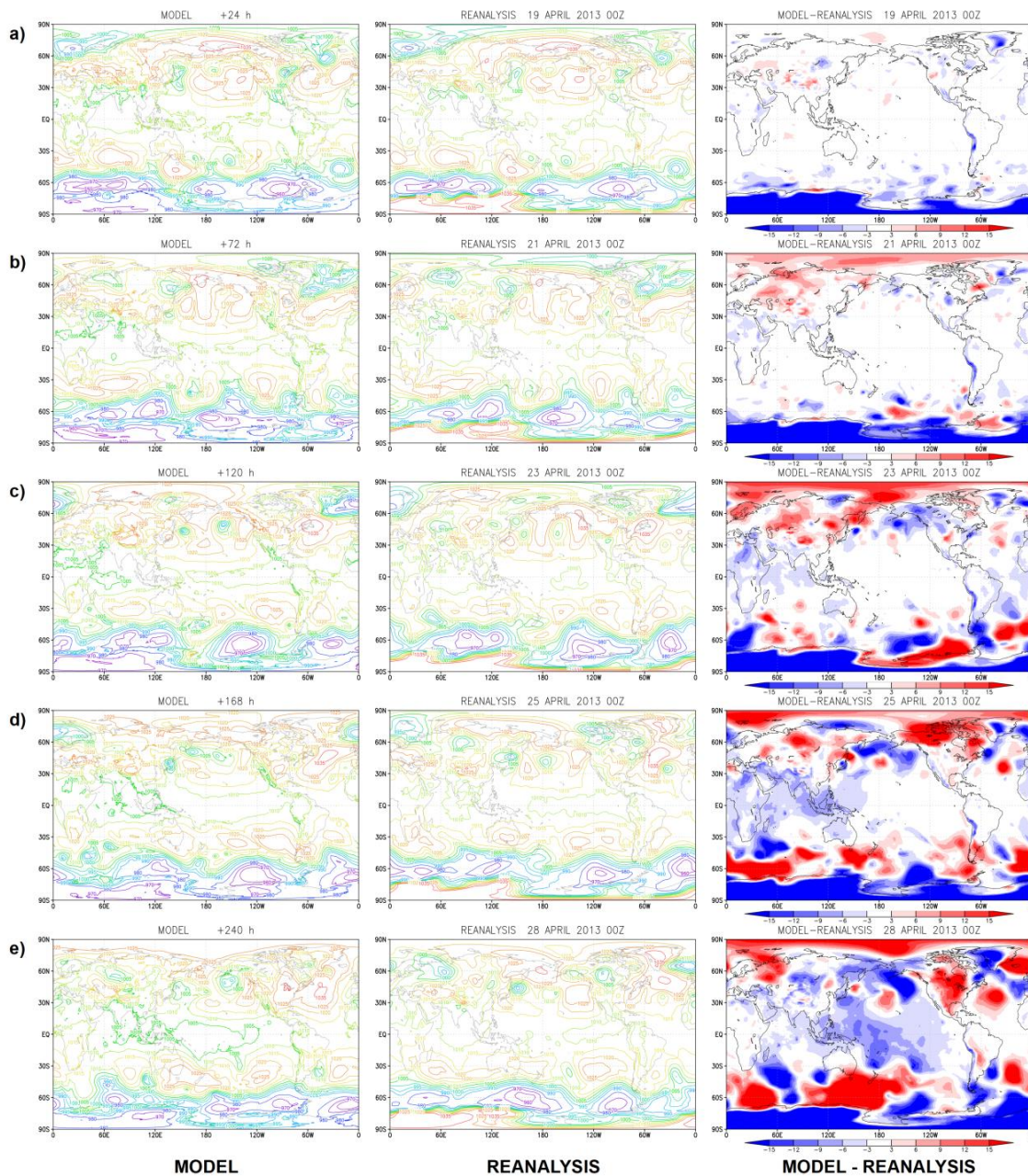
Time series of the global variables analyzed in this section are shown in Figure 4.5. Wind field at 200 hPa shows high level of agreement with reanalysis until day 7 of model simulation (Figure 4.7 a). The model slightly overestimates the values from reanalysis during the first 3 days, and then underestimates until day 7, but with the difference smaller than 0.6 m s^{-1}. After day 7, the model simulates the increase while the reanalysis shows the decrease of the wind magnitude. Time series of geopotential height at 500 hPa is well simulated by the model mostly with the difference of up to only 5 gpm from reanalysis (Figure 4.7 b). The exception is the day 10, where that difference is around 8 gpm. Winds at 850 hPa simulated by the model follow well the pattern from reanalysis, showing only minor differences in intensity (Figure 4.7 c). Different from the other fields, temperature at 850 hPa starts with overestimated value of around 1 degree Celsius on the day 1 of the model simulation, the error later decreases and the temperature approaches the values of reanalysis with the integration (Figure 4.7 d). The reason for that behaviour is probably the same as pointed in the seasonal integrations: the different discretization and vertical interpolations of temperature between model and reanalysis. MSLP is underestimated by the model with almost constant value of about 1 hPa (Figure 4.7 e), while the precipitation is overestimated by approximately 0.5 mm day^{-1} in the first 5 days of integration, but significantly increase that difference in the last 5 days of integration (Figure 4.7 f). Precipitation field will be analyzed objectively in the Section 4.4.

Figure 4.7: 10-days time series of global mean variables simulated by GEF (brown curves) and from corresponding NCEP reanalysis (blue curves): (a) 200-hPa wind speed (m s^{-1}), (b) 500-hPa geopotential (gpm), (c) 850-hPa wind speed (m s^{-1}), (d) 850-hPa temperature (°C), (e) mean sea level pressure (hPa) and (f) precipitation (mm day^{-1}). The initial condition used was from 0000 UTC 18 April 2013.
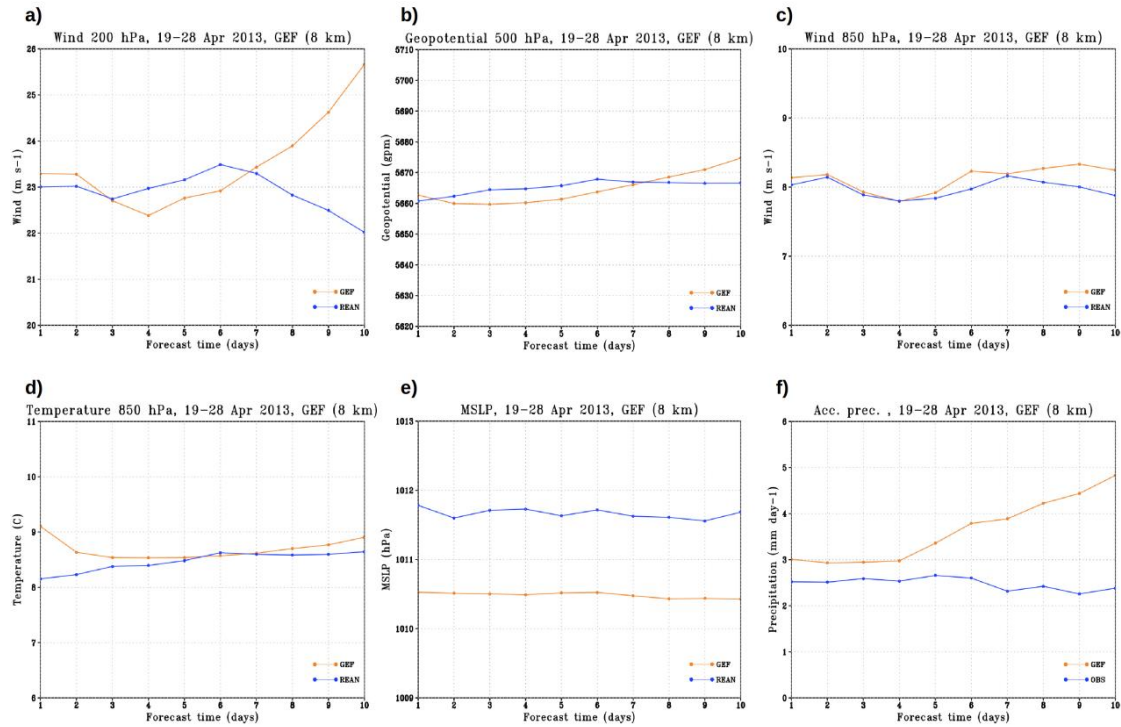
Figure 4.8 shows the reduction of spatial correlation during 10 days of integration. Geopotential height at 500 hPa shows the highest correlation with reanalysis. It starts with the value of approximately 0.99 for the first day of integration and decreases to 0.94 in the last day. Similar pattern and amplitude of decrease is present in the temperature correlation at 850 hPa, which starts with the correlation of 0.92 and ends with 0.86. Spatial correlation for the wind at 200 hPa has initial value of 0.96 and outperforms the spatial correlation of the temperature at 850 hPa during the first 3 days of integration. However, it decreases faster, shows lower values starting with the day 4 and ends with the correlation value of 0.62. Wind at 200 hPa and MSLP have similar values of

correlation of around 0.84 on the day 1 of integration and continue with similar values during the first 4 days of integration. Starting from day 5, the spatial correlation of MSLP shows higher decrease rate and ends with the value of 0.32, while the spatial correlation of the wind at 200 hPa has the value of 0.5 in the day 10 of integration. Simulated and observed precipitation pattern show the lowest level of correlation with values varying from 0.36 after 1 day of integration to 0.08 after 10 days of integration.

Figure 4.8: 10-days time series of spatial correlations between the global variables simulated by GEF and the corresponding NCEP reanalysis, represented by the curves of different colors for different variables: 200-hPa wind speed (turquoise), 500-hPa geopotential (red), 850-hPa wind speed (green), 850-hPa temperature (blue), (e) mean sea level pressure (brown) and precipitation (yellow). The initial condition used was from 0000 UTC 18 April 2013.
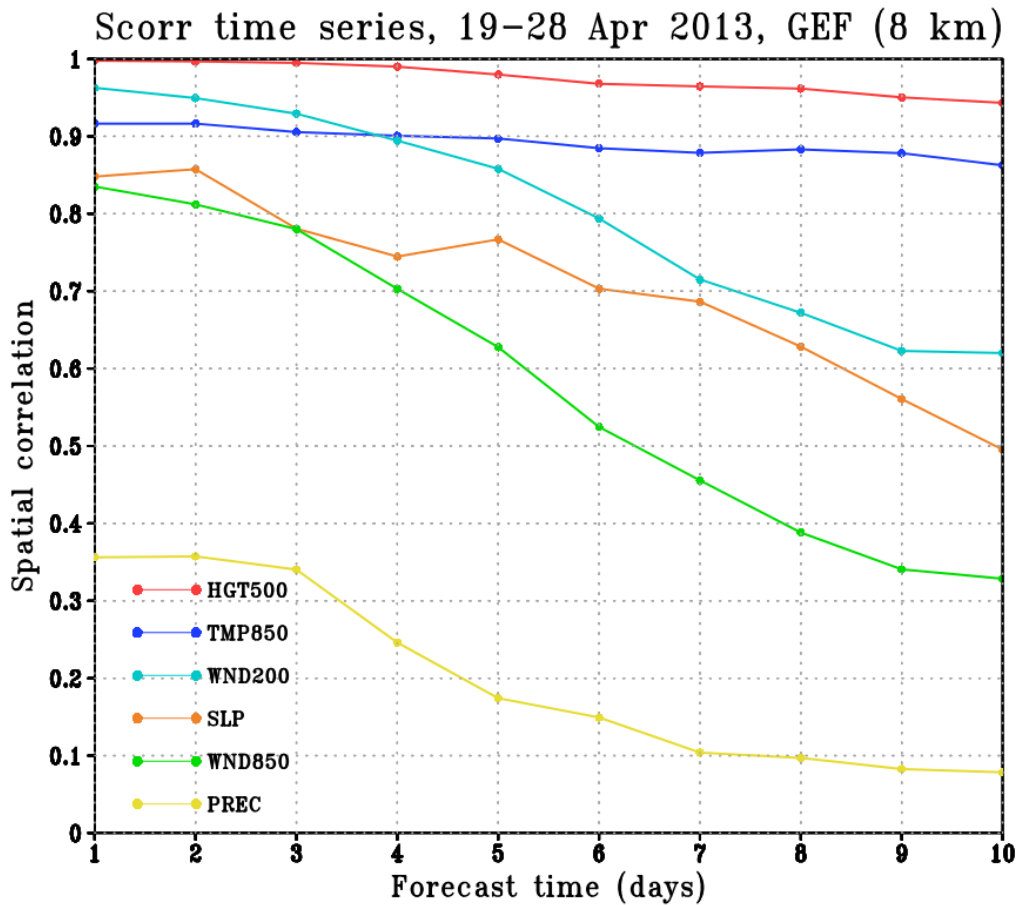
4.4 Statistical analysis for the region of South America

In the previous section, different global variables at different pressure levels are compared with the corresponding reanalysis variables with objective to assess the model in a medium-range simulation using a case study approach. In this section, the statistical analysis focuses on South America, in the region between 60°S – 20°N, 90°W – 30°W). In order to evaluate quantitatively the model simulations, RMSE is used as one of the standard methods to define the average magnitude of the errors. RMSE is used as the measure of difference between the values simulated by the model and the values from reanalysis. The ensemble from all 22 integrations is used. Figure 4.9 shows the evolution of RMSE during the 10 days of ensemble of integrations for the variables: wind at 200 hPa, geopotential height at 500 hPa, wind at 850 hPa, temperature at 850 hPa and MSLP. Mean values of 7-day evolution of RMSE for the year 2017 for South America (60°S – 15°N, 101.25^{o}W – 11.25^{o}W) that include 4 different models (GFS, CPTEC coupled model and 2 CPTEC ensembles) are shown in Figure 4.10. Due to the availability of the variables from different models, the plot uses 250-hPa wind and 850-hPa virtual temperature. The values of RMSE from the Figure 4.10 are used in this analysis as a reference, since the data are not completely comparable. RMSE for the wind at 200 hPa (Figure 4.9 a) starts with the value of approximately 4 m s^{-1}, exceeds 9 m s^{-1} on day 7 and ends with errors of about 11 m s^{-1}. These values are above all the values of RMSE from the models presented in similar case in Figure 4.10 a, where the values of the least accurate model are in the range 3.5 – 5.5 m s^{-1}. Beside the other mentioned differences, the winds from GEF simulations and wind from GFS are at two different pressure levels, what can probably give an extra contribution to the large RMSE. RMSE value of around 50 gpm for geopotential height at 500 hPa (Figure 4.9 b) on day 7 is comparable with the GFS model in the Figure 4.10 b. At the same time, the value of 17 gpm after day 1 is rather within the range of the values of other 3 models with inferior results then GFS, that starts with RMSE of 5 gpm. RMSE of the wind at 850 hPa (Figure 4.9 c) are similar in

the two CPTEC ensembles, being above the values of GFS, and below the CPTEC coupled model (Figure 4.10 c). Unlike the results from Figure 4.10 c, the values of RMSE for 850-hPa wind in Figure 4.9 c increase in a slower rate up to day 6 and remain with similar values until day 10. The evolution of RMSE of the temperature at 850 hPa (Figure 4.9 d) has the similar pattern as the RMSE for the wind at 850 hPa (Figure 4.9 c), the error increases until day 7 days and then remains with the similar values until day 10. The results after day 7 are comparable with all CPTEC global models in the Figure 4.10 d; however, these models start with small values of RMSE on day 1 and increase faster than wind RMSE. The RMSE of the GEF simulated MSLP (Figure 4.9 e) are comparable with the RMSE of the CPTEC global models (Figure 4.10 e) until the day 7, but smaller than RMSE of GFS, what shows good results in the analyzed fields in Figure 4.10.

Figure 4.9: 10-days Root Mean Square Error (RMSE) of GEF 22-member ensemble mean and corresponding NCEP reanalysis over South America (60°S – 20°N, 90°W – 30°W) for: (a) 200-hPa wind speed (m s^{-1}), (b) 500-hPa geopotential (gpm), (c) 850-hPa wind speed (m s^{-1}), (d) 850-hPa temperature (°C) and (e) mean sea level pressure (hPa).
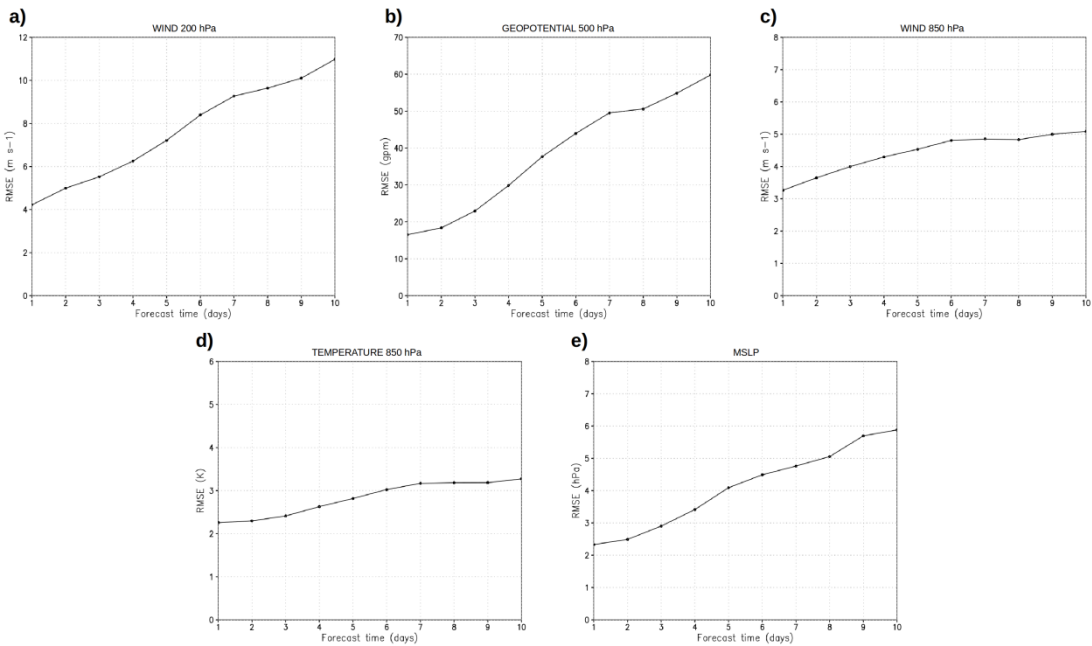
Source: Adapted from avaliacaodemodelos.cptec.inpe.br

Figure 4.10: 7-days Root Mean Square Error (RMSE) of 4 different global models (2017 annual mean) and corresponding analysis over South America (60°S – 15°N, 101.25°W – 11.25°W) for: (a) 250-hPa wind speed (m s^{-1}), (b) 500-hPa geopotential (gpm), (c) 850-hPa wind speed (m s^{-1}), (d) 850-hPa virtual temperature (K) and (e) mean sea level pressure (hPa). The models used (with RMSE represented with different colors) are: GFS (black), CPTEC coupled model (green), CPTEC global control ensemble (blue) and CPTEC global mean ensemble (yellow).
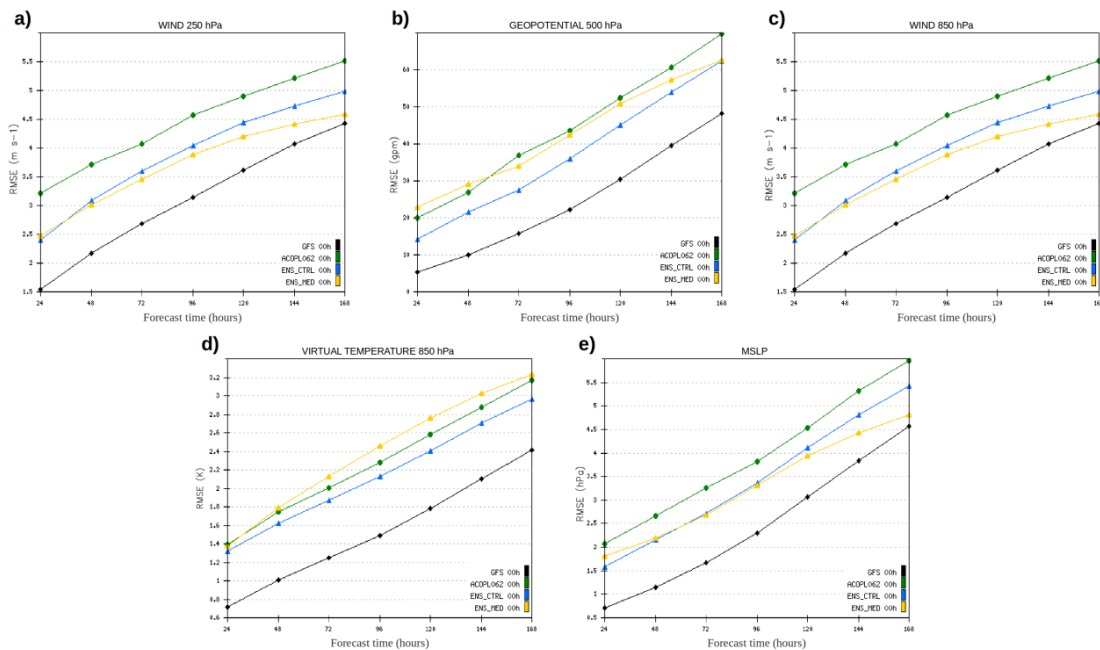
Source: Adapted from avaliacaodemodelos.cptec.inpe.br

For the quantitative evaluation of precipitation, ETS and BIAS are used. They are calculated for the forecast time ranges of 36 and 60 hours, and for the 22 integrations. The observed data used are from CMORPH and calculations are made in every grid box. ETS and BIAS (Figure 4.12) are shown for 8 models (global and regional), for the same time ranges (36 and 60 hours), representing the mean values for the year 2017 are used as a reference. The evaluation was performed against observed data from weather stations and only in the grid-boxes which contained at least one weather station. The models shown in this figure are: Eta, BRAMS and CCAT as representatives of the regional models in CPTEC and 2 versions of CPTEC global atmospheric model,

81

global ensemble, CPTEC coupled model and GFS. The plots from this figure are produced by the group of model evaluations at CPTEC and are publicly available on http://avaliacaodemodelos.cptec.inpe.br/ (last access: 09/02/2018). ETS values for the time range of 60 hours (Figure 4.11 b) are only 0.01-0.02 lower when compared with the values for the time range of 36 hours (Figure 4.11 a, upper plot) and both are with higher scores at lower precipitation thresholds, decreasing towards higher precipitation thresholds. The highest ETS value of approximately 0.35 is seen for the lowest threshold, which is considerably higher even above the highest score of all the models presented in Figure 4.12, in this case, the regional Eta model with the values between 0.25-0.27. That threshold can be regarded as the "rain-no rain" threshold and its high values indicate that the model simulated well the areas with precipitation. Unlike the majority of the models in Figure 4.12 that have higher score for the second lowest threshold then for the first, GEF has lower score, but still relatively high and within the range of other models. For heavier precipitation thresholds, the simulations scores are become generally low. BIAS with the value close to 1 for the rain-no-rain threshold for the time range of 36 hours (Figure 4.11 a) and 1.1 for the time range of 60 hours (Figure 4.11 b) indicates that precipitation is well simulated or slightly overestimated at that threshold. However, for raining thresholds, BIAS decrease significantly to approximately 0.4, and reach 0.1, for the heaviest precipitation thresholds. Most of the other models in lower plots of Figure 4.12 a and Figure 4.12 b start with the values of BIAS between 1.7 and 2.7, overestimating the light rain, continue with mostly well simulated moderate rain with BIAS values around 1 and underestimating heavy rain with the BIAS lower than 1, going down to 0.05.

Figure 4.11: Equitable Threat Score (ETS) (upper plots) and Bias Score (BIAS) (lower plots) of GEF (22-integrations mean) for South America (60°S – 20°N, 90° – 30°W) and for the forecast time ranges of: (a) 36 hours, (b) 60 hours and (c) for both ranges together. The observation data used are CMORPH and calculations are performed in every grid box.
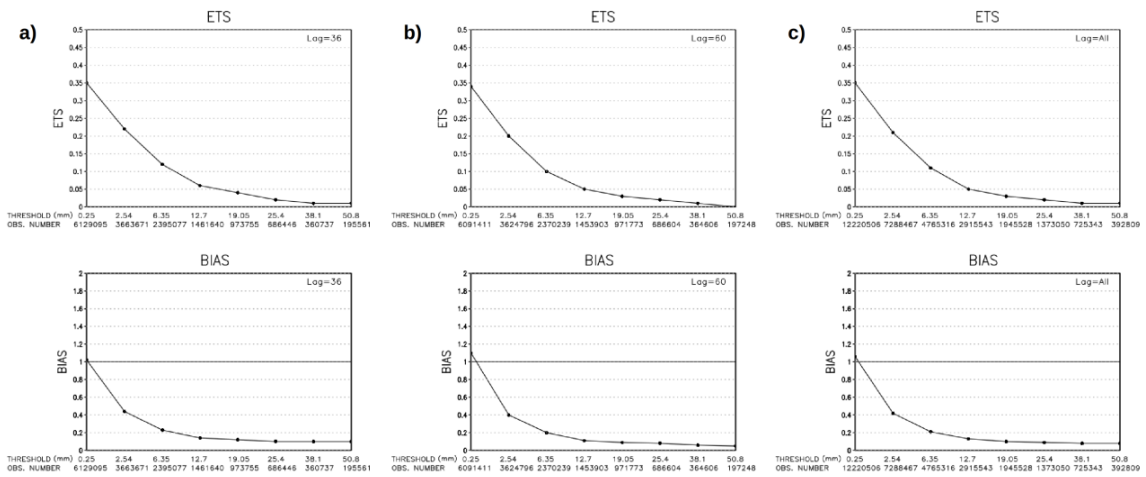
Figure 4.12: Equitable Threat Score (ETS) (upper plots) and Bias Score (BIAS) (lower plots) of 8 different models (2017 annual mean) for South America (50°S – 12°N, 83°W – 34°W) and for the forecast time ranges of: (a) 36 hours and (b) 60 hours. The models used (with ETS and BIAS represented with different colors) are: Eta model 15 km (dark blue), BRAMS 5 km (green), CCAT (pink) as representatives of the regional models in CPTEC and 2 versions of CPTEC global atmospheric model - T213L42 (army green) and T126L28 (blue), CPTEC global ensemble (orange), CPTEC coupled model (dark green) and GFS (black). The observation data used are from weather stations and calculations are performed only in the grid-boxes which contained at least one weather station.
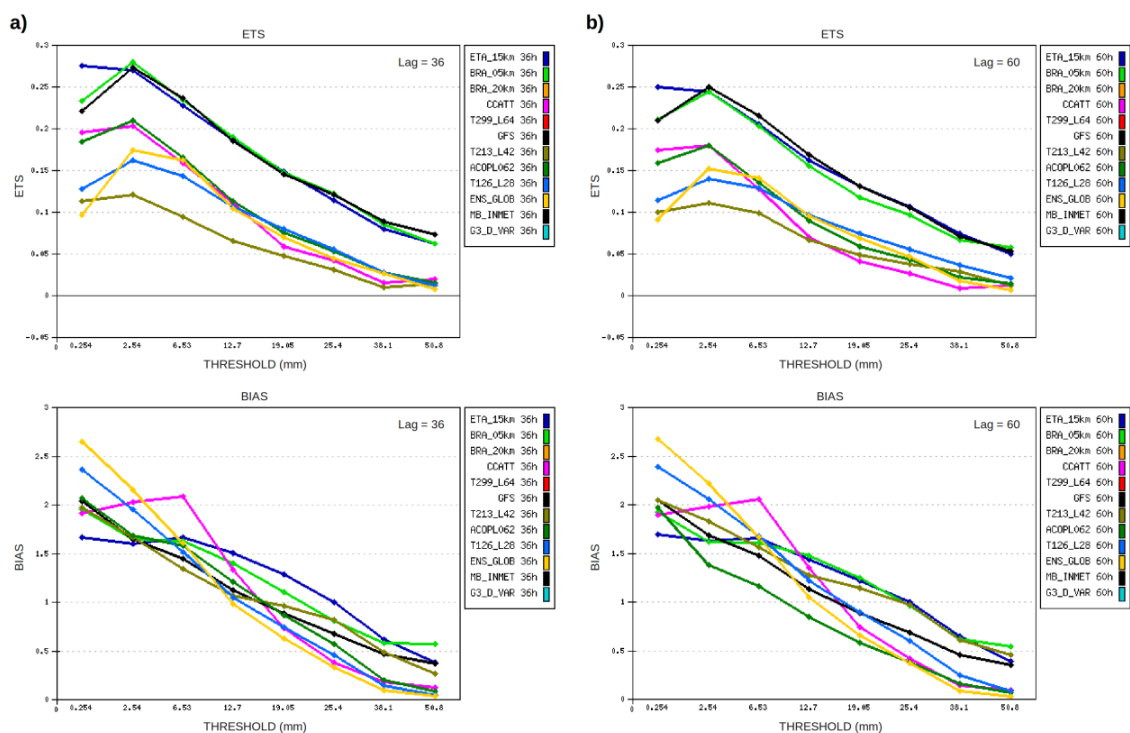
Source: Adapted from avaliacaodemodelos.cptec.inpe.br

Time series of daily mean precipitation for different regions of Brazil are shown in Figure 4.13. The four regions are defined (Figure 4.13 e) according to their different patterns and different origins of precipitation. The region that approximately covers the Amazon basin (AM) is characterized by precipitation primarily produced by isolated showers from deep convection and also by some organized systems such as the synoptic-scale squall lines that are formed by sea-breeze-induced instability in north-eastern coast of South America, or the

cold fronts that reach lower latitudes. The precipitation in the north and northeast region of Brazil (NNE) is mostly controlled by the ITCZ activity and the sea breeze circulation during the year or by the frequent easterly travelling disturbances from the Atlantic anticyclone during winter months. Western-central region (WC) shows remarkable contrast between the summer and winter precipitation patterns that are highly dependent on South American monsoon activity. The origin of precipitation is both tropical, from mesoscale convective systems coming from the Amazon region, and extratropical from cold fronts and squall lines. The region of south and southeast (SSE) is predominantly influenced by the frontal systems, mesoscale convective systems and South Atlantic Convergence Zone in the summer months.

Figure 4.13: 9-days time series of accumulated precipitation (mm day^{-1}) for 4 different regions of Brazil: (a) Amazon (AM), (b) North-northeast (NNE), (c) Western-central (WC) and (d) South-southeast (SSE). Map of these regions is presented in (e). The initial condition used was from 0000 UTC 18 April 2013.
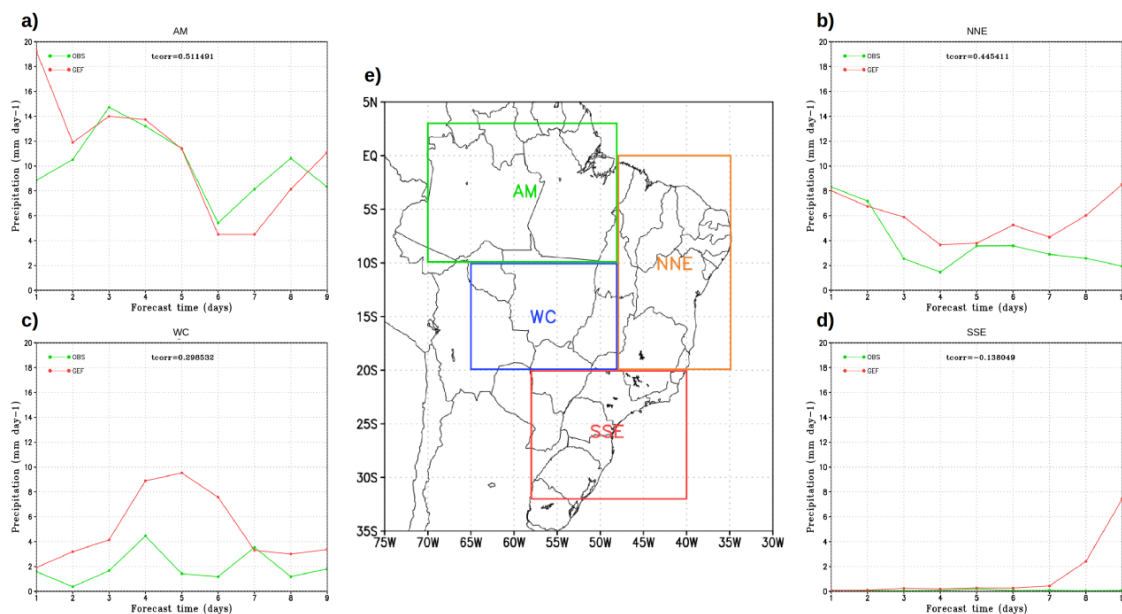
In the Amazon region (AM, Figure 4.13 a), the model simulates well the precipitation, following the observed pattern, although on the first 2 days

precipitation is overestimated. In the last 3 days, despite the agreement in the pattern, the precipitation rate is underestimated. Two precipitation peaks, on days 3 and 8, are captured by the model, although it overestimates on the first day of simulation. Precipitation pattern for the NNE region (Figure 4.13 b) shows delay by about 1 day in the simulation of the peaks of precipitation. The simulated precipitation is slightly overestimated, but the difference between simulated and observed precipitation increases after the day 7. In the Western-central region (WC, Figure 4.13 c), two observed peaks on days 4 and 7, are shown by the model as only one peak of heavier precipitation on day 5. During the analyzed period, there were a little or no rain in observation data in South-southeast region (Figure 4.13 d), which corresponds to the model simulation during the first 7 days.

4.5 Analysis of the cases of extreme precipitation in Manaus, AM

This section describes the cases with intense precipitation over the city of Manaus, AM. The objective is to evaluate the model skill to simulate the events of extreme precipitation in tropical environment with lead times of 24, 48 and 72 hours. One selected case on the 21st April 2013 is discussed in more detail. The other cases, the study will focus on the analysis of intensity and spatial distribution of precipitation over South America and the Amazon region, comparing the simulated precipitation against the observations for the integration lead times of 24, 48 and 72 hours. Figure 4.14 shows different atmospheric fields at 250 hPa, 500 hPa, and 850 hPa levels and at the surface, where upper plots are model outputs on the day 21 April 2013 0000 UTC, with the lead time of 72 hours, and lower plots are from CPTEC analysis. The latter plots are produced by CPTEC weather forecast group and are part of daily technical bulletin that is publicly available on the institution's site (http://tempo.cptec.inpe.br/boletimtecnico/pt, last access 09/02/2018). Anticyclonic circulation is predominant over the southern Brazil, Uruguay and north-eastern Argentina in the upper levels of the atmosphere (Figure 4.14 a).

That configuration represents resembles the pattern of "blocking" situation, that was present in the region in previous days. This system is well represented by the model, including the ridge over the region of Andes, between northern Chile and western Argentina; however, with less intense trough west of the anticylone. Cyclonic circulation west of southern Chile, together with adjacent subtropical jet and subpolar jet that extends to Atlantic ocean over the Drake passage, corresponds both in position and intensity to the pattern simulated by the model. Well defined anticyclonic circulation in the tropical latitudes of the eastern Pacific is followed by the trough and the ridge positioned over the continent between the latitudes of 10° S and 20° S. In the model simulation, that anticyclonic circulation is not as pronounced and the wave-like pattern is missing over the continent. On the other hand, cyclonic circulation over tropical Atlantic Ocean from the analysis is present in the model in the form of well developed and more intense upper tropospheric cyclonic vortex with the centre positioned closer to the continent. The wave-like pattern and the sequence of cyclonic and anticyclonic circulations in the upper levels of the mid-latitudes latitudes, is also present in the lower levels. The simulated 500-hPa geopotential height (Figure 4.14 b) and wind intensity are comparable with the reanalyses. Similar pattern is also noticed at 850-hPa level south of 20° S (Figure 4.14 c). High in the geopotential height with the centre positioned southeast of the Uruguay coast is weakly simulated by the model. The northern branch of the anticyclonic flow, that corresponds to the mentioned mid-latitude ridge, together with equatorial easterlies, contributes to the mass convergence in the central Amazon, which is present both in the analysis and in the model. In the analysis of the pressure field at the surface (Figure 4.14 d), the anticyclone centre in the South Atlantic, east of the coast of Argentina, is weakly simulated by the model. The cold front associated with the cyclone further to the east of Atlantic corresponds to the position of the small perturbations in the pressure field simulated by the model. The cyclone west of southern Chile is well positioned in the model; however, an additional centre of low pressure is simulated further to the southwest.

Figure 4.14: Composites of: (a) 250-hPa wind streamlines and wind speed (color shaded in m s^{-1}), (b) 500-hPa geopotential height (contours in gpm) and wind speed (color shaded in m s^{-1}), (c) 850-hPa wind streamlines and geopotential height (colored contours in gpm) and (d) mean se level pressure (colored contours in hPa). The upper plots represent GEF 72-h lead time simulations with initial condition used from 00:00 UTC 18 April 2013 and the lower plots represent appropriate CPTEC analysis with some additional fields, that are not presented in the model. 250-hPa and 500-hPa wind speed in CPTEC analysis is represented in knots.
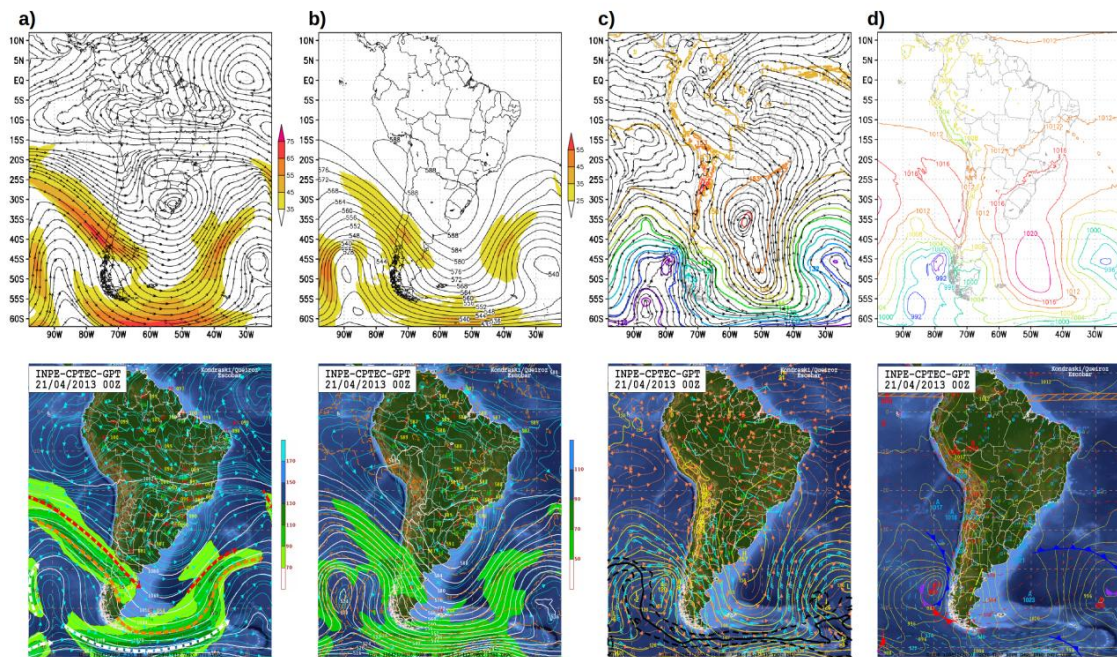
Source: Adapted from tempo.cptec.inpe.br/boletimtecnico/pt

The 24-h accumulated global precipitation (Figure 4.15) for 21 April 2013 0000 UTC simulated with the lead time of 72 h (Figure 4.15 a), 48 h (Figure 4.15 b), and 24 h (Figure 4.15 c) is compared against observed data from CMORPH (Figure 4.15 d). In all lead times, the model simulates the typical global pattern, such as the ITCZ, synoptic scale systems and frontal zones related precipitation. The model underestimates moderate to heavy precipitation, although light rain is overestimated.

Figure 4.15: Global daily accumulated precipitation (mm day⁻¹) for 0000 UTC 21 April 2013 simulated by GEF with the lead time of: (a) 72 h, (b) 48 h, (c) 24 h and (d) corresponding CMORPH precipitation data
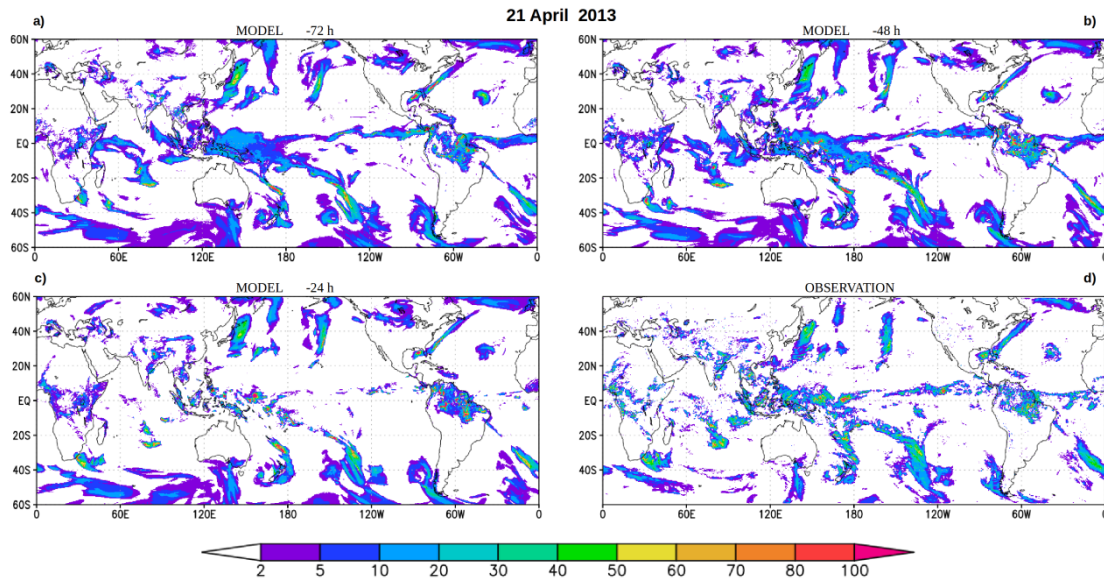
The period between 20 and 22 April 2013 was characterized by large areas of convective instability that caused heavy rainfall in Brazilian states of Amazonas and Pará. A zone of moisture present in the previous days (17 and 18 of April 2018, figures not shown) propagated in the northwest-southeast direction reaching the nortwesternmost areas of the states of Amazonas and Pará. The moisture convergence zone remained over the area for a few days (Figure 4.14 c). This moisture convergence and the warm air temperature lead to vertical movements and formation of the deep convection and precipitation. The Brazilian National Institute of Meteorology (INMET) registered precipitation of 117.4 mm on 21 of April and 140 mm on 22 of April (measurements are taken at 8 AM, local time) in the city of Manaus. The measured amount of 140 mm day⁻¹ on 22 of April 2013 was the heaviest registered in Manaus in that year. The total of 257.4 mm day⁻¹ accumulated in 48 hours has almost reached the average monthly amount of 311.2 mm day⁻¹. Figure 4.16 shows 24-h accumulated precipitation on 20 April 2013 0000 UTC over South America

(upper plots) and over the Central Amazon, 10° S – 5° N, 70° W - 50° W, for the simulations with lead time of 72 h, 48 h, and 24 h and observation. The area with intense precipitation occurred over the northern part of the continent, mostly over the Amazon region and Brazilian Northeast. The band of precipitation that spreads approximately between the equator and 5° N over the Atlantic Ocean corresponds to the ITCZ and narrow band of precipitation that extends from the coast of Brazilian state of Bahia towards southeast corresponds to the part of the weakening moisture convergence zone, which was active in the region in the previous days. In all lead times, the model simulated well the position of precipitation areas in tropics, changing mostly the intensity of the precipitation maxima, giving more locally intense precipitation in 24 h lead time, which is clear in the plots of the Central Amazon. The model simulates rain of different intensity inside in Manaus city in all lead times, between 5-20 mm day^{-1} in the centre of the city and over 100 mm day^{-1} near the borders of the city in the 48-h lead time. However, CMORPH estimate show less precipitation than observed by INMET station data, with difference of up to 50 mm day^{-1} between the two datasets. That difference in observed data might be attributed to the different time of measurements and to the technique used by the CMORPH data set to estimate precipitation.

Figure 4.16: Daily accumulated precipitation (mm day^{-1}) for 0000 UTC 20 April 2013 for: (a) South America (60°S – 20°N, 90°W – 30°W) and (b) Central Amazon (10°S – 5°N, 70°W – 50°W). Plots from left to right represent the simulations by GEF with the lead time of: (a) 72 h, (b) 48 h, (c) 24 h and (d) corresponding CMORPH precipitation data, respectively. The black square in the middle of the lower plots (3.5°S – 2.5°S, 60.5°W – 59.5°W) represents the area that surrounds the city of Manaus (3.1190°S, 60.0217°W), which is positioned approximately in the centre of that square.

Figure 4.17 shows the same as the Figure 4.16, but for the following day, 21 April 2013 0000 UTC. Precipitation east of southern Chile that extends to the South Atlantic Ocean corresponds to the frontal zones observed in the Figure 4.16 d. Almost the same precipitation pattern as in Figure 4.16 can be observed in the tropical region of South America. The plots over the Central Amazon reveal that the position of the precipitation maxima changes depending on the lead time and that these maxima are generally more intense than in observations. The 24-h lead time precipitation simulation in the city of Manaus shows very similar pattern with the observations, only with slightly underestimated precipitation. In longer lead times, the precipitation intensity in

the Manaus area is comparable with the observation, but still weaker precipitation then observed by INMET, probably due to the same reasons mentioned in the comments of the previous figure.

Figure 4.17: Daily accumulated precipitation (mm day^{-1}) for 00:00 UTC 21 April 2013 for: (a) South America (60°S – 20°N, 90°W – 30°W) and (b) Central Amazon (10°S – 5°N, 70°W – 50°W). Plots from left to right represent the simulations by GEF with the lead time of: (a) 72 h, (b) 48 h, (c) 24 h and (d) corresponding CMORPH precipitation data, respectively. The black square in the middle of the lower plots (3.5 – 2.5°S, 60.5° – 59.5°W) represents the area that surrounds the city of Manaus (3.1190°S, 60.0217°W), which is positioned approximately in the centre of that square.
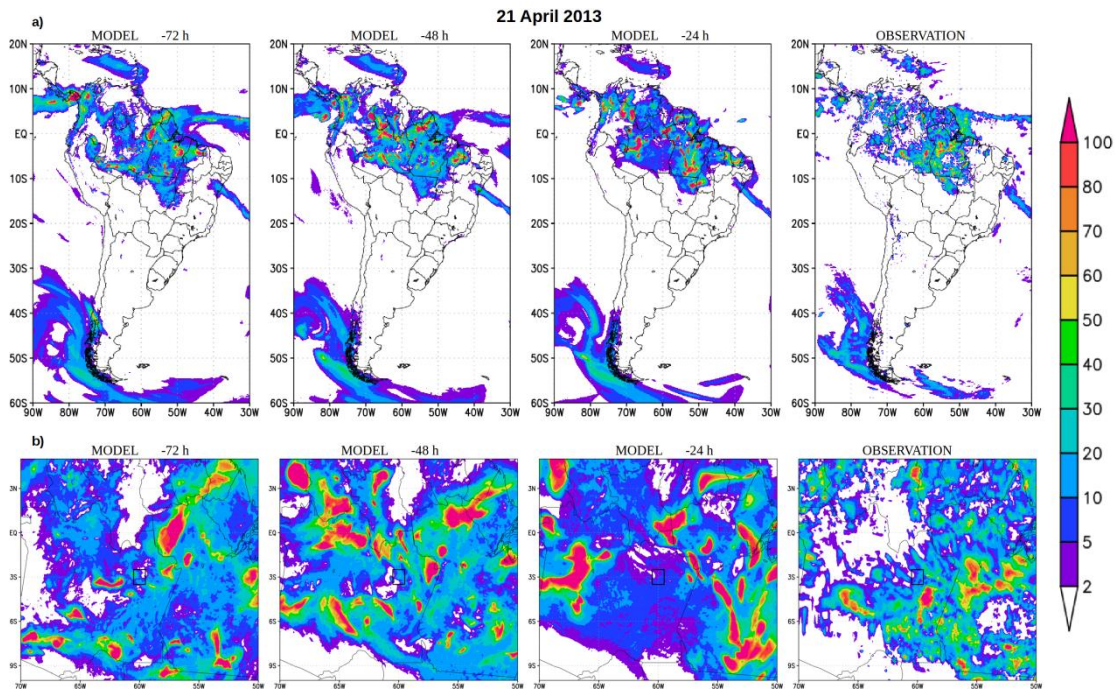
In the evening hours of 30 October 2012, severe thunderstorm hit the city of Manaus, followed by the strong wind that reached 66 km h^{-1}, according to the data from the INMET automatic weather station. The strongest wind gusts of 85 km h^{-1} was recorded in the weather station at the Manaus International Airport "Eduardo Gomes". The total precipitation measured on 31 October 2012 at 8 AM was 81.4 mm day^{-1}. The total accumulated precipitation during the month of

October was 181.4 mm day^{-1}. This is 61% larger than the average precipitation for this month, which is 112.6 mm day^{-1}. October is the month of transition from dry to rainy season in that region, characterized by strong thunderstorms and episodes of heavy rain. The temperatures reach high values, which, with the presence of more humidity, contribute to the development of severe thunderstorms. Figure 4.18 shows the 24-h precipitation for the day 31 October 2012 0000 UTC. The model simulation with 72-h lead time shows the precipitation maxima over Pacific coast of Colombia and over southern Brazil, but no precipitation in the Amazon region. In the 48-h and 24-h lead times, the model reduces the precipitation maxima in southern Brazil and approaches the observed values but some maxima appear over the Amazon region. Spatial distribution of precipitation is reasonably reproduced over the entire continent; however, precipitation is mostly underestimated, especially in the tropical regions. The band of precipitation over Central Amazon is correctly positioned, despite the mostly underestimated values, except in the 24-h lead time simulation, where some precipitation maxima appear. Precipitation in the surroundings of the city of Manaus is mostly underestimated by the model, only in the 24-h lead time simulation, the region north of the city received the precipitation amount comparable with the observation, that shows the maximum of precipitation south of the city. These values are also comparable with the INMET data.

Figure 4.18: Daily accumulated precipitation (mm day⁻¹) for 0000 UTC 31 October 2012 for: (a) South America (60°S – 20°N, 90°W – 30°W) and (b) Central Amazon (10°S – 5°N, 70°W – 50°W). Plots from left to right represent the simulations by GEF with the lead time of: (a) 72 h, (b) 48 h, (c) 24 h and (d) corresponding CMORPH precipitation data, respectively. The black square in the middle of the lower plots (3.5°S – 2.5°S, 60.5°W – 59.5°W) represents the area that surrounds the city of Manaus (3.1190°S, 60.0217°W), which is positioned approximately in the center of that square.

In the case of 8 November 2012, heavy rain started in the early afternoon hours and accumulated 60 mm in only one hour, more than a third of the expected accumulated amount for the month (173.8 mm day⁻¹). The warmest air temperature of 37.1° C for that year, registered the day before, contributed to this extreme rainfall. No intense winds were detected in the city during the event. Similar as for the previous month, the total accumulated for the month of November of 2012 was 284.5 mm day⁻¹, that is 63% higher than the average for that month. Figure 4.19 shows the daily accumulated precipitation for the South America and Central Amazon for the day 8 November 2012 0000 UTC. Precipitation in the mid-latitude regions, related with the synoptic scale systems

is mostly well simulated in all simulation lead times, both in terms of the spatial distribution and intensity. The exception is the band of precipitation that extends from central Argentina toward southeast, which is underestimated by the model. Precipitation over tropical regions of South America is mostly well positioned and mostly underestimated by the model in the all lead times, with exception of central and eastern regions of Brazil, where the model simulates more intense maxima than observed. In the Central Amazon (Figure 4.19 b), it seems that the simulation of the spatial distribution of precipitation is better reproduced in the lead times 48 h and 24 h, when compared with the lead time 72 h; however, still with underestimated values of precipitation. In the area around the city of Manaus, the model simulates accumulated rain of up to 20 mm day^{-1} in 48 h lead time, while the observations show the values of up to 60 mm day^{-1}, that corresponds to the values observed by INMET.

Figure 4.19: Daily accumulated precipitation (mm day^{-1}) for 0000 UTC 8 November 2012 for: (a) South America (60°S – 20°N, 90°W – 30°W) and (b) Central Amazon (10°S – 5°N, 70°W – 50°W). Plots from left to right represent the simulations by GEF with the lead time of: (a) 72 h, (b) 48 h, (c) 24 h and (d) corresponding CMORPH precipitation data, respectively. The black square in the middle of the lower plots (3.5°S – 2.5°S, 60.5°W – 59.5°W) represents the area that surrounds the city of Manaus (3.1190°S, 60.0217°W), which is positioned approximately in the centre of that square.
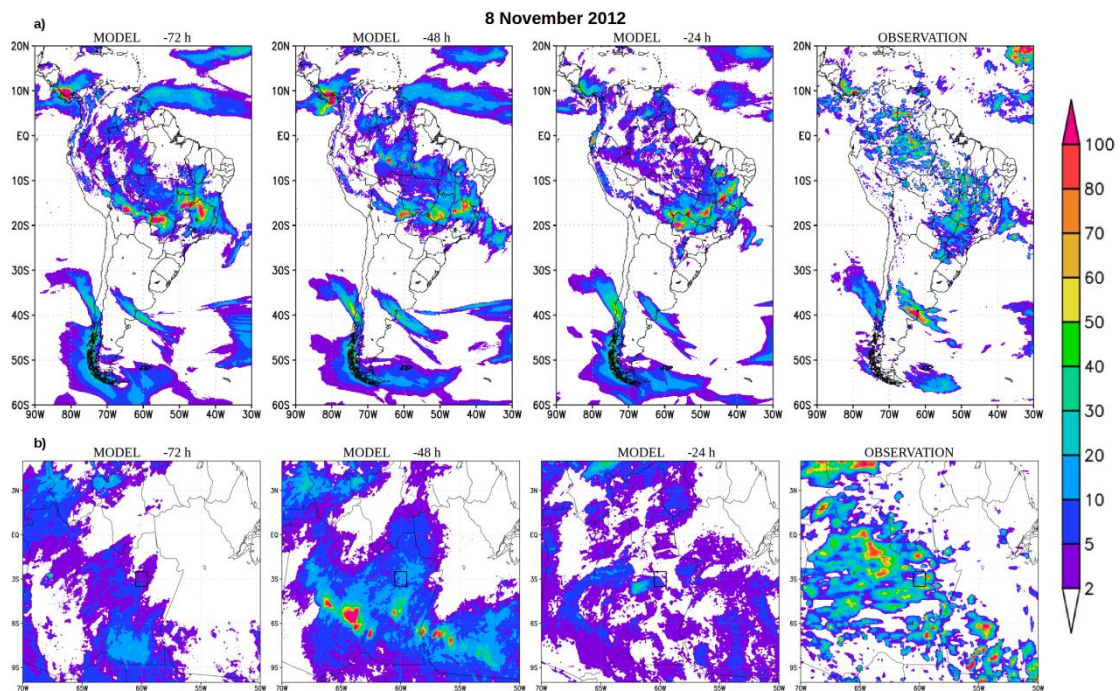
Severe thunderstorm, that started in the late morning of 30 September 2013 was followed by heavy rain, hail, and wind gusts of up to 92 km h^{-1}. The total of 114 mm day^{-1} of rainfall was registered by INMET for that day. In only 3 hours of this extreme event, between 10 AM and 1 PM, it was registered 89 mm of rain, more than the average of the entire month (83 mm). Squall line that formed over the western border of the state of Pará moved towards northwest, in the direction of the city of Manaus, bringing intense rain, uncommon for generally one of the driest months of the year for that region. Warm air temperature observed in the city of Manaus during the day of the extreme event contributed to the development of the cumulonimbus clouds and intensification

of precipitation and wind. The temperature of 34° C that was observed before the rains, dropped to 22° C within only one hour. Figure 4.20 shows the 24-h accumulated precipitation for 30 September 2013 0000 UTC. In all lead times, the model shows difficulties to properly position the precipitation over southeast of Brazil. However, the intensity of the precipitation mostly corresponds to the observed. Precipitation in the central Brazil and in the Amazon region is correctly positioned, but it is mostly underestimated. The band of precipitation in central Amazon was better simulated in the 72 h and 48 h lead times than in the 24 h lead time. Some simulated precipitation maxima, comparable with the maxima in observations, appear in 24 h lead time simulation, but not in the correct position. Simulated precipitation in the surroundings of the city of Manaus reaches the highest value of 20 mm day^{-1} in the 24 h lead time, still less than in observation, that registered 60 mm day^{-1}, which is also significantly weaker than observed by INMET.

Figure 4.20: Daily accumulated precipitation (mm day^{-1}) for 0000 UTC 30 September 2013 for: (a) South America (60°S – 20°N, 90°W – 30°W) and (b) Central Amazon (10°S – 5°N, 70°W – 50°W). Plots from left to right represent the simulations by GEF with the lead time of: (a) 72 h, (b) 48 h, (c) 24 h and (d) corresponding CMORPH precipitation data, respectively. The black square in the middle of the lower plots (3.5°S – 2.5°S, 60.5°W – 59.5°W) represents the area that surrounds the city of Manaus (3.1190°S, 60.0217°W), which is positioned approximately in the center of that square.

Continuous rain during the period of 6 hours was observed on 19 November 2013 in Manaus. The total of 73 mm day^{-1} of rainfall was recorded according to the data from INMET weather station with the strongest wind of 40 km h^{-1}. Including the precipitation from that day, the total expected for the month of November has already been reached in only 19 days. The weather station located in the north-western part of the city at the Manaus International Airport "Eduardo Gomes" registered the precipitation of 56 mm day^{-1} and the wind gusts of 52 km h^{-1}, while in the southern part of the city, another weather station located at the Military Airport "Ponta Pelada" registered the precipitation of 40 mm day^{-1} and the wind gusts of 48 km h^{-1}, showing the high spatial variability of

the precipitation in a relatively small territory and the local character of this extreme event. The model simulated well the extreme precipitation over the northern Argentina and Uruguay (Figure 4.21 a) in all lead times, while the simulation of precipitation over the central Brazil and the Amazon region improved with the lead times closer to the day of extreme event. That can be seen in more detail in Figure 4.21 b, where the precipitation band in the 72 h lead time is positioned more towards southwest, improving in the 48 h lead time and even with some precipitation maxima comparable in intensity with the observation in the 24 h lead time. However, these maxima are not correctly positioned, therefore, the precipitation over the city of Manaus is significantly underestimated. The observed data show the values comparable with the INMET data, between 70 and 80 mm near the city of Manaus and the values above 100 mm/day south of the city.
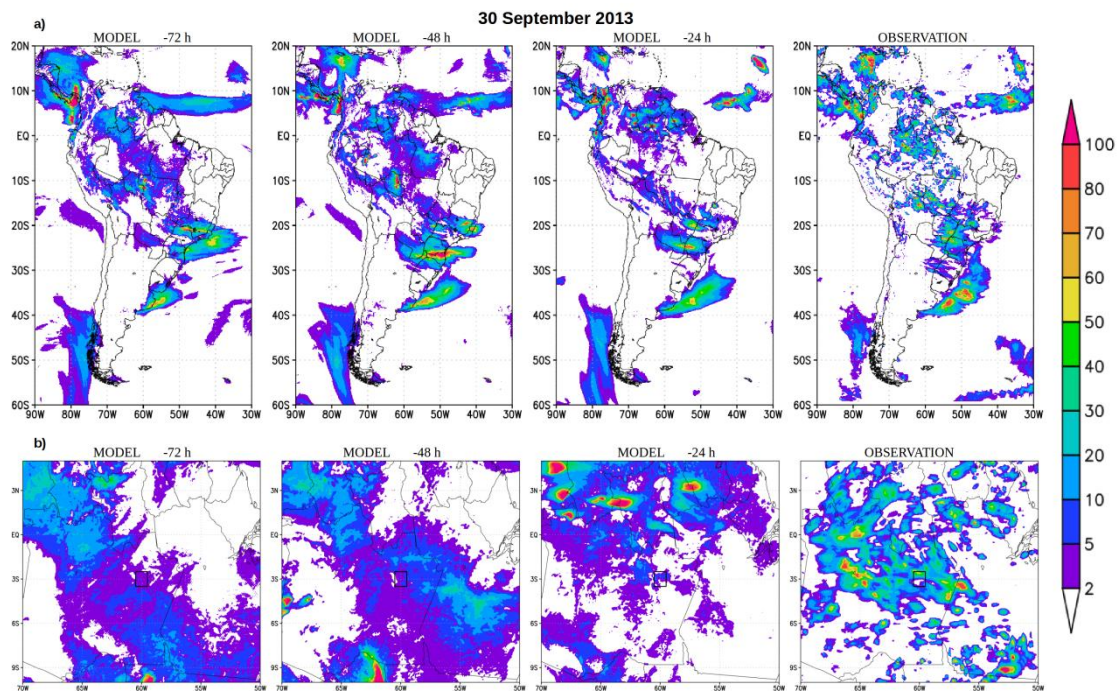
Figure 4.21: Daily accumulated precipitation (mm day⁻¹) for 0000 UTC 19 November 2013 for: (a) South America (60°S – 20°N, 90°W – 30°W) and (b) Central Amazon (10°S – 5°N, 70°W – 50°W). Plots from left to right represent the simulations by GEF with the lead time of: (a) 72 h, (b) 48 h, (c) 24 h and (d) corresponding CMORPH precipitation data, respectively. The black square in the middle of the lower plots (3.5°S – 2.5°S, 60.5°W – 59.5°W) represents the area that surrounds the city of Manaus (3.1190°S, 60.0217°W), which is positioned approximately in the centre of that square.
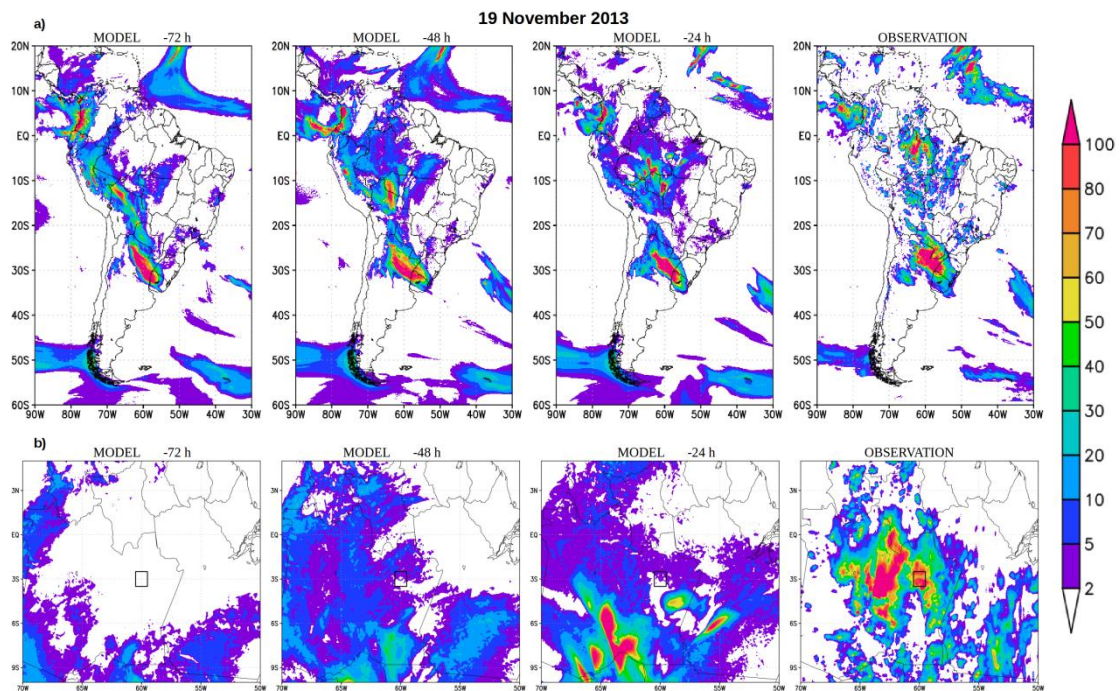
The event of 9 September 2016 was characterized by heavy rainfall in early morning hours. According to the data of the Amazon Protection System (SIPAM), in approximately 2 hours, it was registered 44 mm day⁻¹, 35 mm day⁻¹ and 33 mm day⁻¹ of rainfall in 3 different weather stations in different locations of the city and even 66 mm/day in one of the suburbs of Manaus, following the precipitation data from the Municipal Civil Defence. The temperature dropped from 28.6° C to 23.4° C during the period of extreme event. The precipitation band over the northern part of the continent (Figure 4.22 a) was mostly well positioned in all lead times, but with underestimated values. The southern edge of that precipitation band was over the city of Manaus (Figure 4.22 b) and

caused the observed heavy rainfall. The model simulated rain over Manaus in all lead times; however, with the intensity underestimated.

Figure 4.22: Daily accumulated precipitation (mm day^{-1}) for 0000 UTC 9 September 2016 for: (a) South America (60°S – 20°N, 90°W – 30°W) and (b) Central Amazon (10°S – 5°N, 70°W – 50°W). Plots from left to right represent the simulations by GEF with the lead time of: (a) 72 h, (b) 48 h, (c) 24 h and (d) corresponding CMORPH precipitation data, respectively. The black square in the middle of the lower plots (3.5°S – 2.5°S, 60.5° – 59.5°W) represents the area that surrounds the city of Manaus (3.1190°S, 60.0217°W), which is positioned approximately in the centre of that square.
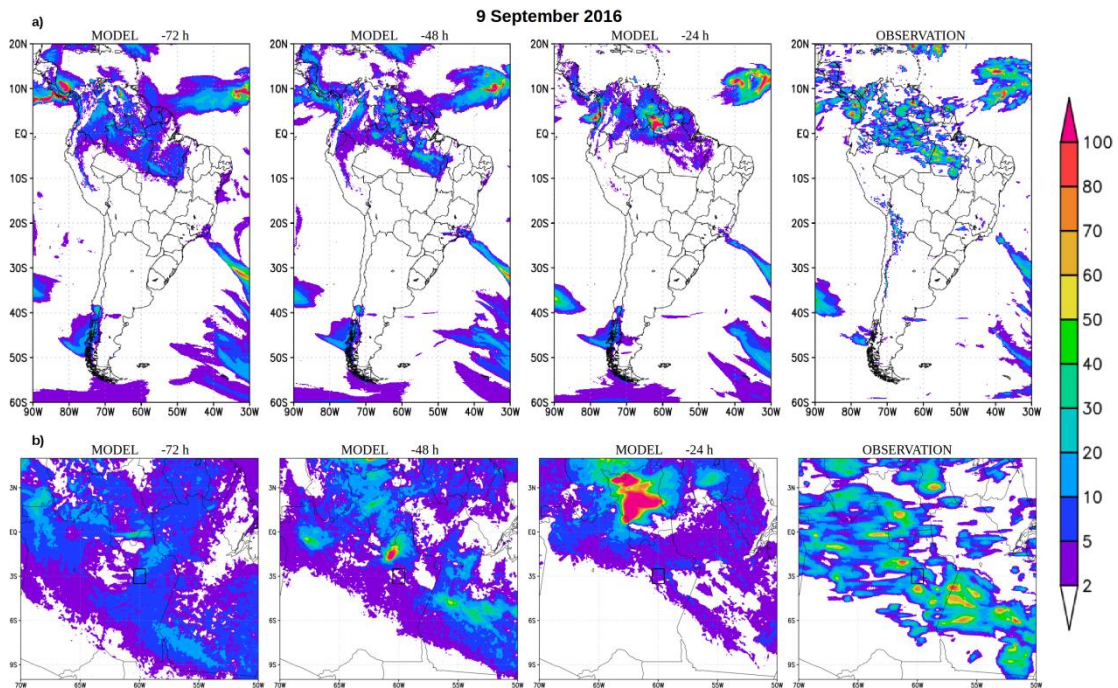
The event of 17 November 2016 was severe only in the intensity of the wind, but not in the intensity of the precipitation. The squall line that formed in the area southwest of Manaus reached the area of the city in the morning hours causing the wind gusts of over 50 km h^{-1}, but it was registered only 15 mm of the rainfall for the period of 2 hours. The simulated spatial distribution of the precipitation over the tropical area of South America was mostly comparable with the observation, especially in the simulations with the lead times of 48 h and 24 h (Figure 4.23 a). Simulated precipitation in the tropics was mostly

underestimated, while in the mid-latitude regions, the precipitation band spreading over the northern Argentina, Uruguay, and southern Brazil was well positioned and with overestimated values simulated by the model, in all lead times. Several areas with the extreme precipitation over 100 mm day^{-1} were observed over the Central Amazon (Figure 4.23 b), but not over Manaus, where the total accumulated daily precipitation varied between 20 mm day^{-1} and 30 mm day^{-1}. The areas with precipitation in the Central Amazon were mostly simulated well by the model, but the precipitation maxima were not captured. The highest simulated precipitation over Manaus was seen in 48 h lead time simulation with the values between 10 mm day^{-1} and 20 mm day^{-1}.

Figure 4.23: Daily accumulated precipitation (mm day^{-1}) for 0000 UTC 17 November 2016 for: (a) South America (60°S – 20°N, 90°W – 30°W) and (b) Central Amazon (10°S – 5°N, 70°W – 50°W). Plots from left to right represent the simulations by GEF with the lead time of: (a) 72 h, (b) 48 h, (c) 24 h and (d) corresponding CMORPH precipitation data, respectively. The black square in the middle of the lower plots (3.5°S – 2.5°S, 60.5°W – 59.5°W) represents the area that surrounds the city of Manaus (3.1190°S, 60.0217°W), which is positioned approximately in the center of that square.

4.6 Chapter conclusions

In the previous sections, the newly configured high-resolution version of GEF was evaluated at various space scales, starting from the analysis of different variables at different pressure levels at global scale, over the statistical analysis for the region of South America, to the analysis of simulations of locally intense precipitation episodes in the tropical environment. The analysis of the atmospheric variables used in section 3 demonstrated the ability of the model to simulate well the large-scale patterns for the period of up to 7 days. That was the limit in the case of most evaluated variables, where the solutions provided by the model started to become more different in intensity and positions of the minima and maxima when compared against reanalysis. In addition, most of the curves that represent the time series of global mean variables start to diverge from the appropriate solutions from reanalysis also after day 7. In the terms of spatial correlation, most of the variables start with the values higher than 0.8 after day 1, with the best performance shown for the geopotential height at 500 hPa and temperature at 850 hPa that maintain the values over 0.85 even after day 10. For all comparisons presented in section 3, the data from reanalysis were interpolated to the higher resolution of the model, that penalized the model in this evaluation. In order to quantify the difference between the model and reanalysis for the presented variables, RMSE for an ensemble of all 22 integrations is used, but only for South America. The obtained results were within the range of the values of most of the other models used by the CPTEC group for evaluation of the models. As previously mentioned, the RMSE calculations for these models were performed under different conditions and the data obtained have served only to provide the referential values. For the full comparison, GEF would have to be integrated daily for the period of 7 days during the period of at least one month. Two categorical scores are used for the evaluation of precipitation over South America. The ETS showed that the model simulates well the areas with precipitation, with the values even superior than all referential values from CPTEC's regional and global models, however for the

higher precipitation thresholds, the results were on the lower limit of referential values of the other models or even below. Unlike the pattern observed in the other evaluated models, where BIAS has the values mostly over 1 for the light rain, approximately 1 for moderate rain and below 1 for heavy rain, the BIAS of GEF showed the "perfect" score for the lowest, "rain-no rain", threshold and the ratio between the simulated and observed events drops rapidly starting already from the case of light rain. One point that should be noted is that the calculation of BIAS and ETS in the case of GEF is performed in all grid boxes at high resolution making these results more reliable. Time series of the daily mean precipitation over the 4 regions of Brazil showed that the model has skill to accurately simulate the minima and maxima of precipitation in a medium-range scale. This feature of the model could be important for the society and could bring benefits in agriculture, hydrology and in water resource management, in general. However, further evaluations and adjustments are needed, especially for this case and the case of analysis of large-scale patterns, where the presented conclusions are based on one integration of the model only. The global pattern of precipitation, shown in the last section, mostly confirmed the conclusions obtained from categorical evaluation for South America, that the model simulated well the areas with precipitation. Focusing on South America, detailed analysis of precipitation field for 8 selected cases revealed that the model mostly performed well in simulating the spatial distribution of precipitation over the continent. In the terms of intensity, it performed well only in extratropical regions while the precipitation in tropical regions was mostly underestimated. Finally, the model simulated rain for Manaus in almost every presented simulation, with underestimated values in most of the cases. Closer look to the region of Central Amazon showed the good simulation of the areas with precipitation, but also low skill in simulation of the positions of precipitation maxima. In one of the described cases, the differences in measurements from 3 different weather stations in the city of Manaus demonstrated the local character of the event. Even if some sensitivity tests were performed in the initial phase of configuration of the model, further adjustments in

parameterization schemes of the model are needed, especially for convection. The function dependent on horizontal resolution (GOMES; CHOU, 2010) is used in the Kain-Fritsch convective scheme to reduce the positive bias in precipitation in the regional Eta model, but it did not give the expected results in GEF. One of the possible solutions would be to readapt it and reconsider its use in order to improve the precipitation in GEF. The question of the quality of the CMORPH data would not change the conclusions, but should be considered, due to the observed differences with the data from the weather stations. In some of the cases, it might be attributed to the different hour of the performed measurements, but one should take in consideration that CMORPH data are initially obtained in resolution of approximately 12-15 km and further interpolated to the 8 km grid (JOYCE et al., 2004), therefore it may not be suitable for use in analysis of locally extreme events. All shown figures of precipitation suggest that the model underestimates the precipitation, which opposes to the figure that shows the time series of global mean precipitation, and where it is shown that the model in fact overestimates the precipitation. A possible explanation may be in eventually high overestimation of the maxima simulated by the model. Inappropriate distribution of the intensity of precipitation, and continuous increase of the global mean precipitation after day 5, represent the main issues to be investigated in the future improvement of the model.

5 SUMMARY AND CONCLUSIONS

GEF is a global atmospheric model on quasi-uniform cubed-sphere grid that uses the numerical infrastructure of the regional Eta model. Due to its computational efficiency in running on massively parallel computers, it is expected to be a good candidate in further development toward unified model for weather and climate predictions. Two configurations of the model, one at 25-km horizontal resolution for seasonal integrations and other at 8-km horizontal resolution for medium-range integrations are configured and evaluated in this thesis.

GEF at 25-km horizontal resolution is used for comparative assessment of simulated and observed seasonal conditions for the trimester SON of the years 2011 and 2013 with emphasis on the evaluation of the model skill to simulate the onset of the rainy season in the region of WCB. For that purpose, the methods based on pentads of precipitation and OLR were applied. A total of 10 seasonal integrations were performed, for the range of approximately 4 months, creating ensembles of 5 members for each season. The same set of integrations was used to assess the ability of GEF to accurately simulate diurnal cycle of precipitation over South America.

Large-scale pattern is mostly well represented by the model for both years with high level of spatial correlation between the model and reanalysis for almost all analyzed variables, with slightly lower values for precipitation only. Intensity of almost all variables is comparable with reanalysis, mostly with some local differences. Precipitation over some tropical oceanic regions is mostly overestimated and over tropical continental regions is mostly underestimated. For South America, the ensemble mean of precipitation shows good agreement with observation, however, with underestimated values over the tropics.

The model skill to simulate the onset of the rainy season is evaluated in comparative analysis of pentads of precipitation and OLR against the corresponding observed data. The simulated ensemble mean precipitation shows good skill in predicting maxima while the intensity of precipitation in the

same case rather shows continuous increase along the observed period than an abrupt change in regime during transition period from dry to wet season. The simulated ensemble mean OLR is represented by a smooth curve, without clear signs of maxima and minima. However, it represents well the tendency and mostly shows similar pattern as the observed OLR, with mostly overestimated values, especially in 2013. The model skill to simulate onset of the rainy season in WCB has its best demonstration in time-longitude daily averaged precipitation over the latitudes 10°S-20°S. It is clearly shown that with the difference of couple of days when compared against observed data, the model shows transition of precipitation regime from dry to wet, approximately at the end of September, beginning of October. Precipitation pattern changes and more intense precipitation continuously starts to appear after that date, however still significantly less intense than observed.

The diurnal cycle of precipitation in selected area is mostly well represented by the model in the ensemble simulations. The exception is the region of central and northern Argentina and Paraguay where the nocturnal peaks attributed to MCCs are not simulated well by the model.

GEF at 8-km horizontal resolution is integrated for the period of 10 days with 22 different sets of initial conditions. Comparative assessment of simulated global atmospheric fields against the corresponding reanalyses fields for the integration days 1, 3, 5, 7 and 10 in a case study approach, using only one selected integration of the model, demonstrated the ability of the model to simulate well the large-scale patterns for the period of up to 7 days. That was the limit in the case of most evaluated variables, after which the solutions provided by the model started to become more different in intensity and positions of the minima and maxima when compared with reanalysis.

In order to quantify the difference between the model and reanalysis data, RMSE for an ensemble of all 22 integrations is used, but only for South America. The obtained results are within the range of the values of most of the other models used by the CPTEC group for evaluation of the models. For the quantitative evaluation of precipitation, ETS and BIAS are calculated for the

forecast time ranges of 36 and 60 hours, and for the 22 integrations. The ETS shows that the model simulates well the areas with precipitation, with the values even superior than all referential values from CPTEC's regional and global models, however for the higher precipitation thresholds, the results are on the lower limit of referential values of the other models or even below. BIAS shows almost the "perfect" score for the lowest, "rain-no rain", threshold and the ratio between the simulated and observed events drops rapidly starting already from the light rain threshold. For calculation of BIAS and ETS, CMORPH observed data are used and calculations are made in every grid box, making these results more reliable.

In the last section, the simulations of precipitation over South America with the lead times of 24, 48 and 72 hours are compared against appropriate observations with objective to evaluate the model skill to simulate 8 events of extreme precipitation over the city of Manaus. The areas with precipitation over South America are well simulated by the model, which is in agreement with conclusions obtained from categorical analysis. In the terms of intensity, the model performed well in extratropical regions while the precipitation in tropical regions was mostly underestimated. Finally, the model simulated rain for Manaus in almost every presented simulation, with underestimated values in most of the cases. However, in the region of Central Amazon, the model simulates well the areas with precipitation, but also shows low skill in simulation of the positions of precipitation maxima.

The simulations of the model at 25-km horizontal resolution, with time step of 40 s, 38 vertical levels and the model top at 25 hPa were performed with relatively modest use of computational resources, using 600 processor cores, where 1 day of simulation was performed in approximately 6 min. On the other hand, the simulations of the model at 8-km horizontal resolution, with time step of 10 s, 38 vertical levels and the model top at 25 hPa were performed using 1176 processor cores, where 1 day of simulation was performed in approximately 1 h 20 min. These results demonstrate computational efficiency of both configurations of the model, especially when compared with current

global atmospheric model, used for weather forecasts at CPTEC (BAM, FIGUEROA et al., 2016), that has 64 vertical levels, runs at 20-km horizontal resolution, uses 4320 processor cores and takes 2 h 15 min for a 1-day forecast.

BAM runs at 20-km horizontal resolution, while the global atmospheric operational model used for long-term simulations (AGCM, latest results presented in CAVALCANTI; RAIA, 2017) runs at approximately 200-km horizontal resolution. Therefore, the results shown in this thesis present a contribution for the centre, also in the terms of improvement in horizontal resolution. However, even if GEF performed reasonably well, both in medium-range and seasonal scales, the presented results indicated that the further improvements are needed. In the model configured at 25-km horizontal resolution, underestimate of precipitation over tropical continental regions, particularly over South America remains one of the main issues, together with the overestimate presented in analysis of OLR. The model configured at 8-km horizontal resolution also showed difficulties in simulation of precipitation, where the main issues are related with continuous increase of global mean precipitation after day 5 and inappropriate distribution of the intensity of precipitation. The implementation of RRTMG radiation parameterization scheme will hopefully improve the simulation of OLR and favor the better representation of radiation and precipitation. Also, further adjustments in parameterization scheme for convection are expected to contribute in improvement in simulation of precipitation.

Incorporation of the refined vertical coordinate that uses "sloping steps" (MESINGER et al., 2012) and development of the nonhydrostatic version of GEF remain as a future task.

REFERENCES

ADAMS, D. K.; SOUZA, E. P.; COSTA, A. A. Convecção úmida na Amazônia: implicações para modelagem numérica. **Revista Brasileira de Meteorologia**, v.24, p. 168-178, 2009.

ADCROFT, A.; CAMPIN, J. M.; HILL, C.; MARSHALL, J. Implementation of an Atmosphere-Ocean General Circulation Model on the expanded spherical cube. **Monthly Weather Review**, v. 132, p. 2845– 2863, 2004.

ARAKAWA, A.; LAMB, V. Computational design of the basic dynamical processes of the UCLA general circulation model. **Methods in computational physics, Advances in Research and Applications**, v.17, p. 173–265, 1977.

BETTS, A. K. A new convective adjustment scheme. Part I: observational and theoretical basis. **Quarterly Journal of the Royal Meteorological Society**, v.112, p. 677–691, 1986.

BETTS, A. K.; MILLER, M. J. A new convective adjustment scheme. Part II: single column tests using GATE wave, BOMEX, ATEX and arctic air-mass data sets. **Quarterly Journal of the Royal Meteorological Society**, v. 112, p. 693–709, 1986. DOI:10.1002/qj.49711247308.

BETTS, A; JAKOBS C. Evaluation of the diurnal cycle of precipitation, surface thermodynamics, and surface fluxes in the ECMWF model using LBA data. **Journal of the Geophysical Research**, v. 107, n.D20, 2002a. DOI:10.1029/ 2001JD000427.

BETTS, A.; JAKOBS, C. Study of diurnal cycle of convective precipitation over Amazonia using a single column model. **Journal of the Geophysical Research**, v. 107, n.D23, 2002b. DOI:10.1029/2001JD002264.

BLACK, T. L. The new NMC mesoscale Eta model: description and forecast examples. **Weather and Forecasting**, v. 9, p. 265–278, 1994.

BOMBARDI, R. J.; CARVALHO, L. M. V. IPCC global coupled model simulations of the South America monsoon system. **Climate Dynamics,** v. 33, p. 893–916, 2009.

BONATTI, J. P. Modelo de Circulação Geral Atmosférico do CPTEC. **Climanálise**, 1996. Available from: http://climanalise.cptec.inpe.br/~rclimanl/boletim/cliesp10a/bonatti.html. Access in: 26 Nov. 2017.

BRUNET, G.; SHAPIRO, M.; HOSKINS, D.; MONCRIEFF, M.; DOLE, R.; KILADIS, G. N.; KIRTMAN, B.; LORENC, A.; MILLS, B.; MORSS, R.; POLAVARAPU, S.; ROGERS, D.; SCHAAKE, J.; SHUKLA, J. Collaboration of the weather and climate communities to advance sub-seasonal to seasonal prediction. **Bulletin of the American Meteorological Society**, v. 91, p. 397–1406, 2010.

CAVALCANTI, I. F. A.; MARENGO, J. A; SATYAMURTY, P.; TROSNIKOV, I.; BONATTI, J.; NOBRE, C. A.; D'ALMEIDA, C.; SAMPAIO, G.; CASTRO, C. A. C.; CAMARGO, H.; SANCHES, M. B. Global climatological features in a simulation using CPTEC/COLA AGCM**. Journal of Climate**, v. 15, p. 2965–2988, 2002.

CAVALCANTI, I. F. A.; RAIA, A. Lifecycle of South American monsoon system simulated by CPTEC/INPE AGCM. **International Journal of Climatology**, v.37, p. 878–896, 2017. DOI: 10.1002/joc.5044.

CHEN, Y.; RANDERSON, J. T.; MORTON, D. C.; DEFRIES, R. S.; COLLATZ, G. J.; KASIBHATLA, P. S.; GIGLIO, L.; JIN, Y.; MARLIER, M. E. Forecasting fire season severity in South America using sea surface temperature anomalies. **Science**, v. 334, n.6057, p. 787–791, 2011. DOI: 10.1126/science.1209472.

CHOU, S. C.; NUNES, A. M. B.; CAVALCANTI, I. F. A. Extended range forecasts over South America using the regional Eta model. **Journal of the Geophysical Research**, v. 105, p. 10147–10160, 2000.

CHOU, S. C.; BUSTAMANTE, J. F.; GOMES, J. L. Evaluation of Eta Model seasonal precipitation forecasts over South America. **Nonlinear Processes in Geophysics**, v. 12, p. 537–555, 2005. Available from: https://doi.org/10.5194/npg-12-537-2005.

CHOU, S. C.; MARENGO, J. A.; LYRA, A.; SUEIRO, G.; PESQUERO, J.; ALVES, L. M.; KAY, G.; BETTS, R.; CHAGAS, D.; GOMES, J. L.; BUSTAMANTE, J. F.; TAVARES, P. Downscaling of South America present climate driven by 4-member HadCM3 runs. **Climate Dynamics**, v. 38, p. 635–653, 2005. Available from: https://doi.org/10.1007/s00382-011-1002-8.

CIFELLI, R. L.; CAREY, L.; PETERSEN, W. A.; RUTLEDGE, S. A. An ensemble study of wet season convection in southwest Amazonia: kinematics and implications for diabatic heating. **Journal of Climate**, v. 17, p. 4692-4707, 2004.

COHEN, J. C. P.; DIAS, A. F. S. M.; NOBRE, C. A. Environmental conditions associated with Amazonian squall lines: a case study. **Monthly Weather Review**, v. 123, p. 3163–3174, 1995. DOI:10.1175/1520-0493(1995)123<3163:ECAWAS>2.0.CO;2.

COTTON, W.; ANTHES, R. **Storm and cloud dynamics**. New York: Academic Press, 1989. v. 44, 880p.

DA ROCHA, R. P.; MORALES, C. A.; CUANDRA, S. V.; AMBRIZZI, T. RegCM3 assessment over South America: summer seasonal climatology and precipitation diurnal cycle. **Journal of the Geophysical Research**, v. 114, D10108, 2009. DOI: 10.1029/2008JD010212.

DAVIDSON, E. A.; DE ARAÚJO, A. C.; ARTAXO, P.; BALCH, J. K.; BROWN, I. F.; BUSTAMANTE, C.; COE, M. T.; DEFRIES, R. S.; KELLER, M.; LONGO, M.; MUNGER, J. W.; SCHROEDER, W.; SOARES-FILHO, B. S.; SOUZA, C. M.; wofsy, S. C. The Amazon basin in transition. **Nature**, v. 481, n.7381, p. 321–328, 2012. DOI: 10.1038/nature10717.

DAVIES, T.; CULLEN, M. J. P.; MALCOLM, A. J.; MAWSON, M. H.; STANIFORTH, A.; WHITE, A. A.; WOOD, N. A new dynamical core for the Met Office's global and regional modelling of the atmosphere. **Quarterly Journal of the Royal Meteorological Society**, v. 131, n.608, p. 1759–1782, 2005.

DEE, D. P.; UPPALA, S. M.; SIMMONS, A. J.; BERRISFORD, P.; POLI, P; KOBAYASHI, S; ANDRAE, U.; BALMASEDA, M. A.; BALSAMO, G.; BAUER, P.; BECHTOLD, P.; BELJAARS, A. C. M.; VAN DE BERG, L.; BIDLOT, J.; BORMANN, N.; DELSOL, C.; DRAGANI, R.; FUENTES, M.; GEER, A. J.; HAIMBERGER, L.; HEALY, S. B.; HERSBACH, H.; HÓLM, E. V.; ISAKSEN, L.; KÅLLBERG, P.; KÖHLER, M.; MATRICARDI, M.; MCNALLY, A. P.; MONGE-SANZ, B. M.; MORCRETT, J.-J.; PARK, B.-K.; PEUBEY, C.; DE ROSNAY, P.; TAVOLATO, C.; THÉPAUT, J.-N.; VITART, F. The ERA-Interim reanalysis: configuration and performance of thedata assimilation system. **Quarterly Journal of the Royal Meteorological Society**, v. 137, p. 553–597, 2011. Available from: https://doi.org/10.1002/qj.828.

DOI, T.; VECCHI, G. A.; ROSATI, A. J.; DELWORTH, T. L. Biases in the Atlantic ITCZ in seasonal-interannual variations for a coarse and a high resolution coupled climate model. **Journal of Climate**, v.25, p.5494-5511, 2012. DOI: 10.1175/jcli-d-11-00360.1.

DONNER, L.; PHILLIPS, V. Boundary layer control on convective available potential energy: Implications for cumulus parameterization. **Journal of the Geophysical Research**, v. 108, n.D22, 2003. DOI:10.1029/2003JD003773.

DUDHIA, J.; BRESCH, J. F. A global version of the PSU-NCAR mesoscale model. **Monthly Weather Review**, v. 130, p. 2989-3007, 2002.

DUFFY, P.; GOVINDASAMY, B.; IORIO, J.; MILOVICH, J.; SPERBER, K.; TAYLOR, K.; WEHNER, M.; THOMPSON, S. High-resolution simulations of global climate, Part 1: present climate. **Climate Dynamics**, v. 21, n.5/6, p. 371–390, 2003.

EK, M.; MITCHELL, K. E.; LIN, Y.; ROGERS, E.; GRUNMANN, P.; KOREN, V.; GAYNO, G.; TARPLEY, J. D. Implementation of Noah land-surface model advances in the NCEP operational mesoscale Eta model. **Journal of the Geophysical Research**, v. 108, p. 8851, 2003. DOI:10.1029/2002JD003296.

ELIASEN, E.; MACHENHAUER, B.; RASMUSSEN, E. **On a numerical method for integration of the hydrodynamical equations with a spectral representation of the horizontal fields**. København: Institute for Teoretisk Meteorologi, University of Copenhagen, 1970.

ESPINOZA, J. C.; RONCHAIL, J.; FRAPPART, F.; LAVADO, W.; SANTINI, W.; GUYOT, J. L. The major floods in the Amazonas river and tributaries (Western Amazon Basin) during the 1970-2012 period: a focus on the 2012 flood. **Journal of Hydrology**, v. 14, p. 1000- 1008, 2012.

FERRIER, B. S.; JIN, Y.; LIN, Y.; BLACK, T.; ROGERS, E.; DIMEGO, G. Implementation of a new grid-scale cloud and precipitation scheme in the NCEP Eta Model. In: CONFERENCE ON WEATHER ANALYSIS AND FORECASTING/15TH CONFERENCE ON NUMERICAL WEATHER PREDICTION, 19., 2002. San Antonio. **Proceedings…** American Meteorological Society, 2002. p. 280–283.

FIGUEROA, S. N.; NOBRE, C. A. Precipitation distribution over central and western tropical South America. **Climanálise**, v. 5, p. 25–40, 1990.

FIGUEROA, S. N.; BONATTI, J. P.; KUBOTA, P. Y.; GRELL, G. A.; MORRISON, H.; BARROS, S. R. M.; FERNANDEZ, J. P. R.; RAMIREZ, E.; SIQUEIRA, L.; LUZIA, G.; SILVA, J.; SILVA, J. R.; PENDAHARKAR, J.; capistrano, V. B.; ALVIM, D. S.; ENORÉ, D. P.; DINIZ, F. L. R.; SATYAMURTY, P.; CAVALCANTI, I. F. A.; NOBRE, P.; BARBOSA, H. M. J.; MENDES, C. L.; PANETTA, J. The Brazilian global atmospheric model (BAM): performance for tropical rainfall forecasting and sensitivity to convective scheme and horizontal resolution. **Weather Forecast**, v. 31, p. 1547–1572, 2016.

FOURNIER, A.; TAYLOR, M. A.; TRIBBIA, J. The spectral element atmosphere model (SEAM): high-resolution parallel computation and localized resolution of regional dynamics. **Monthly Weather Review**, v. 132, n.3, p. 726–748, 2004.

FRITSCH, J. M.; CHAPPELL, C. F. Numerical prediction of convectively driven mesoscale pressure systems. Part I: convective parameterization. **Journal of the Atmospheric Sciences**, v. 37, p. 1722-1733, 1980.

FU, R.; Zhu, B.; DICKINSON, R. How do atmosphere and land surface influence seasonal changes of convection in the tropical Amazon. **Journal of Climate**, v. 12, p.1306-1321, 1999.

FU, R.; LI, W. The influence of the land surface on the transition from dry to wet season in Amazonia. **Theoretical and Applied Climatology**, v. 78, p. 97–110, 2004. DOI: 10.1007/s00704-004-0046-7.

GAN, M. A.; KOUSKY, V. E.; ROPELEWSKI, C. F. The South America monsoon circulation and its relationship to rainfall over West-Central Brazil. **Journal of Climate**, v. 17, p. 47–66, 2004.

GAN, M. A.; RAO, V. B.; MOSCATI, M. C. L. South American monsoon indices. **Atmospheric Science Letters**, v. 6, p. 219–223, 2006.

GARREAUD, R. D.; WALLACE, J. M. The diurnal of convective cloudiness over the Americas. **Monthly Weather Review**, v. 125 p. 3157–3171, 1997. DOI:10.1175/1520 0493(1997)125<3157:TDMOCC>2.0.CO;2.

GARCIA, S. R.; KAYANO, M. T. Determination of the onset dates of the rainy season in central Amazon with equatorially antisymmetric outgoing longwave radiation. **Theoretical and Applied Climatology**, v. 97, p. 361–372, 2009.

GARCIA, S. R.; KAYANO, M. T. Moisture and heat budgets associated with the South American monsoon system and the Atlantic ITCZ. **International Journal of Climatology**, v. 31, p. 2154–2167, 2011.

GARSTANG, M.; ULANSKI, S.; GRECO, S.; SCALA, J.; SWAP, J.; FITZJARRALD, D.; MARTIN, D.; BROWELL, E.; SHIPMAN, M.; CONNORS, V.; HARRIS, R.; TALBOT, R. The Amazon Boundary Layer Experiment (ABLE 2B): a meteorological perspective. **Bulletin of the American Meteorological Society**, v. 71, p.19-32, 1990.

GARSTANG, M.; MASSIE, H. L. JR.; HALVERSON, J.; GRECO, S.; SCALA, J.

Amazon coastal squall lines. Part I: structure and kinematics. **Monthly Weather Review**, v. 122, p. 608 – 622, 1994.

GASSMANN, A. Non-hydrostatic modelling with the ICON model. In: ECMWF NON-HYDROSTATIC WORKSHOP, 2010. **Proceedings…** 2010. Available from: https://www.ecmwf.int/sites/default/files/elibrary/2011/9501-non-hydrostatic-modelling-icon.pdf

GEIST, H. **Our Earth's changing land:** an encyclopedia of land-use and land-cover change. Westport: Greenwood, 2005.

GERARD, L. An integrated package for subgrid convection, clouds and precipitation compatible with meso-gamma scales. **Quarterly Journal of the Royal Meteorological Society**, v. 133, p. 711–730, 2007.

GIRALDO, F. X. A spectral element shallow water model on spherical geodesic grids. **International Journal for Numericl Methods in Fluids**, v. 35, p. 869–901, 2001.

GIRALDO, F. X.; ROSMOND, T. E. A Scalable Spectral Element Eulerian Atmospheric Model (SEE-AM) for NWP: dynamical core tests. **Monthly Weather Review**, v. 132, p. 133–153, 2004.

GONZALEZ, M.; VERA, C. S.; LIEBMANN, B.; MARENGO, J.; Kousky, V.; ALLURED, D. The nature of the rainfall onset over central South America. **Atmosfera**, v. 20, p. 377–394, 2007.

GOVETT, M. W.; MIDDLECOFF, J.; HENDERSON, T. Running the NIM next-generation weather model on GPUs. In: IEEE INTERNATIONAL SYMPOSIUM ON CLUSTER COMPUTING AND THE GRID, 2010, Melbourne, Australia. **Proceedings…** IEEE, 2010. p. 792–796.

GRECO, S.; SWAP, R.; GARSTANG, M.; ULANSKI, S.; SHIPHAM, M.; HARRISS, R. C.; TALBOT, R.; ANDREAE, M. O.; ARTAXO, P. Rainfall and surface kinematics conditions over central Amazonia during ABLE 2B. **Journal of the Geophysical Research**, v. 95, p.17001-17014, 1990.

HALVERSON, J. B.; RICKENBACH, T.; ROY, B., PIERCE, H.; WILLIAMS, E. Environmental characteristics of convective systems during TRMM-LBA. **Monthly Weather Review**, v. 130, p.1493-1509, 2002.

HAZELEGER, W.*;* SEVERIJNS, C.*;* SEMMLER, T.; STEFANESCU, S.; YANG, S.; WANG, X.; WYSER, K.; DUTRA, E.; BALDASANO, J. M.; BINTANJA, R.; BOUGEAULT, P.; CABALLERO, R.; EKMAN, A. M. L.; CHRISTENSEN, J. H.; VAN DEN HURK, B.; JIMENEZ, P.; JONES, C.; KALLBERG, P.; KOENIGK, T.; MCGRATH, R.; MIRANDA, P.; VAN NOIJE, T.; PALMER, T.; PARODI, J. A.; SCHMITH, T.; SELTEN, F.; STORELVMO, T.; STERL, A.; TAPAMO, H.; VANCOPPENOLLE, M.; VITERBO, P.; WILLÉN, U. EC-Earth: A seamless Earth-system prediction approach in action. **Bulletin of the American Meteorological Society,** v. 91, p. 1357-1363, 2010.

HOREL, J. D.; HAHMANN, A. N.; GEISLER, J. E. An investigation of the annual cycle of convective activity over tropical Americas. **Journal of Climate**, v. 2, n.11, p. 1388-1403, 1989.

HURRELL, J. W.; MEEHL, G. A.; BADER, D.; DELWORTH, T.; KIRTMAN, B.; WIELICKI, B. A unified modeling approach to climate system prediction. **Bulletin of the American Meteorological Society**, v. 90, p. 1819–1832, 2009.

JANJIĆ, Z. I. Pressure gradient force and advection scheme used for forecasting with steep and small scale topography. **Beiträge zur Physik der**

Atmosphäre, v. 50, p. 186–199, 1977.

JANJIĆ, Z. I. Forward-backward scheme modified to prevent two-grid-interval noise and its application in sigma coordinate models. **Beiträge zur Physik der Atmosphäre**, v. 52, p. 69–84, 1979.

JANJIĆ, Z. I. Nonlinear advection schemes and energy cascade on semi-staggered grids. **Monthly Weather Review**, v. 112, p. 1234–1245, 1984.

JANJIĆ, Z. I. The step-mountain coordinate: physical package. **Monthly Weather Review**, v. 118, p. 1429–1443, 1990.

JANJIĆ, Z. I. The step-mountain eta coordinate model: further developments of the convection, viscous sublayer, and turbulence closure schemes. **Monthly Weather Review**, v. 122, p. 927–945, 1994.

JANJIĆ, Z. I.; GERRITY, J. P., JR.; NIČKOVIĆ, S. An alternative approach to nonhydrostatic modeling. **Monthly Weather Review**, v. 129, p. 1164–1178, 2001.

JONES, C.; CARVALHO, L. M. V. Climate change in the South American monsoon system: present climate and CMIP5 projections. **Journal of Climate**, v. 26, p. 6660–6678, 2013.

JOYCE, R. J.; JANOWIAK, J. E.; ARKIN, P. A.; XIE, P. CMORPH: A method that produces global precipitation estimates from data at high spatial and temporal resolution. **Journal of Hydrometeorology**, v. 5, p. 487-503, 2004.

KAIN, J. S.; FRITSCH, J. M. A one-dimensional entraining/detraining plume model and its application in convective parameterization. **Journal of the Atmospheric Sciences**, v. 47, n.23, p. 2784-2802, 1990.

KAIN, J. S. The Kain−Fritsch convective parameterization: an update. **Journal of Applied Meteorology**, v. 43, p. 170−181, 2004.

KALNAY, E.; KANAMITSU, M.; KISTLER, R.; COLLINS, W.; DEAVEN, D.; GANDIN, L.; IREDELL, M.; SAHA, S.; WHITE, G.; WOOLLEN, J.; ZHU, Y.; LEETMAA, A.; REYNOLDS, R.; CHELLIAH, M.; EBISUZAKI, W.; HIGGINS, W.; JANOWIAK, J.; MO, K. C.; ROPELEWSKI, C.; WANG, J.; JENNE, R.; JOSEPH, D. The NCEP/NCAR 40-year reanalysis project. **Bulletin of the American Meteorological Society**, v. 77, p. 437-470, 1996.

KANAMITSU, M.; EBISUZAKI, W.; WOOLLEN, J.; YANG, S.-K.; HNILLO, J. J.; FIORINO, M.; POTTER, G. L. NCEP-DOE AMIP-II Reanalysis (R-2). **Bulletin of the American Meteorological Society**, p. 1631-1643, 2002.

KHARIN, V.; ZWIERS, F.; ZHANG, X.; HEGERL, G. Changes in temperature and precipitation extremes in the IPCC ensemble of global coupled model simulations. **Journal of Climate**, v. 20, n.8, p. 1419–1444, 2007.

KOUSKY, E. V. Diurnal rainfall variation in northeast Brazil. **Monthly Weather Review**, v. 108, p. 488–498, 1980. DOI:10.1175/1520-0493(1980)108<0488:DRVINB>2.0.CO;2.

KOUSKY, V. E. Pentad outgoing longwave radiation climatology for the South American sector. **Revista Brasileira de Meteorologia**, v. 3, p. 217–231, 1988.

LACIS, A. A.; HANSEN, J. E. A parameterization of the absorption of solar radiation in the Earth's atmosphere. **Journal of the Atmospheric Sciences**, v. 31, p. 118-133, 1974.

LATINOVIĆ, D.; CHOU, S. C.; NOBRE, P. Capability of Global Eta Framework

(GEF) to predict extreme climate events. In: SIMPÓSIO INTERNACIONAL DE CLIMATOLOGIA (SIC), 5., 2013, Florianópolis, SC, Brazil. **Anais…** 2013.

LATINOVIĆ, D.; CHOU, S. C.; RANČIĆ, M. Seasonal range test run with Global Eta Framework. **Advances in Science and Research**, v. 14, p. 247-251, 2017. Available from: https://doi.org/10.5194/asr-14-247-2017.

LAURENT, H.; MACHADO, L. A. T.; MORALES, C. A.; DURIEUX, L. Characteristics of the Amazonian mesoscale convective systems observed from satellite and radar during the WETAMC/LBA experiment. **Journal of the Geophysical Research**, v. 107, p. 8064, 2002. DOI:10.1029/ 2001JD000337.

LEAN, H. W.; CLARK, P. A.; DIXON, M.; ROBERTS, N. M.; FITCH, A.; FORBES, R.; HALLIWELL, C. Characteristics of high-resolution versions of the Met Office Unified Model for forecasting convection over the United Kingdom. **Monthly Weather Review**, v. 136, p. 3408–3424, 2008.

LEE, J.-E.; LINTNER, B. R.; BOYCE, C. K.; LAWRENCE, P. J. Land use change exacerbates tropical South American drought by sea surface temperature variability. **Geophysical Research Letters**, v. 38, n.19, 2011. DOI: 10.1029/2011gl049066.

LIEBMANN, B.; MARENGO, J. Interannual variability of the rainy season and rainfall in the Brazilian Amazon Basin. **Journal of Climate**, v. 14, p. 4308–4318, 2001.

LIEBMANN, B.; CAMARGO, S. J.; SETH, A.; MARENGO, J. A.; CARVALHO, L. M.; ALLURED, D.; FU, R.; VERA, C. S. Onset and end of the rainy season in South America in observations and the ECHAM 4.5 atmospheric general circulation model. **Journal of Climate**, v. 20, p. 2037–2050, 2007.

LIN, X.; RANDALL, D.; FOWLER, L. Diurnal variability of the hydrological cycle and radiative fluxes: comparisons between observations and a GCM. **Journal of Climate**, v. 13, p. 4159-4179, 2000.

LYRA, A; TAVARES, P.; CHOU, S. C.; SUEIRO, G.; DERECZYNSKI, C.; SONDERMANN, M.; SILVA, A.; MARENGO, J.; GIAROLLA, A. Climate change projections over three metropolitan regions in Southeast Brazil using the non-hydrostatic Eta regional climate model at 5-km resolution. **Theoretical and Applied Climatology**, 2017. Available from: https://doi.org/10.1007/s00704-017-2067-z.

MACHADO, L.; LAURENT, H.; LIMA, A. Diurnal march of the convection observed during TRMM-WETAMC/LBA. **Journal of the Geophysical Research**, v. 107, p. 8064, 2002. DOI:10.1029/2001JD000338.

MALHI, Y.; WRIGHT, J. Spatial patterns and recent trends in the climate of tropical rainforest regions. **Philosophical Transactions of the Royal Society London B: Biological Sciences**, v. 359, n.1443, p. 311–329, 2004.

MAPES, B. Convective inhibition, subgrid-scale triggering energy, and stratiform instability in a toy tropical wave model. **Journal of the Atmospheric Sciences**, v. 57, p. 1515-1535, 2000.

MARENGO, J. A. Interannual variability of deep convection in the tropical South American sector as deduced from ISCCP C2 data. **International Journal of Climatology**, v. 15, n.9, p. 995-1010, 1995.

MARENGO, J. A. Impactos de extremos relacionados com o tempo e o clima: impactos sociais e econômicos. **Boletim do Grupo de Pesquisa em Mudanças Climáticas**, v. 8, p. 1-5, 2009.

MARENGO, J. A.; LIEBMANN, B.; KOUSKY, V. E.; FILIZOLA, N.; WAINER I. On the onset and end of the rainy season in the Brazilian Amazon Basin. **Journal of Climate**, v. 14, p. 833–852, 2001.

MARENGO, J. A.; LIEBMANN, B.; GRIMM, A. M.; MISRA, V.; SILVA DIAS, P. L.; CAVALCANTI, I. F. A.; CARVALHO, L. M. V.; BERBERY, E. H.; AMBRIZZI, T.; VERA, C. S.; SAULO, A. C.; NOGUES-PAEGLE, J.; ZIPSER, E.; SETH, A.; ALVES, L. M. Recent developments on the South American monsoon system. **International Journal of Climatology**, v. 32, p. 1–21, 2012. DOI:10.1002/joc.2254.

MARENGO, J. A.; TOMASELLA, J.; SOARES, W. R. Extreme climate events in the Amazon Basin. **Theoretical and Applied Climatology**, v. 107, p. 73-85, 2012. Available from: http://dx.doi.org/10.1007/s00704-011-0465-1.

MAJEWSKI, D.; LIERMANN, D.; PROHL, P.; RITTER, B.; BUCHHOLD, M.; HANISCH, T.; PAUL, G.; WERGEN, W.; BAUMGARDNER, J. The operational global icosahedral-hexagonal gridpoint model GME: description and high-resolution tests. **Monthly Weather Review**, v. 130, p. 319–338, 2002.

MASUDA, Y.; OHNISHI, H. An integration scheme of the primitive equations model with an icosahedral–hexagonal grid system and its application to the shallow water equations. In: SYMPOSIUM ON SHORT- AND MEDIUM-RANGE NUMERICAL WEATHER PREDICTION, 1986, Tokyo, Japan. **Proceedings…** Tokyo: Japan Meteorological Society, 1986. p. 317–326.

MCGREGOR, J. L. Semi-lagrangian advection on conformal-cubic grids. **Monthly Weather Review**, v. 124, p. 1311–1322, 1996.

MCGREGOR, J. L. Semi-lagrangian advection on a cubic gnomonic projection of the sphere. In: LIN, C. A.; LAPRISE, R.; RITCHIE, H. (Eds.). **Numerical**

methods in atmospheric and oceanic modelling. Washington: NRC
Research Press, 1997. p. 153–169.

MCGREGOR, J. L.; DIX, M. R. The CSIRO conformal-cubic atmospheric GCM.
In: HODNETT, P. F. (Ed.). **IUTAM Symposium on Advances in Mathematical
Modelling of atmosphere and ocean dynamics**. Berlin: Springer, 2001. p.
197–202.

McHALE, J. **R. Buckminster fuller**: makers of contemporary architecture. New
York: LLC, 1962. 128p.

MELLOR, G. L.; YAMADA, T. Development of a turbulence closure model for
geophysical fluid problems. **Reviews of Geophysics and Space Physics**, v.20,
p. 851–875, 1982.

MESINGER, F. A method for construction of second-order accuracy difference
schemes permitting no false two-grid-interval wave in the height field. **Tellus**,
v.25, p. 444–458, 1973.

MESINGER, F. Forward-backward scheme, and its use in a limited area model.
Beiträge zur Physik der Atmosphäre, v. 50, p. 200–210, 1977.

MESINGER, F. Blocking technique for representation of mountains in
atmospheric models. **Revista di Meteorologia Aeronáutica**, v. 44, p. 195–202,
1984.

MESINGER, F. Improvements in quantitative precipitation forecasts with the Eta
regional model at the National Centers for Environmental Prediction: the 48-km
upgrade. **Bulletin of the American Meteorological Society**, v. 77, p. 2637–
2649, 1996.

MESINGER, F.; BLACK, T. L. On the impact on forecast accuracy of the step-mountain (Eta) vs. sigma coordinate. **Meteorology and Atmospheric Physics**, v. 50, p. 47–60, 1992. Available from: https://doi.org/10.1007/BF01025504.

MESINGER, F.; JANJIĆ, Z. I. Problems and numerical methods of the incorporation of mountains in atmospheric models. **Lectures in Applied Mathematics**, v. 22, p. 81–120, 1985.

MESINGER, F.; JANJIĆ, Z. I.; NIČKOVIĆ, S.; GAVRILOV, D.; DEAVEN, D. G. The step mountain coordinate: model description and performance for cases of Alpine cyclogenesis and for a case of an Appalachian redevelopment. **Monthly Weather Review**, v. 116, p. 1493–1518, 1988.

MESINGER, F.; JOVIC, D. **The Eta slope adjustment**: contender for an optimal steepening in a piecewise-linear advection scheme? comparison tests. 2002. Available from: http://www.emc.ncep.noaa.gov/officenotes/newernotes/on439.pdf. Access in: 26 Nov. 2017.

MESINGER, F.; CHOU, S. C.; GOMES, J. L.; JOVIC, D.; BASTOS, P.; BUSTAMANTE, J. F.; LAZIC, L.; LYRA, A. A.; MORELLI, S.; RISTIC, I.; VELJOVIC, K. An upgraded version of the Eta model. **Meteorology and Atmospheric Physics**, v. 116, p. 63–79, 2012. Available from: https://doi.org/10.1007/s00703-012-0182-z.

MESINGER, F.; VELJOVIC, K. Eta vs sigma: review of past results, Gallus–Klemp test, and large-scale wind skill in ensemble experiments. **Meteorology and Atmospheric Physics**, v.129, n.6, p.573-593, 2017. Available from: https://doi.org/10.1007/s00703-016-0496-3.

MOLION, L. C. B. Climatologia dinâmica da região Amazônica: mecanismos de

precipitação. **Revista Brasileira de Meteorologia**, v. 2, n.1, p. 107-117, 1987.

MOLION, L. C. B. Amazonia rainfall and its variability. In: BONELL, M.;
HUFSCHMIDT, M. M.; GLADWELL, J. S. (Eds.). **Hydrology and water
management in the humid tropics**. Cambridge: Cambrigde University Press,
1993. p. 99-111.

NEPSTAD, D. C.; VERSSIMO, A.; ALENCAR, A.; NOBRE, C.; LIMA, E.;
LEFEBVRE, P.; SCHLESINGER, P.; POTTER, C.; MOUTIMHO, P.; MENDOZA,
E.; COCHRANE, M.; BROOKS, V. Large-scale impoverishment of Amazonian
forests by logging and fire. **Nature**, v. 398, n.6727, p. 505–508, 1999.

NICOLINI, M.; SAULO, A. C. Modeled Chaco low-level jets and related
precipitation patterns during the 1997–1998 warm season. **Meteorology and
Atmospheric Physics**, v. 94, p. 129–143, 2006. DOI:10.1007/s00703-006-
0186-7.

NOBRE, C.; BRASSEUR, G. P.; SHAPIRO, M. A.; LAHSEN, M.; BRUNET, G.;
BUSALACCHI, A. J.; HIBBARD, K.; SEITZINGER, S.; NOONE, K.; OMETTO, J.
P. Addressing the complexity of the Earth system. **Bulletin of the American
Meteorological Society**, v. 91, p. 1389–1396, 2010.

NOGUÉS-PAEGLE, J.; MECHOSO, C. R.; FU, R.; BERBERY, E. H.; CHAO, W.
C.; CHEN, T. C.; COOK, K.; DIAZ, A. F.; ENFIELD, D.; FERREIRA, R.; GRIMM,
A. M.; KOUSKY, V.; LIEBMANN, B.; MARENGO, J.; MO, K.; NEELIN, J. D.;
PAEGLE, J.; ROBERTSON, A. W.; SETH, A.; VERA, C. S.; ZHOU, J. Progress
in Pan American CLIVAR research: understanding the South American
monsoon. **Meteorologica**, v. 27, p. 3-32, 2002.

ORSZAG, S. A. Transform method for calculation of vector coupled sums:
application to the spectral form of the vorticity equation. **Journal of the**

Atmospheric Sciences, v. 27, p. 890–895, 1970.

PAULSON, C. A. The mathematical representation of wind speed and temperature profiles in the unstable atmospheric surface layer. **Journal of Applied Meteorology**, v. 9, p. 857–861, 1970.

PESQUERO, J. F.; CHOU, S. C.; NOBRE, C. A.; MARENGO, J. A. Climate downscaling over South America for 1961–1970 using the Eta Model. **Theoretical and Applied Climatology**, v. 99, p. 75–93, 2010. Available from: https://doi.org/10.1007/s00704-009-0123-z.

PETERSEN, W.; RUTLEDGE, S. Regional variability in tropical convection: observations from TRMM. **Journal of Climate**, v. 14, p. 3566-3586, 2001.

PETERSEN, W. A.; NESBITT, S. W.; BLAKESLEE, R. J.; CIFELLI, R.; HEIN, P.; RUTLEDGE, S. A. TRMM observations of intraseasonal variability in convective regimes over the Amazon. **Journal of Climate**, v. 15, p. 1278-1294, 2002.

PETERSEN, W.; FU, R.; CHEN, M.; BLAKESLEE, R. Intraseasonal forcing of convection and lightning activity in the southern Amazon as a function of cross equatorial flow. **Journal of Climate**, v. 19, p. 3180-3196, 2006.

PILOTTO, I. L.; CHOU, S. C.; NOBRE, P. Seasonal climate hindcasts with Eta model nested in CPTEC coupled ocean–atmosphere general circulation model. **Theoretical and Applied Climatology**, v. 110, p. 437–456, 2012. DOI:10.1007/s00704-012- 0633-y.

PLATZMAN, G. W. The spectral form of the vorticity equation. **Journal of Meteorology**, v. 17, p. 635–644, 1960.

POPE, V.; STRATTON, R. The processes governing horizontal resolution sensitivity in a climate model. **Climate Dynamics**, v. 19, n.3, p. 211–236, 2002.

PURSER, J. R.; JANJIĆ, Z. I.; BLACK, T. L. A b-cylindrical "Yin-Yang" global grid geometry applied to the NCEP Nonhydrostatic Mesoscale Model, extended abstract. In: CONFERENCe ON WEATHER ANALYSIS AND FORECASTING, 21., 2005. **Proceedings…** AMS, 2005.

PURSER, R. J.; RANČIĆ M. Smooth quasi-homogeneous gridding of the sphere. **Quarterly Journal of the Royal Meteorological Society**, v. 124, p. 637–647, 1998.

PURSER, R. J.; RANČIĆ, M. **A standardized procedure for the derivation of smooth and partially overset grids on the sphere, associated with polyhedra that admit regular griddings of their surfaces**. Part I: mathematical principles of classification and construction. Silver Spring: NOAA, 2011. (NOAA/NCEP Office Note 467). Available from: http://www.emc.ncep.noaa.gov/officenotes/newernotes/on467.pdf. Access in: 26 Nov. 2017.

PURSER, R. J.; RANČIĆ, M.; JOVIĆ, D.; LATINOVIĆ, D. Two strategies for the mitigation of coordinate singularities of a spherical polyhedral grid. In: PDEs WORKSHOP, 2014, Boulder, CO, USA. **Proceedings…** 2014. Available from: http://www.cgd.ucar.edu/events/20140407/Presentations-Posters/Purser.pdf. Access in: 26 Nov. 2017.

PUTMAN, W. M.; LIN, S.-J. A finite-volume dynamical core on the cubed-sphere grid. In: POGORELOV, N. V.; AUDIT, E.; COLELLA, P.; ZANK, G. P. (Eds.). **Numerical modeling of space plasma flows**: astronum-2008. San Francisco: Astronomical Society of the Pacific, 2009. v. 406, p. 268–276.

PUTMAN, W. M.; SUAREZ, M. Mesoscale weather and climate modeling with the global non-hydrostatic Goddard Earth Observing System Model (GEOS-5) at cloud-permitting resolutions. In: AGU FALL MEETING ABSTRACTS, 2009. **Abstracts…** AGU, 2009.

RAIA, A.; CAVALCANTI, I. F. A. The life cycle of the South American monsoon system. **Journal of Climate**, v. 21, p. 6227–6246, 2008.

RANČIĆ, M.; PURSER, R. J.; MESINGER, F. A global shallow-water model using an expanded spherical cube: gnomonic versus conformal coordinates. **Quarterly Journal of the Royal Meteorological Society**, v. 122, p. 959–982, 1996.

RANČIĆ, M.; ZHANG, H. A framework for globalization of regional atmospheric models: Dry core and quasi-uniform grids. In: CONFERENCE ON NUMERICAL WEATHER PREDICTION, 15., 2002, San Antonio, Texas. **Proceedings…** Boston: American Meteorological Society, 2002.

RANČIĆ, M.; PURSER, R. J.; JOVIĆ, D.; VASIĆ, R.; BLACK, T. A nonhydrostatic multiscale model on the uniform Jacobian cubed sphere. **Monthly Weather Review**, v.145, p.1083-11505, 2017. Available from: https://doi.org/10.1175/MWR-D-16-0178.1.

RAO, V. B.; HADA, K. Characteristics of rainfall over Brazil: annual variations and connections with the Southern Oscillation. **Theoretical and Applied Climatology**, v. 42, p. 81–92, 1990.

RAO, G. V.; CAVALCANTI, I. F. A.; HADA, K. Annual variations of rainfall over Brazil and water vapor characteristics of South America. **Journal of the**

Geophysical Research, v. 101, n.D21, p. 26539–26551, 1996. DOI:10.1029/96JD01936.

RAYMOND, D. Regulation of moist convection over the west Pacific warm pool. **Journal of the Atmospheric Sciences**, v. 52, p. 3945-3959, 1995.

REYNOLDS, R. W.; RAYNER, N. A.; SMITH, T. M.; STOKES, D. C.; WANG, W. An improved in situ and satellite SST analysis for climate. **Journal of Climate**, v. 15, p. 1609-1625, 2002.

RICKENBACH, T. Nocturnal cloud systems and the diurnal variation of clouds and rainfall in Southwestern Amazonia. **Monthly Weather Review**, v. 132. p. 1201-1219, 2004.

RINGLER, T. D.; HEIKES, R. P.; RANDALL, D. A. Modeling the Atmospheric General Circulation using a spherical geodesic grid: a new class of dynamical cores. **Monthly Weather Review**, v. 128, p. 2471–2490, 2000.

ROECKNER, E.; BROKOPF, R.; ESCH, M.; GIORGETTA, M.; HAGEMANN, S.; KORNBLUEH, L.; MANZINI, E.; SCHLESE, U.; SCHULZWEIDA, U. Sensitivity of simulated climate to horizontal and vertical resolution in the ECHAM5 atmosphere model. **Journal of Climate**, v. 19, n.16, p. 3771–3791, 2006.

RONCHI, C.; IACONO, R.; PAOLUCCI, R. The "cubed sphere": a new method for the solution of partial differential equations in spherical geometry. **Journal of Computational Physics**, v. 124, p. 93–114, 1996.

SADOURNY, R. Conservative finite-differencing approximations of the primitive equations on quasi-uniform spherical grids. **Monthly Weather Review**, v. 22, p. 1107–1115, 1972.

SALATHÉ, E. P.; STEED, R.; MASS, C. F.; ZAHN, P. H. A high-resolution climate model for the U.S. Pacific Northwest: mesoscale feedbacks and local responses to climate change. **Journal of Climate**, v. 21, n.21, p. 5708–5726, 2008.

SALIO, P.; NICOLINI, M.; ZIPSER, E. J. Mesoscale convective systems over southeastern South American low-level jet. **Monthly Weather Review**, v. 135, p. 1290–1309, 2007. DOI:10.1175/MWR3305.1.

SATOH, M. Conservative scheme for the compressible non-hydrostatic models with the horizontally explicit and vertically implicit time integration scheme. **Monthly Weather Review**, v. 130, p. 1227–1245, 2002.

SATOH, M. Conservative scheme for a compressible non-hydrostatic models with moist processes. **Monthly Weather Review**, v. 131, p. 1033–1050, 2003.

SATYAMURTY, P.; DA COSTA, C. P.; MANZI, A. O.; CANDIDO, L. A. A quick look at the 2012 record flood in the Amazon Basin. **Geography Research Letter**, v. 40, p. 1-6, 2013. Available from: http://dx.doi.org/10.1002/grl.50245.

SCHWARZKOPF, M. D.; FELS, S. B. The simplified exchange method revisited: an accurate, rapid method for computation of infrared cooling rates and fluxes. **Journal of the Geophysical Research**, v. 96, p. 9075–9096, 1991.

SENIOR, C.A.; ARRIBAS, A.; BROWN, A. R.; CULLEN, M. J. P.; JOHNS, T. C.; MARTIN, G. M.; MILTON, S. F.; WEBSTER, S.; WILLIAMS, K. D. Synergies between numerical weather prediction and general circulation climate models. In: DONNER, L.; SCHUBERT, W.; SOMERVILLE, R. (Eds.). **The development of atmospheric general circulation models**. Cambridge: Cambridge University Press, 2011. p. 76–116.

SETH, A.; RAUSCHER, S.; CAMARGO, S.; QIAN, J.-H.; PAL, J. RegCM regional climatologies for South America using reanalysis and ECHAM model global driving fields. **Climate Dynamics**, v. 28, p. 461, 2006. DOI:10.1007/s00382-006-0191-z.

SETH, A.; ROJAS, M.; RAUSCHER, S. CMIP3 projected changes in the annual cycle of the South American Monsoon. **Climate Change**, v. 98, p. 331–357, 2010.

SHAFFREY, L. C.; STEVENS, I.; NORTON, W.; ROBERTS, M. J.; VIDALE, P. L.; HARLE, J. D.; JRRAR, A.; STEVENS, D. P.; WOODAGE, M. J.; DEMORY, M.-E.; DONNERS, J.; CLARK, D. B.; CLAYTON, A.; COLE, J. W.; WILSON, S. S.; CONNOLLEY, W. M.; DAVIES, T. M.; IWI, A. M.; JOHNS, T. C.; KING, J. C.; NEW, A. L.; SLINGO, J. M.; SLINGO, A.; STEENMAN-CLARK, L.; MARTIN, G. M. U.K. HiGEM: The new U.K. high-resolution global environment model: model description and basic evaluation. **Journal of Climate**, v. 22, n.8, p. 1861-1896, 2009. Available from: https://doi.org/10.1175/2008JCLI2508.1.

SHAPIRO, M.; SHUKLA, J.; BRUNET, G.; NOBRE, C.; BELAND, M.; DOLE, R.; TRENBERTH, K.; ANTHES, R.; ASRAR, G.; BARRIE, L.; BOUGEAULT, P.; BRASSEUR, G.; BURRIDGE, D.; BUSALACCHI, A.; CAUGHEY, J.; CHEN, D. L.; CHURCH, J.; ENOMOTO, T.; HOSKINS, B.; HOV, O.; LAING, A.; LETREUT, H.; MAROTZKE, J.; McBEAN, G.; MEEHL, G.; MILLER, M.; MILLS, B.; MITCHELL, J.; MONCRIEFF, M.; NAKAZAWA T.; OLAFSSON, H.; PALMER, T.; PARSONS, D.; ROGERS, D.; SIMMON, A.; TROCCOLI A.; TOTH, Z.; UCCELLINI, L.; VELDEN, C.; WALLACE, J. M. An earth-system prediction initiative for the twenty-first century. **Bulletin of the American Meteorological Society**, v. 91, p. 1377–1388, 2010.

SHIU, C.-J.; LIU, S. C.; FU, C.; DAI, A.; SUN, Y. How much do precipitation extremes change in a warming climate? **Geophysical Research Letters**, v. 39,

L17707, 2012. DOI:10.1029/2012GL052762.

SILBERMAN, I. Planetary waves in the atmosphere. **Journal of Meteorology**, v. 11, p. 27–34, 1954.

SILLMANN, J.; KHARIN, V. V.; ZHANG, X.; ZWIERS, F. W.; BRONAUGH, D. Climate extremes indices in the CMIP5 multimodel ensemble: Part 1. model evaluation in the present climate. **Journal of the Geophysical Research: Atmosphere**, v. 118, p. 1716–1733, 2013. DOI:10.1002/jgrd.50203.

SILVA, A. E.; CARVALHO, L. M. V. Large-scale index for South America Monsoon (LISAM). **Atmospheric Science Letters**, v. 8, p. 51–57, 2007.

SIQUEIRA, L.; NOBRE, P. Tropical Atlantic sea surface temperature and heat flux simulations in a coupled GCM. **Geophysical Research Letters**, v. 33, L15708, 2006. Available from: https://doi.org/10.1029/2006GL026528.

SKAMAROCK, W. C.; KLEMP, J.; DUDA, M.; PARK, S.-H.; FOWLER, L.; RINGLER, T.; THUBURN, J.; GUNZBURGER, M.; JU, L. Global non-hydrostatic modeling using voronoi meshes: the MPAS model. In: ECMWF NON-HYDROSTATIC WORKSHOP, 2010, Reading, UK. **Proceedings…** 2010.

SMOLARKIEWICZ, P. K.; GRABOWSKI, W. W. The multidimensional positive definite advection transport algorithm: nonoscillatory option. **Journal of Computational Physics**, v. 86, p. 355–375, 1990.

STANIFORTH, A.; WOOD, N. Aspects of the dynamical core of a nonhydrostatic, deep-atmosphere, unified weather and climate prediction model. **Journal of Computational Physics**, v. 227, p. 3445– 3464, 2008.

STEPHEN, G. L.; L'ECUYER, T.; FORBES, R.; GETTLEMEN, A.; GOLAZ, J.-C.; BODAS-SALCEDO, A.; SUZUKI, K.; GABRIEL, P.; HAYNES, J. Dreary state of precipitation in global models. **Journal of the Geophysical Research**, v. 115, D24211,2010. DOI:10.1029/2010JD014532.

TOOMEY, M.; ROBERTS, D. A.; STILL, C.; GOULDEN, M. L.; McFADDEN, J. P. Remotely sensed heat anomalies linked with Amazonian forest biomass declines. **Geophysical Research Letters**, v. 38, n.19, 2011. DOI: 10.1029/2011gl049041.

STORELVMO, T.; STERL, A.; TAPAMO, H.; VANCOPPENOLLE, M.; VITERBO, P.; WiILLEN, U. EC-Earth: A seamless Earth-system prediction approach in action. **Bulletin of the American Meteorological Society**, v. 91, p. 1357–1363, 2010.

STUHNE, G. R.; PELTIER, W. R. Vortex erosion and amalgamation in a new model of large scale flow on the sphere. **Journal of Computational Physics**, v. 128, p. 58-81, 1996.

SWARTZTRAUBER, P. N.; WILLIAMSON, D. L.; DRAKE, J. B. The Cartesian method for solving partial differential equations in spherical geometry. **Dynamics of Atmospheres and Oceans**, v. 27, p. 679–706, 1997.

TAKACS, L.; BALGOVIND, R. High latitude filtering in global grid point models. **Monthly Weather Review,** v. 111, p. 2005–2015, 1983.

TAKAHASHI, K.; PENG, X.; KOMINE, K.; OHDAIRA, M.; GOTO, K.; YAMADA, M.; FUCHIGAMI, H.; SUGIMURA, T. In: ZWIEFLHOFER, W.; MSDZYNSKI, G. (Eds.). **Non-hydrostatic atmospheric GCM development and its computational performance:** use of high performance computing in

meteorology. [S.I.]: World Scientific, 2005. p. 50-62.

TAYLOR, M. A.; EDWARDS, J.; ST CYR, A. Petascale atmospheric models for the community climate system model: new developments and evaluation of scalable dynamical cores. **Journal of Physics Conference Series**, v. 125, e012023, 2008.

TAYLOR, M.; TRIBBIA, J.; ISKANDARANI, M. The spectral element method for the shallow water equations on the sphere. **Journal of Computational Physics**, v. 130, p. 92–108, 1997.

THUBURN, J. A PV-based shallow-water model on a hexagonal–icosahedral grid. **Monthly Weather Review**, v. 125, p. 2328–2347, 1997.

TOMITA, H.; SATOH, M. A new dynamical framework of nonhydrostatic global model using the icosahedral grid. **Fluid Dynamics Research**, v. 34, n.6, p. 357-400, 2004.

ULLRICH, P. A**. Recent advances in the development of next-generation global modelling systems**. 2015. Available from: https://climate.ucdavis.edu/Ullrich-CCTP2-abstract.pdf. Access in: 26 Nov. 2017.

VELASCO, I.; FRITSCH, J. M. Mesoscale convective complexes in the Americas. **Journal of the Geophysical Research**, v. 92, p. 9591–9613, 1987. DOI:10.1029/JD092iD08p09591.

VERA, C.; HIGGINS, W.; AMADOR, J.; AMBRIZZI, T.; GARREAUD, R.; GOCHIS, D.; LETTENMAIER, D. D.; MARENGO, J.; MECHOSO, C. R.; PAEGLE, J. N.; SILVA DIAS, P. L.; ZHANG, C. A unified view of the American Monsoon Systems. **Journal of Climate**, v. 19, p. 4977–5000, 2006.

VERA, C.; SILVESTRI, G. Precipitation interannual variability in South America from the WCRP-CMIP3 multi-model dataset. **Climate Dynamics**, v. 32, p. 1003–1014, 2009. DOI: 10.1007/s00382-009-0534-7.

WAN, H. **Developing and testing a hydrostatic atmospheric dynamical core on triangular grids**. Hamburg, Germany: Max-Planck Institute for Meteorology, 2009. (Technical report, 65).

WANG, H.; FU, R. Cross-equatorial flow and seasonal cycle of precipitation over South America. **Journal of Climate**, v. 15, p. 1591–1608, 2002.

WEDI, N.; BENARD, P.; YESSAD, K.; UNTCH, A.; MALARDEL, S.; HAMRUD, M.; MOZDZYNSKI, G.; FISHER, M.; SMOLARKIEWICZ, P. Nonhydrostatic modeling with IFS: current status. In: ECMWF NON-HYDROSTATIC WORKSHOP, 2010, Reading, UK. **Proceedings…** 2010.

WETZEL, P. J.; ARGENTINI, S.; BOONE, A. Role of land surface in controlling daytime cloud amount: two case studies in GCIP-SW area. **Journal of the Geophysical Research**, v. 101, p. 7359-7370, 1996.

WILLIAMS, E.; RENNO, N. An analysis of the conditional instability of the tropical atmosphere. **Monthly Weather Review**, v. 121, p. 21-36, 1993.

WILCOX, E.; DONNER, L. The frequency of extreme rain events in satellite rain-rate estimates and an atmospheric general circulation model. **Journal of Climate**, v. 20, n.1, p. 53–69, 2007.

WILLIAMS, E.; ROSENFELD, D.; MADDEN, N.; GERLACH, J.; GEARS, N.; ATKINSON, L.; DUNNEMANN, N.; FROSTROM, G.; ANTONIO, M.; BIAZON,

B.; CAMARGO, R.; FRANCA, H.; GOMES, A.; LIMA, M.; MACHADO, R.; MANHAES, S.; NACHTIGALL, L.; PIVA, H.; QUINTILIANO, W.; MACHADO, L.; ARTAXO, P.; ROBERTS, G.; RENNO, N.; BLAKESLEE, R.; BAILEY, J.; BOCCIPPIO, D.; BETTS, A.; WOLFF, D.; ROY, B.; HALVERSON, J.; RICKENBACH, T.; FUENTES, J.; AVELINO, E. Contrasting convective regimes over the Amazon: implications for cloud electrification. **Journal of the Geophysical Research**, v. 107, e000380, 2002. DOI:10.1029/2001JD000380.

WILLIAMSON, D. L. The evolution of dynamical cores for global atmospheric models. **Journal of the Meteorological Society of Japan**, v. 85B, p. 241–269, 2007.

WORKING GROUP ON NUMERICAL EXPERIMENTATION WGNE. **Report of the twentieth session of the CAS/JSC Working Group on Numerical Experimentation**. Geneva: WMO, 2005. 56p. (WMO/TD-NO.1297).

YANG, G.-Y.; SLINGO, J. The diurnal cycle in the tropics. **Monthly Weather Review**, v. 129, p. 784-801, 2001.

YEH, K.-S.; CÔTÉ, J.; GRAVEL, S.; METHOT, A.; PATOINE, A.; ROCH, M.; STANIFORTH, A. The CMC MRB Global Environmental Multiscale (GEM) Model. Part III: nonhydrostatic formulation. **Monthly Weather Review**. v. 130, p. 339–356, 2002.

YIN, L.; FU, R.; SHEVLIAKOVA, E.; DICKINSON, R. E. How well can CMIP5 simulate precipitation and its controlling processes over tropical South America? **Climate Dynamics**, v. 41, n.11/12, p. 3127–3143, 2013.

ZHANG, G. Convective quasi-equilibrium in the tropical western Pacific: comparison with midlatitude. **Journal of the Geophysical Research**, v. 108,

n.D19, 2003a. DOI:10.1029/2003JD003520.

ZHANG, G.; Roles of tropospheric and boundary layer forcing in the diurnal cycle of convection in the U.S. southern Great Plains. **Geophysical Research Letters**, v. 30, e018554, 2003b. DOI:10.1029/2003JD018554.

ZHANG, H.; RANČIĆ, M. A global Eta model on quasi-uniform grids. **Quarterly Journal of the Royal Meteorological Society**, v. 133, p. 517–528, 2007.

ZHAO, Q.; BLACK, T. L.; BALDWIN, M. E. Implementation of the cloud prediction scheme in the Eta Model at NCEP. **Weather Forecasting**, v. 12, p. 697–712, 1997.

ZHOU, J.; LAU, W. K.-M. Principal modes of interannual and decadal variability of summer rainfall over South America. **International Journal of Climatology**, v. 21, p. 1623–1644, 2001.

ZILITINKEVICH, S. S. Non-local turbulent transport: Pollution dispersion aspects of coherent structure of convective flows. In: POWER, H.; MOUSSIOPOULOS, N.; BREBBIA, C. A. (Eds.). **Air pollution III:** air pollution theory and simulation. Southampton: Computational Mechanics Publications, 1995. p. 53–60.